THE DEVELOPMENT OF THE NATIONAL ACCELERATOR CENTRE PROTON MICROPROBE AS AN ANALYTICAL TOOL IN GEOCHEMISTRY

by

Esmé van Achterbergh

Thesis submitted in fulfilment of the requirements for the degree of Master of Science in the Department of Geological Sciences at the University of Cape Town.

Department of Geological Sciences

University of Cape Town

June 1994

ABSTRACT

This thesis describes work performed to establish and demonstrate a quantitative trace element microanalysis technique for geological material using protons accelerated by the Van de Graaff Accelerator at the National Accelerator Centre (NAC) in Faure near Cape Town. The method relies on the analysis of Proton Induced X-ray Emission (PIXE) spectra, interpreted with the help of the GeoPIXE software package. The use of the Si(Li) energy dispersive detector provides simultaneous multi-element detection at the parts-per-million (ppm) level, and a scanning beam facility permits trace element distributions to be studied at these levels.

The calibration of the detector efficiency and the thicknesses of selectable X-ray attenuating filters was performed using pure elemental samples. This involved the accurate determination of the target to detector distance, the thickness of the active volume of the Si(Li) detector crystal, the thicknesses of all the absorbing layers between the sample and the detector crystal, and the assessment of the effects of incomplete charge collection in the detector.

Tests of the alternative H^+ and a H_2^+ beams were carried out to assess their suitability for quantitative analysis. The H_2^+ beam was found to introduce significant charge integration errors regardless of improved electron suppression geometry and voltage. Hence, the H^+ beam was adopted for all quantitative work.

The method was tested using a number of international mineral and glass geostandards and secondary standards. Following calibration, these tests showed the method to be accurate to better than 5%. Precision depends strongly on counting

statistics and hence on the concentration of a particular element. However, typically precision was found to be less than 8%, increasing to ~30% near the detection limit. Detection limits are low, commonly varying between 1 and 5 ppm in the energy range 7-15 keV, for routine analysis times of 6-8 minutes.

It was shown that errors in quantitative results can be introduced if the thin-section thickness of geological specimens is less than the depth of penetration of the proton beam, as elements in the underlying glass slide are excited, and their X-rays added to the final spectrum. The multilayer facility of GeoPIXE enabled correction for the contribution of X-rays from the substrate and also for the effect of the finite thickness of the section on the calculated X-ray yields. While this approach will be essential for many unique thin-sections held in research collections, this work illustrates the need for thicker sections (> 60 μm) for improved trace element analysis.

The application of the proton microprobe to mineralogical studies in geology was illustrated by the analysis of a suite of eclogite xenoliths from the Roberts Victor kimberlite, mounted as polished thin-sections. The good precision and sensitivity of the microprobe allowed the identification of chemical differences between constituent mineral phases of the kyanite-bearing and kyanite-free eclogites, as well as trace element zoning profiles in the garnet grains across the contact of the two eclogite types. Elemental imaging of small areas in two of the kyanite eclogites showed the heterogeneity in distribution of the elements Sr and Ba in the clinopyroxene.

It was concluded that, in view of its high accuracy, precision and sensitivity, the proton microprobe will be applicable to a wide variety of geological studies dealing with the concentration and distribution of trace elements in minerals.

ACKNOWLEDGEMENTS

This project was initiated and supervised by Assoc. Prof. Anton le Roex and Prof. John Gurney at the Department of Geological Sciences of the University of Cape Town. I am grateful for their able and attentive supervision.

The project was supported financially by the Foundation for Research Development.

The valuable contributions of Dr. Chris Ryan during both the experimental and writing stages of this project is gratefully acknowledged.

The staff of the Van de Graaff Group of the National Accelerator Centre was most helpful. In particular, I would like to thank Bill Schmidt and his able team of operators for ensuring optimum accelerator operation during the experiments. Karl Springhorn and Cecil Churms played key roles in the early development stages of the proton microprobe, and offered their continued support throughout the project. As part-time employee of the Van de Graaff Group, Dr. Victor Prozesky allowed me freedom and initiative to complete this thesis.

I am grateful to Johanci Bingle for valuable assistance during the final stages of the thesis preparation. Rose Kovats drafted Figure 6.1, for which I am thankful.

Soli Deo Gloria.

TABLE OF CONTENTS

CHAPTER 1

INTRODUCTION

Particle Induced X-ray Emission (PIXE), a variant of the more general technique of X-ray emission analysis, was first introduced at the Lund Institute of Technology in 1970 (Johansson *et al.*, 1970). Since then, numerous publications describing the development and applications of PIXE have appeared. Cookson *et al.* (1972) were the first to describe the use of a micron-sized focused beam spot for quantitative PIXE analysis: the proton microprobe.

The proton microprobe has been used extensively in geoscience applications. Notable is, for example, the analysis of lunar and meteoric material by the Heidelberg proton microprobe group (Blank *et al.*, 1984; Bajt and Traxel, 1991), and the analysis of ore deposit and sulphide mineralogy by the Ottawa microprobe group (Cabri, 1988). The CSIRO in Sydney, Australia, has demonstrated the level of productivity that can be reached when an accelerator and proton microprobe are dedicated to geological research (Griffin *et al.*, 1989; Griffin *et al.*, 1990; Ryan *et al.*, 1990; O'Reilly *et al.*, 1991 and many others).

The electron and proton microprobes are complimentary techniques in analytical geoscience, together providing a wealth of information regarding the composition of geological specimens. Fast and reliable analysis can be carried out by the electron microprobe, providing the essential major element composition of the mineral(s) of interest. This is necessary for accurate reduction of the proton microprobe data. The greatly reduced background in the PIXE spectrum then allows the determination of the low level trace element concentrations of the samples by the proton microprobe.

Sample preparation requirements are simple; thin geological sections, mounted on glass slides, or mineral separates, mounted in standard epoxy blocks (ca 2 cm diameter) are used routinely. The samples are coated with a thin carbon film to avoid charge integration errors, and are used in both the electron and proton microprobe target chambers.

In the latter half of 1991, scientists at the National Accelerator Centre (NAC) commissioned the hardware for a proton microprobe from Oxford microbeams in England. The initial idea behind the purchase of the microprobe was to use it non-quantitatively in physics applications. Examples of such applications are Rutherford backscattering (RBS) studies, secondary electron imaging and qualitative X-ray emission analysis. However, the Department of Geological Sciences at the University of Cape Town (UCT) soon realized the quantitative potential of the microprobe and its usefulness in trace element analysis of geological material by utilizing the microPIXE technique. The Department consequently purchased the GeoPIXE software programme (Ryan *et al.*, 1990) from CSIRO (Sydney, Australia) to be used in conjunction with the microprobe in quantitative geological applications.

The acquisition of the necessary hardware and software did not mean immediate and meaningful quantitative results since all the units of the microprobe setup had to be tested, the detector efficiency and filter thickness had to be calibrated, and the viability of the probe as a quantitative analytical instrument had to be investigated. As a result, this project was initiated, the aim of the study being the development of an accurate and precise analytical tool, allowing geochemists low-level trace element analysis.

To illustrate the application of the proton microprobe in the analysis of geological samples, the new NAC proton microprobe was used to analyze a suite of eclogite samples from the Roberts Victor kimberlite.

CHAPTER 2

INSTRUMENTATION AND DATA ACQUISITION OF THE NATIONAL ACCELERATOR CENTRE PROTON MICROPROBE

2.1 The Van De Graaff Accelerator

The National Accelerator Centre (NAC) proton microprobe (PMP) hardware has recently been fitted to one of five beamlines serviced by the 6 MV single-ended Van de Graaff accelerator. Two ion sources, i.e. a Penning and a Duoplasmatron source are available at NAC, and can provide users from different scientific disciplines with a wide variety of particle beams and energies. However, for pure applications using PIXE (Particle Induced X-ray Emission) and RBS (Rutherford Backscattering), the H^+, H_2^+ and He^+ beams, typically at energies of 2 to 5 MeV, are used almost exclusively.

The Penning source was designed to supply particle beams consisting of heavy ions such as $^{16}O^+$, but it was found that lighter particle beams (i.e. H^+ and H_2^+) can also be obtained. However, the H^+ yield is very low, and the current finally measured on the target is too low for low-level analysis within reasonable analysis time. The Duoplasmatron source, which supplies high yields of both H^+ and H_2^+, is therefore preferred for PMP analysis.

Particles are extracted from the ion source by applying an "extraction voltage" of approximately -10 to -40 kV, depending on the required current. A crossed-field analyzer (or velocity selector) selects the particle beam to be used.

The entire dome (terminal) of the Van de Graaff accelerator is charged positively by charge carried on a rotating belt, and it therefore repels the positive particles as they exit the terminal. The particles are subsequently accelerated down a flight tube to the analyzing magnet. The purpose of the magnet is, firstly, to analyze the beam energy, and secondly, to bend the beam through 90° into a horizontal plane. It then passes through a set of control slits (which provide a feedback signal to fine-tune the terminal voltage) and a quadruple doublet lens, into the beam-switching magnet. The latter selects the port through which the beam passes into the appropriate beamline.

Beam instability is still a limitation at the Van de Graaff facility, affecting mainly the vertical beam resolution and the optimum current obtainable. Factors that have been identified as possible causes for the unstable beam are the following:

* unstable plasma in the ion source,
* poor terminal voltage stability,
* limitations on the feedback from the control slits,
* power supply ripple,
* stray AC magnetic field distortions, and
* amplification of beam instability by poor beam focusing in the doublet quadruple lenses (Tapper *et al.,* 1993)

2.2 The Proton Microprobe Beamline

The PMP beamline (manufactured by Oxford Microbeams; Grime *et al.,* 1991) has been mounted at the 0° port of the switching magnet, which is therefore switched off

during microprobe operation. Two sets of collimator slits, approximately 5 metres apart, are positioned along the beamline. Magnetic scanning coils are positioned between the second set of collimators and the quadruple lenses. The coils are PC controlled (Churms *et al.,* 1993) to allow beam scanning and beam positioning. The beam is focused by a triplet set of quadruple lenses, before finally entering the sample chamber. The essenal units of the microprobe are shown in Plate 1, Appendix A.

The maximum coil current, in the quadruple triplet, obtainable from the power supplies for beam focusing have a nominal value of 100 A. For the focusing of a 5.0 MeV H_2^+ beam (which corresponds in energy per proton to a 2.5 MeV H^+ beam), the magnet currents operate close to the maximum value (i.e. ± 97 and 102 A respectively). A set of fans is positioned close to the lenses to avoid over-heating.

From the relationship:

$$\text{current} \propto \text{magnetic rigidity}$$

$$\propto \frac{(mE)^{1/2}}{q} ,$$

where m = mass of the particle,

E = energy of the particle and

q = charge of the particle,

it is clear that the magnet current needed to focus a 2.5 MeV H^+ beam is less by approximately a factor of two.

It was found experimentally (Tapper *et al.*, 1993) that the best beam resolution obtainable is approximately 0.5 μm horizontally, and 2 μm vertically. The loss in vertical resolution is a result of the unstable beam described in the previous section, i.e. any energy dispersion (or energy pulses) in the beam as it accelerates downwards, translates into a vertical aberration after its directional change in the analyzing magnet.

2.3 The Sample Chamber

A schematic drawing of the PMP sample chamber is given in Figure 2.1. The numerals given below in parentheses correspond to those in the figure. It is also shown in Plate 2, Appendix A.

The faraday cup (1) mounted directly opposite the incoming beam direction (2) collects the current during analyses of thin targets such as pure element foils which do not stop the beam. If thick targets are being analyzed (i.e. those that stop the beam), the current is measured directly from the target ladder. Depending on the thickness of the target, the faraday cup or the target ladder is connected to the current integrator, which produces a pulse train output where each pulse corresponds to a fixed unit of charge.

The optical microscope (3), used to view the sample (4), is set at a 135° angle to the left of the beam direction, and therefore has the limitation that the sample surface, which is normal to the beam, will only be in focus along a thin vertical strip. The microscope is mounted such that this "focused strip" corresponds exactly to the y-cross hair when the target surface is at the focal point of the beam. The microscope has a

zooming capability which greatly facilitates location of grains/points to be analyzed.

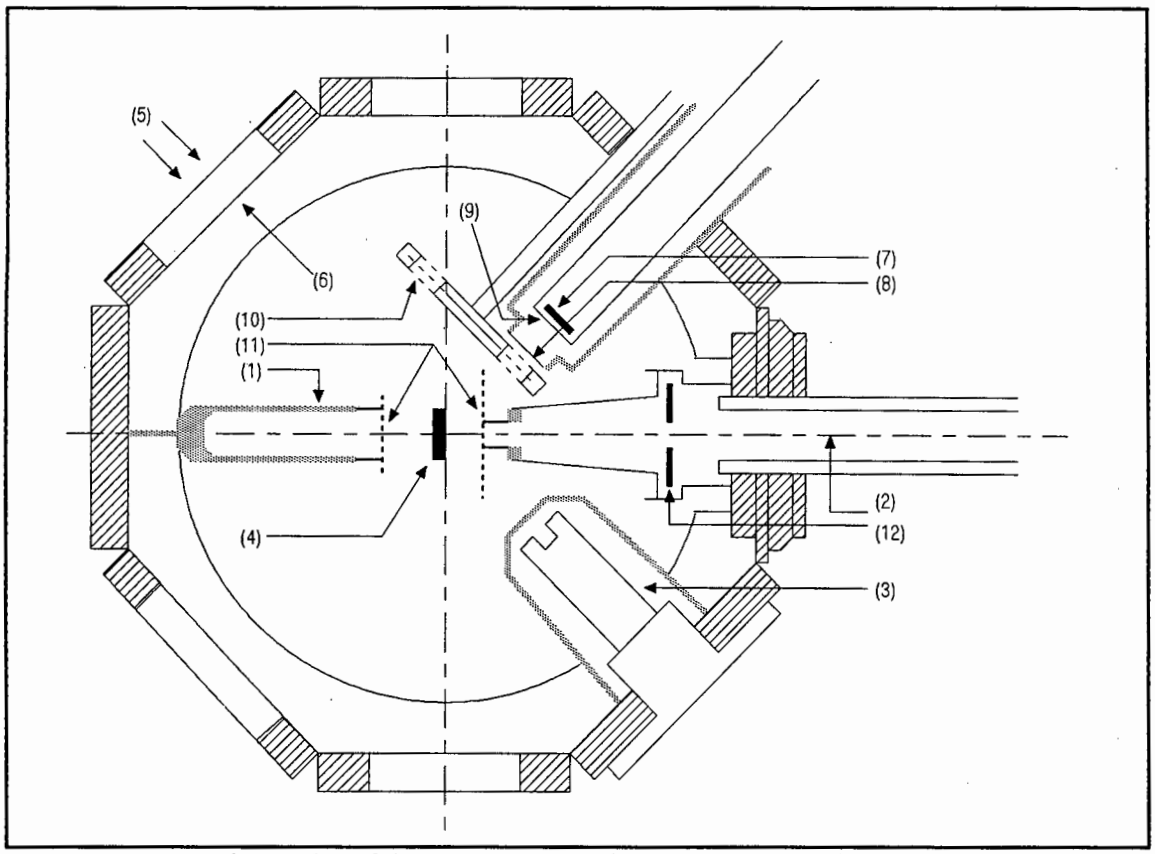

Figure 2.1: Schematic drawing of the proton microprobe sample chamber (not to scale). The numerals are explained in the text.

A light source (5) is placed at the window (6) opposite the microscope for transmitted light illumination of the sample. Two small light bulbs (suspended from the chamber lid; not shown in the diagram) are positioned inside the chamber for additional illumination.

The Si(Li) energy dispersive detector (7) is situated at 135° to the right of the beam direction. It is separated from the evacuated sample chamber by means of an intervening kevlar ($C_{14}H_{10}N_2O_2$) foil, 75 μm thick (8). This precaution protects the thin

(8 μm) Be window (9) of the detector during the pump-down cycle of the sample chamber, and stops backscattered protons from entering the detector.

An adjustable filter wheel (10) is positioned in front of the detector tube. The wheel can be fitted with eight X-ray filters, and it allows the selective attenuation of X-rays, depending on the requirements of the analyst.

The secondary electron suppressor (11) is used to ensure accurate charge collection. An analysis is terminated once a specified preset charge is attained. However, secondary electrons that are excited by the high energy beam, are emitted from the sample surface and the loss of these electrons causes the attainment of this preset charge prematurely. This introduces a significant error when elemental concentrations are calculated. The high negative voltage that is applied by the suppressor, forces the electrons back into the sample. The annular surface barrier detector (12) is used to detect backscattered α-particles for RBS applications.

Figure 2.2 is a schematic diagram of the fundamental electronic units of the PMP hardware. It forms the basis of the discussion that follows in sections 2.4 to 2.8. The abbreviations in Figure 2.2 are as follows: AMP = amplifier, ICR = incoming count rate, ADC = analog-to-digital conversion, Q = charge integrator, PC = personal computer, CAMAC = CAMAC crate and XSYS = XSYS data acquisition system.

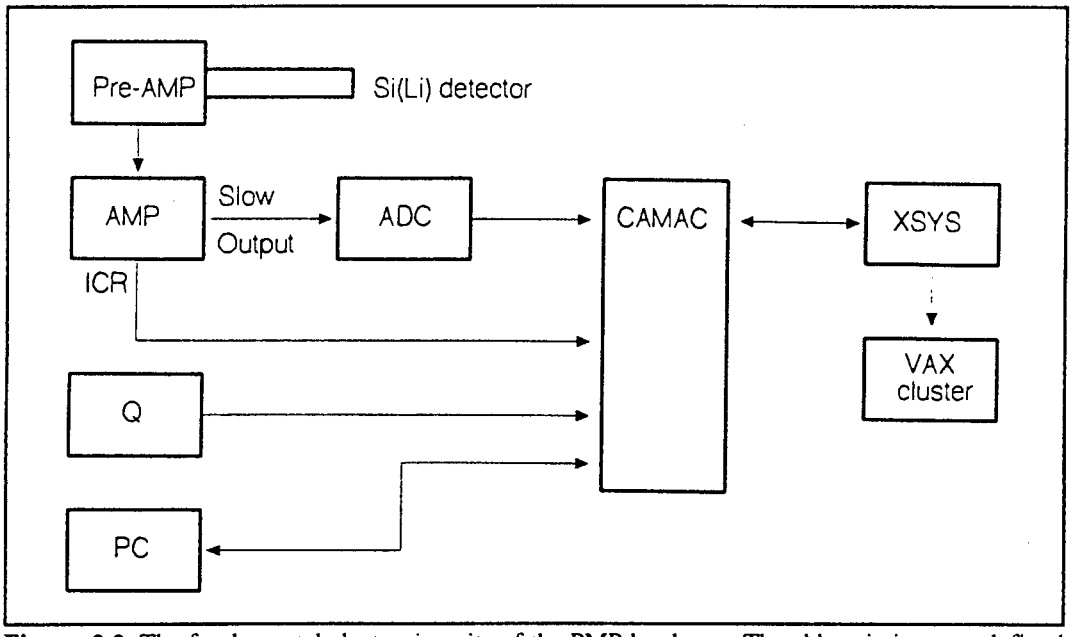

Figure 2.2: The fundamental electronic units of the PMP hardware. The abbreviations are defined in the text.

2.4 The Si(Li) Energy Dispersive X-ray Detector, and the Pre-amplifier

The X-ray detector is a Li drifted Si semiconductor crystal with an active area of 30 mm^2, and a thickness of 3 mm. By definition, a semiconductor is a very poor conductor of electric charge, which becomes momentarily conducting by the absorption of X-ray photons and the subsequent creation of electron-hole pairs. This charge (electrons and "holes") is swept out by a bias (an electric potential applied across the crystal) and is recorded as a charge pulse. The magnitude of the pulse is proportional to the energy of the incident X-ray photon.

Various detector artifacts, e.g. detector efficiency and resolution need to be considered during quantitative analysis. These are described and discussed in Chapter 3.

The total charge of the pulse collected at the detector electrode is integrated by

the pre-amplifier and converted to a voltage signal of discrete amplitude, retaining its proportionality to the energy of the X-ray photon. The detector and the pre-amplifier input FET[1] are kept at liquid nitrogen temperature (-195° C), to minimize the effects of electronic noise and to keep Li from drifting out of the Si(Li) crystal.

2.5 The Amplifier

The NAC proton microprobe uses the Canberra Model 2024 Spectroscopy Amplifier for amplification and processing of pulses. Amplification is done by the electronic differentiation and subsequent integration of the signal. This can be envisaged as the conversion of a series of steps, applied to the signals received from the pre-amplifier output, to resultant Gaussian shaped pulses. Pulse processing includes *pulse shaping* and *pulse pileup rejection.*

Pulse shaping, characterized by a *shaping time constant,* must optimize the signal-to-noise[2] ratio, which is reflected in the X-ray spectrum by the peak resolution. The best resolution is generally achieved by a large shaping time constant. However, larger shaping times increase the probability for *pulse pileup,* i.e. a second pulse enters the electronic circuitry before the processing of a first pulse has been completed[3].

Pulse pileup rejection reduces the unwanted effects of pulse pileup, which is of

---

[1] Field Effect Transistor.

[2] Electronic noise is reduced by "electronic filters" as part of the integration function. It uses the frequency characteristics of the noise to effectively filter out noise from pre-amplifier signals.

[3] When two pulses enter the processing system closely spaced in time, their amplitudes are added together, corresponding to an erroneous pulse of higher amplitude which looks like an X-ray photon of higher energy.

particular importance at high count rates, and with long shaping times. When two pulses have enter the electronic circuitry closely spaced in time, both pulses are rejected and are not processed further by the system. Figure 2.3 illustrates the effect pulse pileup has on the spectrum (a) and how this effect is reduced by pulse pileup rejection (b). If two pulses arrive within a sufficiently short time interval they cannot be distinguished as separate, and are interpreted by the amplifier as a single pulse with an amplitude equal to the sum of the two separate pulses. The sum effect of such signals appear on the X-ray spectra as discrete *pileup peaks* (indicated with the letter p in Figure 2.3), which have to be identified and corrected for during data reduction.

When pulses are rejected, or while pulses are being processed, the system is "dead" for a certain portion of the time (i.e. some analysis time elapses when the data acquisition system is unavailable). This effect is known as the *system dead-time*. To minimize the amplifier contribution to dead-time[4], the shortest possible shaping time constant must be used, but still retaining the best possible resolution. Table 2.1 shows FWHM (full width at half maximum) values for the MnK_{α}[5] line at different shaping times and constant count rate. Optimum resolution was obtained at a shaping time of 4 μs, without excessive dead-time. The value of 4 μs was therefore selected as the working shaping time constant.

---

[4] Dead-time cannot be avoided completely and corrections are still necessary. This is discussed in section 1.8.

[5] $K\alpha = K\alpha_1 + K\alpha_2$

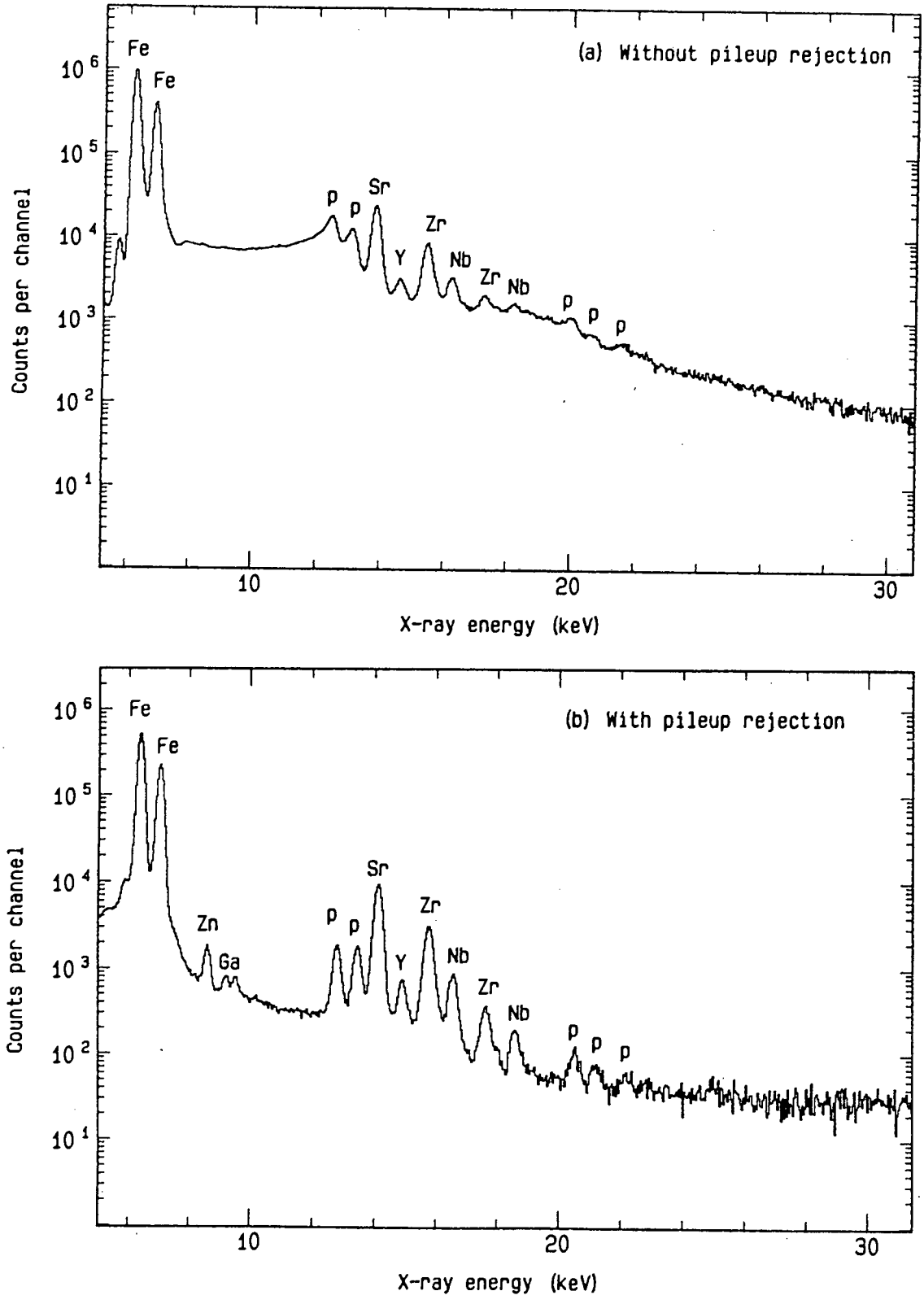

Figure 2.3: Two X-ray spectra of a mineral standard: (a) without pileup rejection, (b) with pileup rejection. The letter p indicates pileup peaks.

Table 2.1

Peak resolution and dead-time effects at different shaping time constants[6].

Shaping time constant	Resolution FWHM for Mn K_{α}	Dead-time
0.5 μs	300 eV	3.2 %
1.0 μs	274 eV	3.8 %
2.0 μs	256 eV	5.1 %
4.0 μs	210 eV	7.4 %
8.0 μs	235 eV	12.2 %

Amplification and pulse shaping take place in the "slow channel" of the amplifier, which outputs to the analog-to-digital convertor (see below). If these pulses survive pileup rejection and system dead-time, they are referred to as the *measured counts*. However, the amplifier also has a "fast channel" operating in parallel with the slow channel which allows the detection of **all incoming pulses.** The aim of the "fast channel" is to produce a logic pulse for every pre-amplifier pulse, and the result is known as the ICR (Incoming Count Rate). These pulses are not processed but output directly to a scaler in the CAMAC crate (the interface between the electronic circuitry and the VAX data acquisition computer) which counts the pulses as they enter. The ICR therefore allows the determination of the *total counts* from the Si(Li) detector during an analysis, apart from the completely overlapping pulses that appear in the spectrum as pileup peaks (these are corrected for during spectrum analysis, Chapter 4).

[6] Measurements done at a constant count rate of 1000 c/s.

2.6 Analog to Digital Conversion

The analog-to-digital converter (ADC) converts the amplitude of the voltage pulse received from the amplifier to a digital number. This number is proportional to the X-ray energy and is the "address" of the "bin" or "channel" to increment in the spectrum (section 2.7). The maximum number of channels (typically 1024) selectable on the ADC is known as the "conversion gain".

The conversion process in the ADC takes a certain amount of time during which it cannot accept further pulses from the amplifier for processing. *ADC dead-time*, therefore, contributes to the overall system dead-time, and must be corrected for.

2.7 Multichannel Analysis

Multichannel analysis (MCA) is the process by which the "address" for a pulse from the ADC is identified and the appropriate channel in the spectrum is incremented. This process is handled by the XSYS data acquisition system, with a CAMAC crate acting as the interface between the electronic circuitry and the VAX computer.

The particular energy range (e.g. 0-40 keV) is selected using the amplifier gain. This total range divided by the conversion gain leads to a certain "energy per storage channel" (keV/chan), the interval of X-ray energy stored in a channel.

2.8 Data Acquisition

Initialization of an analysis.

Data acquisition is handled by the XSYS general purpose data acquisition system package (Gould *et al.*, 1981; Gould and Roberson, 1983) on a VAX-11/750 mini-computer. The initialization of an analysis is controlled by a personal computer (PC) running the CCSCAN program (Churms *et al.*, 1993). It allows the selection of up to 32 points for either continuous or single point analysis. An analysis is initiated by a click on the PC mouse button at which the PC *gates on* the ADC (i.e. allowing the ADC to process signals) and the scalers in the CAMAC crate, and informs XSYS to start data collection.

Termination of an analysis.

A scaler in the CAMAC crate which is connected to the current integration module, counts the charge pulses as they accumulate. When the preset charge is reached, the ADC and the scalers are *gated off*, and XSYS is instructed to halt the run and write the data to a spectrum file. XSYS, in turn, signals the PC that the run has been terminated and instructs it to move to the next point.

XSYS to GeoPIXE.

The VAX mini-computer is connected to NAC's VAXcluster (Pilcher and Wikner, 1991) which allows further processing of data. A FORTRAN program automatically

performs dead-time correction (see below) and writes the XSYS spectrum file to a format which can be read by the data analysis software package GeoPIXE (Ryan *et al.*, 1990). The GeoPIXE format file is stored in a central data area on the cluster. GeoPIXE can be instructed to start spectrum analysis automatically while data for the next point is being collected. GeoPIXE will be discussed in more detail in Chapter 4.

Apart from routine point analysis, XSYS has the capability to do elemental mapping of a maximum area ≈ 1.5 mm x 1.5 mm, at the routine beam energy of 3 MeV. It uses a coefficients matrix built by GeoPIXE, which will be discussed in Chapter 4.

Dead-time correction.

The dead-time correction compensates statistically for counts that have been lost due to dead-time in the amplifier and the ADC. It is defined according to the relationship:

total input counts / measured counts,

The final spectrum is multiplied by this ratio.

Total counts are the total number of ICR pulses recorded in the scaler in the CAMAC crate. The scaler counts all incoming events from the Si(Li) detector, except those pulses that completely overlap and appear in the spectrum as pileup peaks. Corrections are made in the GeoPIXE package (Ryan *et al.*, 1990) for dead-time that arises from these pulses (Chapter 4). *Measured counts* are all the counts in the final spectrum, determined by integration of the spectrum.

CHAPTER 3

THE THEORY OF THE PIXE ANALYTICAL TECHNIQUE

3.1 Introduction

In the last two decades, the proton microprobe (PMP) has become a powerful tool for the in situ, nondestructive analysis of mineral grains. It is complementary to the electron microprobe (EMP), the latter being used for the geochemical analysis of major elements at the weight % (wt %) level, while the PMP is used for trace element analysis at the parts-per-million (ppm) level.

The PMP utilizes the micro-PIXE technique, i.e. particle induced X-ray emission with a very small proton beam (typically 1-20 μm). It is a variant of the more general technique of X-ray emission analysis, and was first introduced at the Lund Institute of Technology in 1970 (Johansson *et. al.*, 1970). It has since been established as a viable analytical method in numerous laboratories around the globe, and a large number of publications describing the development and application of PIXE have appeared. Combined with the appropriate hardware and software, it has a unique feature in that it provides a means for quantitative standardless trace element analysis, once the system has been calibrated.

In this chapter, the theory of the PIXE technique and the calculation of elemental concentrations is outlined. The calibration procedure, which is an integral part of the preparation of any PMP setup for routine analysis, is described. It forms the general basis

for Chapter 4, in which quantitative analysis more specific to the NAC PMP is discussed.

3.2 The Proton Beam-Target Interaction

When a particle beam bombards a target of interest, it induces various processes in the target. These processes provide a wealth of information regarding the composition and structure of the sample.

3.2.1 X-ray Emission

Of primary importance for this study is X-ray emission. The incident particles (projectiles) eject inner shell electrons, leaving vacancies in the K, L and M shells of the atom. This process is known as atomic ionization and the measure of the probability of ionization of a particular shell of element Z is known as the ionization cross-section σ_Z. The cross section is expressed in units of barns (B)[7]. It increases with increasing velocity of the incident particle and reaches a maximum when the proton velocity matches that of the bound electron. The cross section slowly decreases with a further increase in the projectile velocity.

The atom, in an excited state, de-excites within approximately 10^{-16} s (Johansson and Campbell, 1988) by electron transitions from higher shells to fill the vacancy. This de-excitation may be accompanied by the emission of an X-ray photon. The energy of the photon is characteristic of the element and the X-ray intensity is proportional to the

---

[7] 1 Barn = 10^{-24} cm^2

concentration of the element in the sample. Various electron transitions in a single atom are possible as shown in the atomic model diagram (Figure 3.1), reproduced from Woldseth (1973). The relative proportions of electron transitions from different shells to fill a vacancy (e.g. the ratio of the transition from the L-shell to the K-shell, and from the M-shell to the K-shell) are known as the branching ratios (b).

3.2.2 Auger Electrons

A finite probability exists for the energy emitted during the filling of a vacancy to be reabsorbed internally to the parent atom. Instead of an X-ray photon being emitted, the excess energy is transferred to an electron, which is then emitted from the atom as an *Auger electron*. This process decreases the total X-ray yield.

The following ratio, or *fluorescence yield* (ω), can now be introduced as a measure of the probability that the filling of a vacancy gives rise to an X-ray:

$$\omega = \frac{\text{emitted X-rays}}{\text{emitted X-rays + Auger electrons.}} \qquad (3.1)$$

3.2.3 Secondary Fluorescence

If the energy of an X-ray photon (emitted from an element in the sample) is above the absorption edge of a neighbouring element, the photon may ionize the neighbouring atom. This leads to secondary X-ray emission, referred to as *secondary fluorescence.*

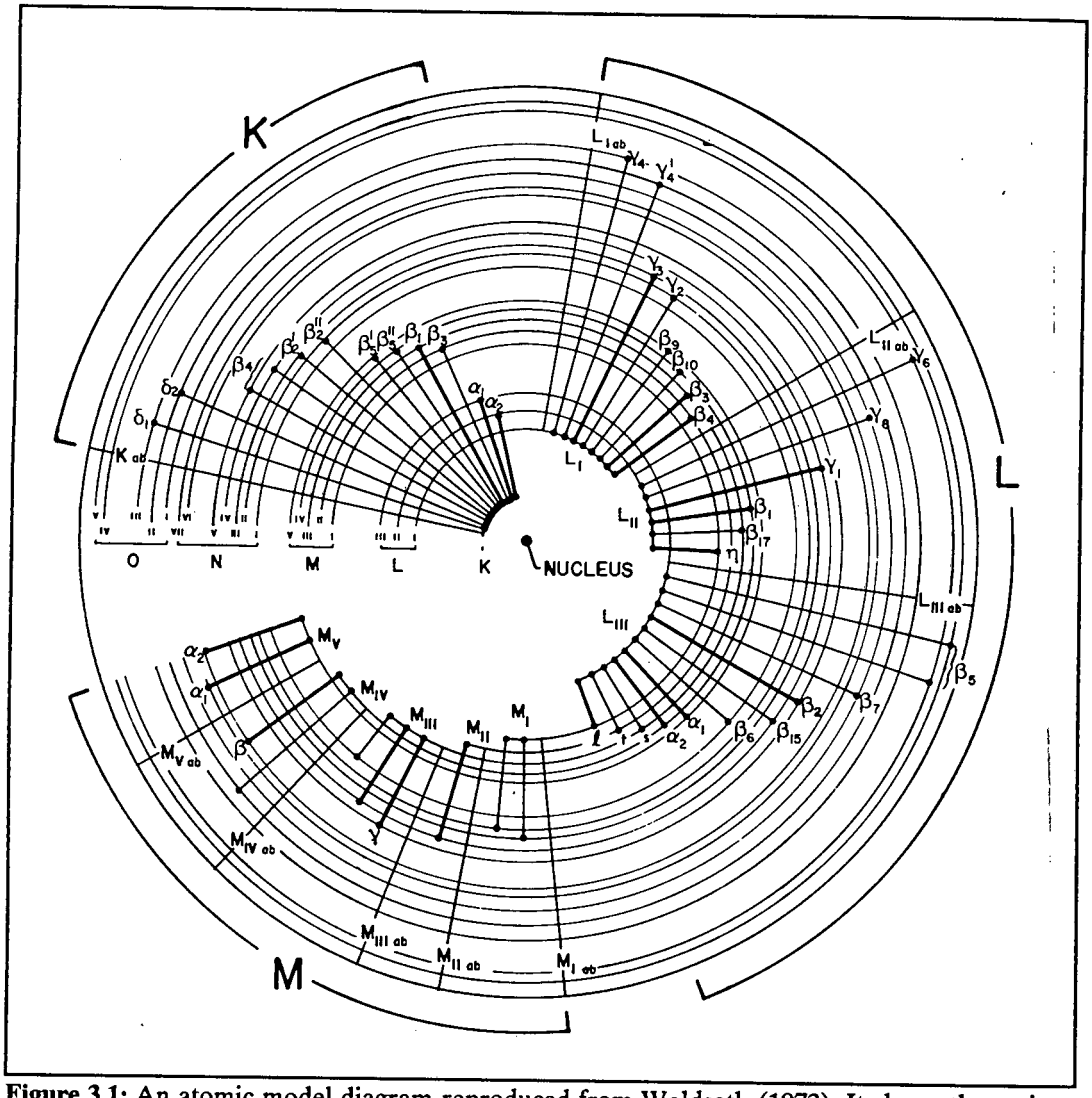

Figure 3.1: An atomic model diagram reproduced from Woldseth (1973). It shows the various electron transitions that may follow the creation of an electron vacancy.

3.2.4 Secondary Electrons

As the proton beam enters the target, the particles interact with electrons in the outer shells of the target atoms, transferring some of the particle energy to the electrons. The electrons are set in motion and may escape from the target as secondary electrons. The rapid *decceleration of secondary electrons* in the target is the cause of secondary electron bremsstrahlung, as will be discussed in section 3.4.

The interaction of the incident particles with electrons in the target is the principal mechanism for the gradual energy loss of MeV energy protons. A measure of the magnitude by which the matrix "stops" the beam, is expressed as the matrix stopping power S.

3.2.5 Gamma Rays

Particle beams of sufficient energy induce nuclear reactions in the nuclei of low Z elements in the target with the subsequent emission of γ-rays. This radiation contributes to the overall background, the extent of which is difficult to predict (Johansson and Campbell, 1988).

3.2.6 Elastic Scattering

Protons of the incident beam that collide with atomic nuclei in the target are said to be *elastically scattered.* The negative acceleration suffered by the protons during these collisions is the cause of proton bremsstrahlung (section 3.4).

Backscattered protons may damage the Si(Li) crystal of the detector, and this is an additional reason for the presence of a protective kevlar foil in front of the detector (Chapter 2 - Figure 2.1).

3.3 The Calculation of Elemental Concentrations

To calculate the X-ray yield (Y_0) of X-ray line k, emitted from element Z in a thin target (i.e. the protons pass through the sample without loss of energy and the X-rays suffer negligible absorption), the following equation is given by Johansson and Campbell (1988):

$$Y_0(Z) = \frac{N_p M_Z(Z)\sigma_Z(E_0)\omega_Z b_{Zk}\varepsilon_Z N_A}{A_Z} \qquad (3.2)$$

where N_p is the number of protons that pass through the target, σ is the cross section at constant proton energy E_0, ω, b and ε are the fluorescence yield, branching ratio and detector efficiency[8] respectively, N_A is Avogadro's number, A_Z is the atomic mass of element Z and M_Z is the mass per unit area of element Z. M_Z is given by:

$$M_Z = C_Z \rho x \qquad (3.3)$$

where C_Z is the relative concentration of Z in the target, ρ is the target density and x the thickness of the thin target.

However, in most of the PIXE applications described in this study, the targets are sufficiently thick to not only change the beam energy, but to stop the passage of the beam completely. This change in energy incrementally changes the cross section. In addition,

[8] In their detector efficiency term ε, Johansson and Campbell (1988) include both the intrinsic efficiency of the detector, and the detector solid angle. This is discussed in more detail in section 3.5

X-rays that are emitted along the path of the beam are subject to some degree of self-absorption on their way to the target surface. This self-absorption is also a function of the beam energy. An integration across the entire path of the beam is necessary, with the limits of integration being the entrant beam energy E_0 and zero (Johansson and Campbell, 1988). Equation 3.2 then becomes:

$$Y_0(Z) = \frac{N_p C_Z \omega_Z b_{Zk} \varepsilon_Z N_A}{A_Z} \int_0^{Eo} \frac{\sigma_Z(E) T_Z(E)}{S(E)} dE \qquad (3.4)$$

where S(E) is the matrix stopping power (Anderson and Ziegler, 1977). The self-absorbtion term T_Z is given by:

$$T_Z = \exp\left(\frac{-\mu\rho x(E)}{|\cos\Theta|}\right) \qquad (3.5)$$

where μ is the mass attenuation coefficient (Thiesen and Vollath, 1967) and x(E) is the depth within the target from which the X-ray originates, where the protons have slowed to energy E. Θ is the detector angle (Fig 3.2).

Ryan *et al.* (1990) related the peak areas in a spectrum N_{Zk}, for X-ray line k and element Z, to the X-ray yields of the major X-ray line Y_{Z1} and relative X-ray intensities r_{Zk} by:

$$N_{Zk} = Q\Omega(\varepsilon_k T_k)(Y_{Z1} r_{Zk}) C_Z \qquad (3.6)$$

$$\text{where} \quad r_{Zk} = Y_{Zk}/Y_{Z1} \qquad (3.7)$$

and where Y_{Z1} is similar to Y(Z) in equation 3.4, but calculated for unit beam charge, detector efficiency and the concentration of Z in the sample. These are added as separate terms in equation 3.6. The number of protons is related to the integrated charge Q and a term for the correction of attenuation of X-rays in X-ray filters (T_k) is included. ϵ denotes the intrinsic detector efficiency and Ω is the detector solid angle (section 3.5).

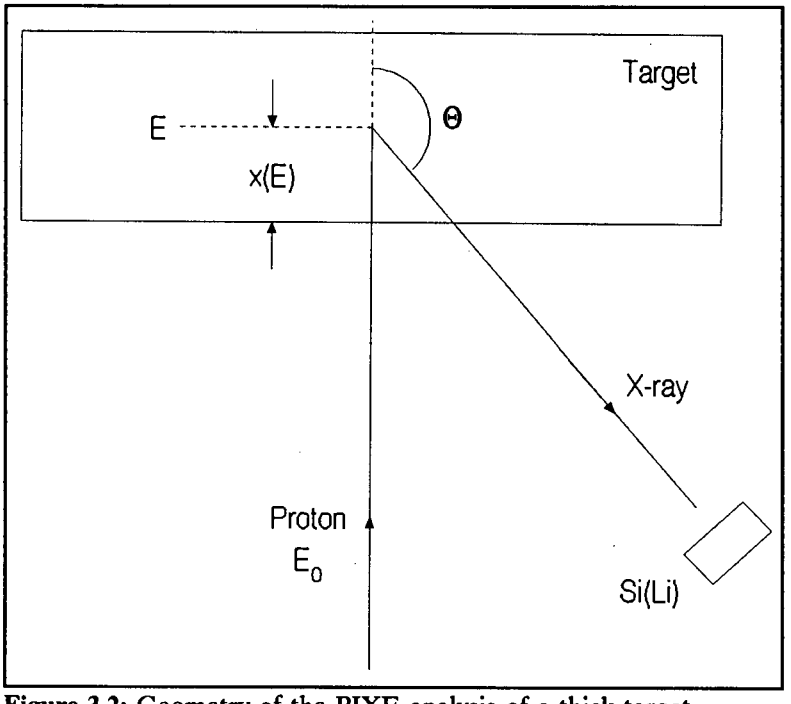

Figure 3.2: Geometry of the PIXE analysis of a thick target.

3.4 The PIXE spectrum

The result of the X-ray emission from the target is an X-ray spectrum. The X-ray energy (in units of kilo-electron volts, or keV) is plotted on the X-axis, and the X-ray intensity (in units of counts per channel) on the Y-axis. The spectrum consists of a continuum background (Figure 3.3), overlain by the characteristic X-ray lines of discrete energies emitted from atoms in the target (Figure 3.4).

3.4.1 Background

Bremsstrahlung[9] background is attributed to the X-ray emission that results from the slowing-down of secondary electrons and protons in the target. The X-ray photons that are emitted have a wide range in energies and are therefore observed in the spectrum as a continuum (Figure 3.3). Gamma rays which may Compton scatter through the detector contribute to the background as well, i.e a flat continuum extending to high energies in the spectrum. The exact extent of the γ-ray contribution is, however, difficult to predict (Johansson and Campbell, 1988).

Secondary electron bremsstrahlung.

An incident proton that collides with an electron in an energy shell of an atom, transfers some or all of the its energy to the electron which is ejected. In turn, this electron slows down through interaction with atoms in the target, and emits X-ray photons with a range of energies up to the energy of the electron (Folkmann *et al.*, 1974a, 1974b; Ishii and Morita, 1984).

The approximate maximum energy T_m that can be transferred to a free electron in a head-on collision with a proton of energy E_p is given by the equation (Folkmann *et al.*, 1974a, 1974b):

$$T_m = (4m/M)E_p \qquad (3.8)$$

---

[9] "Bremsstrahlung" means "braking radiation".

Proton bremsstrahlung

The energy loss suffered by incident particles through collisions with atomic nuclei may be accompanied by X-ray photon emission. The photons have a wide range in energies and contribute to the "flat" background across the entire range of the PIXE spectrum as shown in Figure 3.3.

3.4.2 X-ray Lines

Various electron transitions within the atoms of a single element are possible (Figure 3.1), and therefore appear as a series of lines on the spectrum (Figure 3.4). For the sake of simplicity, the X-ray line notation used in this study is the conventional Siegbahn notation. However, mention must be made of the IUPAC notation which describes the exact electron transitions. For example, the $K_{\alpha 1}$ line results from the transition of an electron from the L_3 level to a vacancy in the K shell. The correct IUPAC notation for the resulting X-ray line is therefore K-L_3. Similarly, the IUPAC notation for the $K_{\beta 1}$ line is K-M_3. A table with a complete comparison of the Siegbahn and IUPAC notations for X-ray lines is given in Table A1, Appendix A.

Based on the probability of a certain electron transition taking place, the X-ray lines have varying intensities. For example, the intensity of the $FeK_{\beta\_}$ line is approximately 11% of the $FeK_{\alpha\_}$ line. No distinction is made here between the $K_{\alpha 1,2}$, and $K_{\beta 1,2,3}$ lines because in this energy range in the spectrum they cannot be resolved. However, at higher energy (for example the Ba K lines), the $K_{\alpha 1,2}$ lines

are resolved and here the intensity of the $K_{\alpha 2}$ line is approximately 50% of the $K_{\alpha 1}$ line.

The shapes of the peaks are close to Gaussian, and their widths are characterized by the full-width-at-half-maximum (FWHM). The peak width is a measure of the detector resolution, which will be discussed in section 3.5.

Other lines that appear in the spectrum are the pulse pile-up peaks and the Si escape peaks (identified in Figure 3.4 with the letters p and e respectively). The latter is discussed in section 3.5.

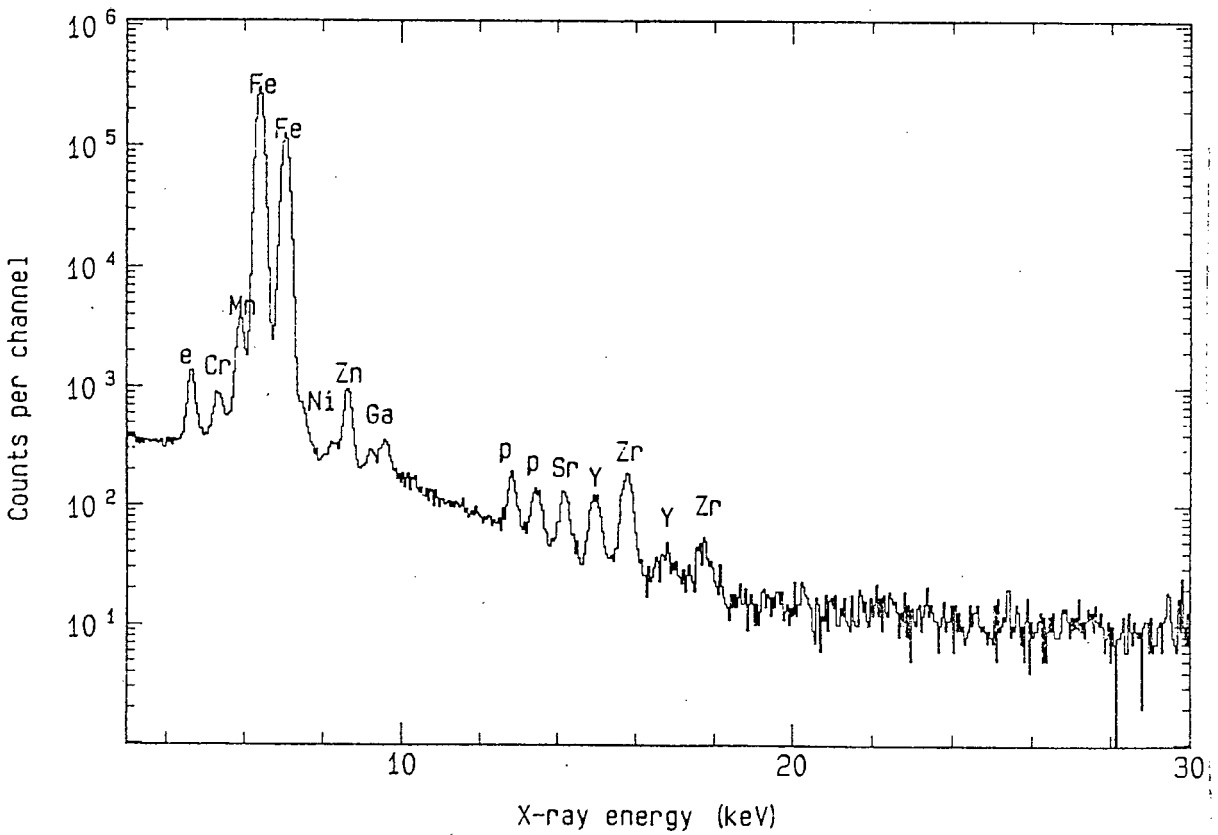

Figure 3.4: A typical PIXE spectrum, collected by the analysis of a garnet grain with a proton beam of energy 3 MeV, and a total integrated charge of 14 μC.

3.5 Detector Response

Several artifacts arising from the detector response to X-ray emission from atoms in the target appear in the PIXE spectrum. These are escape peaks, peak tailing, pileup peaks and the FWHM of the peaks in the spectrum. Most importantly, the efficiency of the detector largely determines the quality of the results.

3.5.1 Detector Efficiency

The efficiency[10] of a Si(Li) detector is influenced by a number of factors. These are: (a) the thickness of the Be entrance window, (b) the thickness of the Si dead-layer[11], (c) the thickness of the gold contact layer at the front face of the detector, (d) the thickness of a possible ice layer, (e) the thickness of the Si(Li) crystal and (e) the geometrical efficiency (the active area of the crystal combined with the distance between the target and the detector).

The Be window, the dead-layer, the gold contact and the ice layer attenuate low energy X-rays. At higher X-ray energy, the Si(Li) crystal thickness is the dominant factor, as some X-rays could pass through the crystal without detection. The geometrical efficiency effects all X-rays equally and is given by the equation:

---

[10] The probability that an X-ray which is emitted from the target is detected in the full energy peak of that line in the PIXE spectrum.

[11] The Si "dead-layer" is an inactive layer at the surface of the Si(Li) crystal.

$$\text{geometrical efficiency} = (\Omega/4\pi)\ , \qquad (3.9)$$

where Ω is the detector solid angle, expressed in units of steradians (sr) and given by:

$$\Omega = \frac{A}{d^2} \qquad (3.10)$$

A is the active area of the crystal and d is the distance between the X-ray source and the detector. To ensure accurate quantitative results, the magnitude of each factor has to be known or measured accurately.

3.5.2 Detector Resolution

An X-ray peak at energy E in the PIXE spectrum has a Gaussian distribution. This follows the effects of noise and the statistical variation in the creation of electron-hole pairs and the collection of charge pulses at the detector electrodes. The full-width-at-half-maximum (FWHM) of an X-ray peak is therefore a measure of the detector resolution.

However, it has been found through empirical observations that the resolution is considerably better than predicted for Poisson counting statistics on the number of electron-hole pairs. This difference is incorporated in the so-called "Fano factor" (F). For a Si(Li) detector, $F \approx 0.10$ to 0.13.

If the random contribution of electronic noise is considered as well, the total detector resolution is given by:

$$FWHM = \sqrt{(FWHM)^2_{noise} + [2.35\ (F\varepsilon E)^{1/2}]^2} \qquad (3.11)$$

ε is the energy per electron-hole pair created, and the factor of 2.35 converts from standard deviation of a Gaussian peak to FWHM. F is the dimensionless Fano factor, and E is the energy in keV of the incident photon.

3.5.3 The Escape Peaks

An incident X-ray photon with an energy (E) higher than the K absorption edge[12] of Si (1.838 keV), may excite Si K X-rays from the Si(Li) crystal. These X-rays are mostly reabsorbed, and the resulting measured energy of the photon remains E. However, the probability exists that some of these X-rays "escape" from the crystal, and the resulting energy of the photon becomes:

$$E - 1.74 \text{ keV},$$

where 1.74 keV is the X-ray energy of the escaping Si K_α. In the case of an escaping Si K_β X-ray the resulting energy becomes

$$E - 1.83 \text{ keV}.$$

---

[12] The "critical energy" needed to ionize a particular atomic shell (K, L or M) of an atom.

The effect of this in the spectrum is the loss of counts from the parent line at energy E, and the appearance of the Si K escape peaks in the spectrum at energies of 1.74 keV and 1.83 keV **below** that of the parent line.

Although the intensity of the Si K_α escape peak is $\approx$ 1% or less of its parent peak, care must be taken to avoid confusion during peak identification. The intensity of the Si K_β escape peak is only 11% that of the K_α escape peak and is therefore negligible.

3.5.4 Peak Tailing

Incomplete collection of the charge produced in the detector as electron-hole pairs may cause "tails" on the low energy side of X-ray lines. This may introduce errors in the estimation of peak areas of low intensity peaks that overlap with tails of higher intensity lines, or it may obscure the presence of low intensity peaks completely. In the former case, corrections can be made during data reduction by fitting an empirical function to the peak tails.

3.6 The Calibration Procedure

3.6.1 Detector Efficiency Calibration

It was pointed out in section 3.5 that the magnitude of various characteristics of the X-ray detector have to be known accurately to obtain good quantitative results. The respective effects of absorption of X-rays in the Be window, the Au contact and the Si

dead-layer are difficult to distinguish above the Si K and Au M absorption edges, and their thicknesses are therefore set to the manufacturer's values.

The active thickness of the crystal, although generally set to the manufacturer's specification, can show slight variations (~15%) and is adjusted to fit high energy X-ray trends, i.e. a deviation from the known composition for elements of high X-ray energy (e.g. Ba), indicates an error in the specified thickness. For example, if the calculated value for Ba is less than the known composition, this can be due to insufficient correction being made for the loss of X-ray counts which pass through the crystal without detection. The active thickness of the crystal is therefore thinner than specified, and should be adjusted.

An error in the calculation of concentrations for elements of low X-ray energy is attributed to the loss of X-rays due to incomplete charge collection (the cause of peak tailing), because the effect is observed to be more pronounced at low energies. This is corrected by the inclusion of an additional Si absorber. X-rays are also absorbed in the X-ray filters used, and these have to be calibrated separately (see below).

The active area of the crystal is also specified by the manufacturer, but the target-detector distance is inherent to a particular microprobe setup and has to be measured. The distance is measured physically, but some uncertainty (~10%) arises from the actual position of the Si(Li) crystal inside the detector snout, which can be variable. Therefore, because the target-detector distance affects all the elements equally, a constant error across the energy spectrum may be observed and the distance parameter in the efficiency term has to be adjusted accordingly.

3.6.2 Filter Calibration

X-ray filters are used routinely during PIXE analysis to selectively attenuate unwanted X-ray lines. Elements of low X-ray energy are affected to varying degrees by absorbtion, and accurate corrections can only be made if the absorber thickness is well constrained.

Two schemes are employed for the accurate determination of the absorber thickness. The first is a simple calculation of the areal density ρx by dividing the mass of the foil by the accurately measured area. The mass is measured using a high precision balance.

A second scheme was suggested by Ryan *et al.* (1990), in which the *effective* thickness that reproduces the observed absorption of X-rays is determined. The thickness is calculated using the ratio of the peak areas of a low energy X-ray from a light element x (e.g. Cr K_α), measured with (N_x^{absorb}) and without (N_x^0) the filter, relative to the equivalent ratio for a high energy X-ray from a heavy element y (e.g. Mo K_α). These relative ratios are related to the thickness t by (Ryan *et al.*, 1990):

$$\exp(\mu_x-\mu_y)t = \frac{N_x^0}{N_x^{absorb}} \cdot \frac{N_y^{absorb}}{N_y^0} \qquad (3.12)$$

This calculation of t is independent of the composition of the target or errors in the beam current integration, but subject to the criterion that the X-rays x and y have to be largely separated in energies. The mass attenuation coefficient of y (μ_y) is then negligible

relative to μ_x, and equation 3.12 provides a measure of the effective absorber thickness. The method is reported to determine the thickness to better than 3% (Ryan *et al.*, 1990).

CHAPTER 4

QUANTITATIVE ANALYSIS USING THE NAC PROTON MICROPROBE

4.1 Introduction

The combination of the general hardware of the proton microprobe (PMP), as described in Chapter 2, with a software system that does spectrum analysis and PIXE X-ray yield calculation facilitates routine PIXE analysis. The software used in conjunction with the NAC PMP is the GeoPIXE package of Ryan *et al.* (1990), which is outlined briefly below.

In Chapter 3, the general method for the calibration of detector efficiency and filter thickness was described. System calibration is an integral part of the preparation of any proton microprobe (PMP) for routine quantitative analysis, and in this chapter the results of the calibration of the NAC PMP are presented. These data are followed by a short description of the general running procedures adopted for quantitative PIXE micro-analysis using the NAC proton microprobe

Both the H^+ and H_2^+ beams are available at the NAC for routine analysis. However, as shown in this chapter, charge integration errors render the H_2^+ beam unfavourable for quantitative analysis. The chapter is concluded with a discussion of possible errors that are introduced if standard geological sections are thin enough for the beam to pass through the sample and to excite X-rays of elements of the underlying glass slide.

4.2 The GeoPIXE Software Package

The data obtained from PMP analysis as raw spectra are analyzed by the GeoPIXE software package (Ryan *et al.,* 1990). The peak areas are determined by the spectrum fitting program PIXE FIT and combined in the GeoTRACE program with the precalculated X-ray yields and relative intensities, calculated by the LAYER program.

4.2.1 X-ray Yield Calculation

The FORTRAN program LAYER (Cousens *et al.*, 1987) calculates the X-ray yield Y_{kZ} for each characteristic X-ray line k and for each element Z over the integrated path of the beam, correcting for the effects of self-absorption and secondary fluorescence. The yields are calculated in "generic" form, i.e. assuming an ideal detector (efficiency = 1, solid angle = 1) and no filters. The intensities of all the lines within an energy shell, relative to the major line in the shell are also calculated. The calculation requires a matrix of known composition which is obtained in this work from prior electron probe (EMP) analysis.

4.2.2 Peak Fitting and Background Estimation

Peak areas are calculated from the PIXE spectrum by a non-linear least squares fit to the raw data, using the fitting program PIXE FIT (Ryan *et al.*, 1990). The fit varies the peak area of the major X-ray line N_{Z1} as the free parameter, and uses the relative intensities of the other lines of the same element Z as calculated by LAYER to complete

the fit to all the X-ray lines of Z. The relative intensities have been corrected for filter attenuation and detector efficiency.

The Si K_{α} escape peaks and the pile-up peaks are also treated by PIXE FIT (Ryan *et al.*, 1990). The former is fitted 1.74 keV below each parent line (e.g. major element Fe), with a calculated intensity of ~1% of the parent line. The positions and intensities of pileup peaks are calculated by a mathematical approximation of the probability of various combinations of pileup events occurring. This is describe in full in Ryan *et al.* (1990).

Accurate background subtraction is a prerequisite to accurate trace element analysis, and this lead to the development of the SNIP[13] algorithm (Ryan *et al.*, 1988). It provides the background estimation and is performed as the first stage of PIXE FIT upon which the extraction of peak areas follow.

The linear least squares fit generates a table of peak areas of the major lines with their error estimates, extracted from the error matrix as suggested by Bevington (1969). The goodness of fit is evaluated by a reduced chi-squared χ_v^2 and a root-mean-square error (Isozumi, 1985). An estimation of the minimum detection limit (MDL) is also included, calculated from the equation of Currie (1968), which represents the 99% confidence limit:

$$MDL = 3.29 \sqrt{B} \qquad (4.1)$$

[13] Statistics-sensitive Nonlinear Iterative Peak-clipping.

where B is the underlying background. From equation 4.1, the MDL is calculated as a number of counts (N) from which it is translated into units of ppm in the same manner as the calculation of elemental concentrations using equation 4.2 below.

4.2.3 The Calculation of Trace Element Concentrations

Trace element concentrations C_Z are calculated from equation 3.6 (equation 4.2 below) in terms of the generic X-ray yields Y_{Zl} and relative intensities r_{Zk} (as calculated by LAYER) corrected for the experimental parameters, i.e. the intrinsic detector efficiency ε_k, the detector solid angle Ω and the filter attenuation T_k. The concentrations are related to the peak areas as obtained from PIXE FIT by:

$$N_{Zk} = Q\Omega(\varepsilon_k T_k)(Y_{Zl} r_{Zk})C_Z \qquad (4.2)$$

The evaluation of the C_Z from N_{Zk} is performed using the interactive program GeoTRACE (Ryan *et al.*, 1990).

4.2.4 Spectrum Display and Manipulation

A fourth program in the GeoPIXE package, called FLASH, is used for interactive spectrum display and manipulation. It allows peak identification, full-width-at-half-maximum (FWHM) estimates, peak area estimates, summing of spectra, refining of the energy calibration, examination of the goodness of fit, etc.

4.2.5 Dynamic Analysis and Elemental Imaging

Two additional utilities of the GeoPIXE package, *dynamic on-line analysis* and *true elemental imaging*, have recently been implemented in combination with the XSYS data acquisition package at NAC. These procedures, which are briefly outlined below, are described in full elsewhere (Ryan and Jamieson, 1993; Ryan *et al.*, 1993).

In short, dynamic analysis is the fast, *on-line* determination of elemental concentrations. The method uses a matrix transformation that effectively resolves overlaps between neighbouring elements and subtracts background to transform the spectrum directly into a list of elemental concentrations. It requires the prior analysis of the same mineral, or in the case of elemental mapping, a similar combination of minerals under the same experimental conditions. The background shape and the selection of elemental components is therefore predetermined before the dynamic analysis is done. Subsequently, if dynamic analysis is required during on-line data acquisition, the *background intensity* and *major line peak areas* are rapidly extracted from the spectrum, and the elemental concentrations are calculated at that instantaneous charge.

Dynamic analysis is particularly useful when a fast and reliable way is needed to identify, for example, very small inclusions in minerals that cannot ordinarily be observed in the microscope setup, or to locate areas of subtle chemical differences, etc. The analyst can therefore locate these areas of chemical significance for further detailed analysis, or avoid areas that are contaminated with small inclusions, in a much shorter space of time.

results obtained by the microPIXE analytical technique are largely dependent on the accurate correction for the X-rays that are lost.

These correction procedures are built into the GeoPIXE software package (Ryan *et al.*, 1990), and are quite straightforward if the reasons for X-ray losses are known and well characterized. In other words, the magnitude of a number of experimental parameters must be known accurately to allow for accurate correction. These parameters are:

(a) the active area of the crystal

(b) the thickness of the absorbing layers between the target and the detector.

(c) the target to detector distance

(d) the thickness of the crystal

(e) the thickness of the X-ray filters.

As was discussed in section 3.6, a number of these parameters are set to the manufacturer's specifications (e.g. (a) and (b) above), but the exact magnitude of others cannot be accurately measured ((c), (d) and (e)). For example, the measurement of the target to detector distance is hindered by the uncertainty of the exact location of the Si(Li) crystal inside the detector snout. The measurement of the X-ray filter thickness is dependent on the accuracy of the database of absorption coefficients, or on the accuracy of the mass and area measurements, depending on which technique is used to determine the thickness (section 3.6).

Step 2: Filter thickness

After the target to detector distance was corrected, a discrepancy in the results for the highest and lowest energy X-ray lines remained. At high energies X-rays suffer little absorption so absorber thickness errors have negligible effect. However, at high energy the efficiency varies linearly with the thickness of the detector. Therefore, the trend for the high energy X-rays is attributed to an error in the nominal thickness of the Si(Li) crystal and is discussed under step 3. The values for the low energy X-rays fall below the known values and this is a result of an underestimation of the absorption terms, i.e. the thickness of one or more of the absorbing layers.

"Ice" thickness calibration

Because of the use of a kevlar vacuum window in front of the detector, strong absorption at low X-ray energy does not permit the analysis of light elements. Furthermore, in this work in order to optimize the sensitivity to heavier trace elements generally an additional Al filter is used which strongly attenuates X-rays from elements below Cr. Therefore, it is not possible to distinguish between the effects of errors in the thicknesses of the kevlar window, detector dead-layer, Be window or a possible ice layer on the face of the detector. This is because all X-rays of interest fall above the absorption edges of the elements in these absorbers. Hence, the errors in the thicknesses of these layers must be considered together. In this work these errors, and losses due to peak tailing, which have their origins in incomplete charge collection from a layer at the front of the detector, are accounted for by the addition of a single "ice" absorbing layer. The

thickness of the "ice" layer was determined to be 15 μm using the analysis of the standards without the customary Al filter in order to flatten the low energy part of the efficiency curve.

Filter thickness calibration

Three Al X-ray filters, with nominal thicknesses of 40, 160 and 320 μm, respectively, are used routinely during analysis of geological material. The accurate thickness of the 40 μm foil was determined by the areal density measurement described in section 3.6. It was found to be 40.78 ± 0.82 μm. The 160 and 320 μm filters comprise, respectively, 4 and 8 layers of the foil, and their accurate thicknesses were therefore calculated by simple multiplication to be 163.1 ± 3.3 μm and 326.2 ± 6.5 μm, respectively.

In addition to these measurements, the effective filter thicknesses were calculated by the method of Ryan *et al.* (1990) (also described in section 3.6). The results obtained by this method for the three filters are 40.7 ± 1.2 μm, 161.2 ± 4.8 μm and 322.4 ± 9.8 μm, respectively. These values, which are consistent with those obtained by the weighing method, were used as a starting point during the analysis of the standards. It was found that the thickness was still slightly underestimated and the values were further adjusted to 41.5 μm, 166 μm and 332 μm respectively. These revised values are within the calculated uncertainty estimates. The results, before and after the filter calibration, are shown in Figure 4.1(b).

Step 3: The thickness of the Si(Li) crystal

Accurate knowledge of the thickness of the Si(Li) crystal of the particular detector that is used for quantitative analysis is imperative to obtain correct results for the high X-ray energy elements. The results obtained for the elements Pd, Sn and Ba were found to be higher than the known results (Figure 4.1(c)) and this was attributed to an underestimation of the Si(Li) crystal thickness. In other words, there is an overcorrection for the loss of X-rays[16] as less X-rays are truly lost than calculated by the software. Therefore, the crystal is thicker than the nominal value of 3.0 mm and this was adjusted to 3.5 mm. The final calibration curve, including this corrected value, is plotted in Figure 4.1(c). Within the analytical uncertainty, all results fit the known concentrations.

4.4 General Running Procedures

The general running conditions during routine PMP analysis are specific to the particular sample of interest and the requirements of the analyst. There are, however, some parameters that are more or less constant.

Due to the relatively high X-ray production cross-section and the relatively low γ-ray yield of most geological specimens, the 3 MeV H^+ beam is used most commonly during routine analysis. The beam-on-target current is typically between 5 to 15 nA, for a beam spot of 10 to 20 μm in diameter. Count rates are kept below 1 500 cps, to avoid possible errors with the dead-time correction and to minimize pileup peak contamination

[16] A number of high energy X-rays pass through the Si(Li) crystal without detection.

of the spectrum. The secondary electron suppression voltage is set at -1 kV (section 4.5).

The duration of an analysis is determined by a specified preset integrated charge Q. This value is selected by the analyst and depends on the nature of the analytical requirements. For example, if high sensitivity is a requirement, a larger value for Q is selected to ensure a long analysis time. Q is related to the analysis time t and current I by:

$$Q = It \qquad (4.3)$$

Typically, an integrated charge of 3 μC is used.

4.5 A Comparison of the H^+ and H_2^+ Beams for Quantitative Analysis

Tapper *et al.* (1993) found that the brightness of the H_2^+ beam is superior to that of the H^+ beam from both the Penning and the Duoplasmatron ion sources, and due to the higher current subsequently measured on the target surface, the H_2^+ beam was favoured for X-ray mapping applications. However, for *quantitative* point analyses, the relative merits of the H_2^+ and H^+ beams had to be assessed.

Analysis of pure element and mineral standards using a 4 MeV H_2^+ beam yielded systematically low results. This was attributed to charge integration errors, caused by insufficient secondary electron suppression. Consequently, pure element standards were analyzed at increasing suppressor voltages for both the H^+ and the H_2^+ beams to determine at which voltage sufficient suppression is attained (the saturation voltage). The

results are shown in Figure 4.2. Au was chosen as the pure element standard to illustrate the saturation behaviour because it has a very high yield of secondary electrons (hence its wide usage as coating material in Electron Microscopy).

It is clear from Figure 4.2 that complete saturation could not be attained in the case of the H_2^+ beam up to the maximum suppressor voltage of -2 kV. This effect is not fully understood, but it could possibly be attributed to either one or both of two causes; (1) the suppression geometry and (2) insufficient suppression of the high energy electron that enters the target with the two hydrogen atoms in the H_2^+ molecular ion. Although the suppression geometry was improved (a larger suppressor ring was used and a magnet was attached to the target ladder) the results using the H_2^+ beam remained systematically low (Figure 4.2).

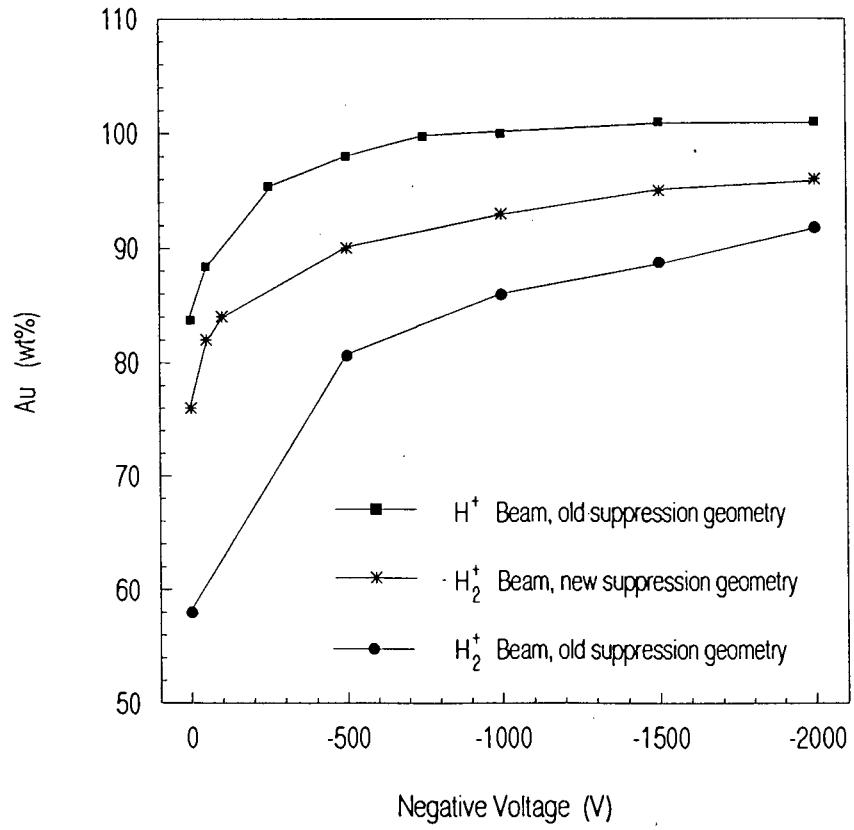

Figure 4.2: Electron suppression saturation curves for different beams using a pure Au target.

High beam currents are not required for routine PIXE micro-analysis, and this consideration, combined with the charge integration problem described above, renders the H^+ beam more favourable for quantitative analysis.

The high energy electron is absent in the case of the H^+ beam and complete saturation is achieved at a relatively low voltage. Hence, a working voltage of -1 kV is selected for routine quantitative analysis. This ensures effective suppression yet is well below the maximum voltage that can be applied to the suppressor.

4.6 Problems Encountered with Thin Targets Mounted on a Glass Substrate

The penetration depth of protons into a target of non-negligible thickness varies as the density of the target varies, but it is on the order of a few tens of μm's for a proton energy of a few MeV (Tapper and Malmqvist, 1991). The proton beam ionizes elements in the target along its entire path until it is stopped by the matrix, and is therefore sensitive to elements at depths of several tens of μm's.

The nominal thickness of the average geological thin section is 30 μm, mounted on a thick glass substrate. Two scenarios exist where the proton beam may excite significant X-rays from elements in the underlying glass slide; (a) the section is thinner than the nominal value of 30 μm, or (b) the target has a relatively low mean atomic number which provides little attenuation of X-rays excited in the glass. Elements in the glass slide that are excited by the beam cannot be differentiated from the target elements in the final PIXE spectrum, and will lead to erroneous results if not accounted for.

The correct X-ray yields for different layers in such a layered target is calculated by the program LAYER, which is part of the GeoPIXE software package (Ryan *et al.*, 1990). The program can treat up to four layers of known thickness and density in a single target, with one layer of unknown composition. In the case of the two-layer geological specimen, the proton beam stops in the glass (layer 2), and it can therefore be assumed that the glass is infinitely thick. The detailed major and trace composition of the glass can be determined by separate PMP analysis. If the thickness and density of the specimen (layer 1) is known accurately, correct X-ray yields are calculated and the contribution of the glass to the final concentration is subtracted. For an unknown layer 1, the correct elemental concentration can thus be calculated, assuming that the glass slide is homogeneous.

There is, however, a degree of uncertainty in the nominal 30 μm thickness of the geological specimens and an alternative method can be used to determine the effective thickness of the section (Ryan and Cousens, 1992). It requires the presence of at least one element that occurs ONLY in the glass (e.g. As[17]) and therefore has a concentration of zero ppm in the sample. X-ray yields for *different thicknesses* are calculated and combined with the data from the PIXE spectrum. Because the contribution of the glass is *subtracted* from the final concentration of the unknown layer, the X-ray yield calculation done using the *correct thickness* will yield a *zero concentration* for the unique substrate element in the mineral[18].

---

[17] As is commonly added to glass to counteract the negative effect of Fe on the clarity of the glass.

[18] The X-ray yield calculations done for *too thin* sections will yield negative concentrations, and those done for *too thick* sections will yield concentrations above zero ppm.

It was found that for the geological applications described in the following chapters (bimineralic and kyanite eclogites), Sr can be used as such an unique substrate element, as it is found to occur abundantly in the glass, but **not** in the kyanite. However, the presence of Sr cannot be excluded in the clinopyroxene and the garnet grains and the accurate thicknesses of the thin sections can therefore only be calculated for the thin sections that contain kyanite.

Five geological samples where analyzed for trace elements in this study, two of which exhibit a homogeneous distribution of the mineral kyanite. Accurate thin section thicknesses for these two samples were calculated by the method described above and corrections were made for the contribution of glass slide elements to the final concentration.

Kyanite is heterogeneously distributed in the remaining three samples and several thin section were cut on each of the samples, some of which **do not** contain kyanite. The thicknesses of the kyanite-bearing thin sections were calculated by the method described above and it was found that the preparation of these thin sections was done very precisely. Thin sections of the same samples have the same, or very similar, thicknesses (the results of these thickness calculations are shown in Table 4.1 below). The thicknesses of the remaining thin sections (kyanite-free), for each individual sample, were therefore *assumed* to be the same as the average of those thicknesses that were *calculated.* Calculated thin sections thicknesses are shown in bold typeface in Table 4.1.

To avoid these correction procedures, and thus avoiding further possible sources

of error, it is suggested that thin sections be made thicker than the depth of penetration of the proton beam. This would ensure that the target is of infinite thickness and that no elements in the glass are analyzed. For silicate minerals, a thin section thickness > 60 μm is suggested.

Table 4.1

The determination of the thin section thicknesses of the heterogeneous kyanite- bearing eclogites. The thin sections shown in bold typeface contain kyanite, and their thicknesses could therefore be calculated.

Sample	Thickness	How determined
HRV 17-B	**39 μm**	**Calculated**
HRV 17-C	**36 μm**	**Calculated**
HRV 17-D	**36 μm**	**Calculated**
HRV 30-1	48 μm	Assumed
HRV 30-2	48 μm	Assumed
HRV 30-3	**48 μm**	**Calculated**
HRV 30-4	**48 μm**	**Calculated**
HRV 30-5	**48 μm**	**Calculated**
HRV 30-7	48 μm	Assumed
JJG 177-1	**48 μm**	**Calculated**
JJG 177-2	**46 μm**	**Calculated**
JJG 177-3	**42 μm**	**Calculated**
JJG 177-4	45 μm	Assumed
JJG 177-5	45 μm	Assumed

CHAPTER 5

ACCURACY, PRECISION AND SENSITIVITY OF THE PROTON MICROPROBE

5.1 Introduction

The proton microprobe has various applications in the fields of geology, biology, medicine and solid state physics. In many of these disciplines emphasis is placed on quantitative analysis. Therefore, the accuracy, precision and sensitivity of the microprobe has to be thoroughly tested and proven. In this chapter, the results of these tests are presented and discussed.

The *accuracy* of an analytical instrument refers to its ability to reproduce the *correct* composition of a sample, i.e. the exact quantity of each element in the sample. A 100 % correct result can never be achieved, but analysts strive to attain the highest accuracy possible in applications where good quantitative results are required.

The *precision* of the proton microprobe refers to the *reproducibility* of the result through repeated analyses. High precision is important in the analytical sciences in order to investigate true chemical differences within a sample and between different samples.

The ability of an analytical technique *to detect* low concentration elements in a sample is its *sensitivity*. The proton microprobe is a relatively sensitive technique with the ability to analyze elements on the parts-per-million (ppm) level. The sensitivity depends largely on many experimental parameters, and the proton microprobe analyst has to strive

to attain the best possible sensitivity.

5.2 Accuracy

5.2.1 Tests of Analytical Accuracy

The accuracy of the proton microprobe was tested by the analysis of targets of known composition such as pure element metals and foils, steel standards and geological standards. In addition, interlaboratory comparisons were made with the proton microprobe laboratory at the Heavy Ion Analytical Facility (HIAF), Sydney, Australia. A number of proton microprobe results of geological specimens were compared with the results obtained by X-ray Fluorescence Spectroscopy (XRFS) as a further test of accuracy.

The analysis of pure element standards allows the calibration of the detector efficiency (discussed in Chapters 3 and 4), as well as the identification of sources of analytical error. Examples of errors that have been identified are (a) the insufficient suppression of backscattered electrons when using the H_2^+ particle beam (discussed in Chapter 4) and (b) detector malfunctions.

The results of two tests are presented in Tables 5.1 and 5.2. The complete results are given in Tables B1 to B10, Appendix B. Figure 5.1 summarizes all the tests that were done, by plotting the data obtained by PMP analysis (Y-axis) against the certified concentrations, or the concentrations obtained by other techniques (X-axis).The results

show that the proton microprobe is an analytical instrument of high accuracy (generally, the accuracy is better than 95%). The tests did, however, highlight a number of problems that must be guarded against during quantitative analysis. These are discussed below.

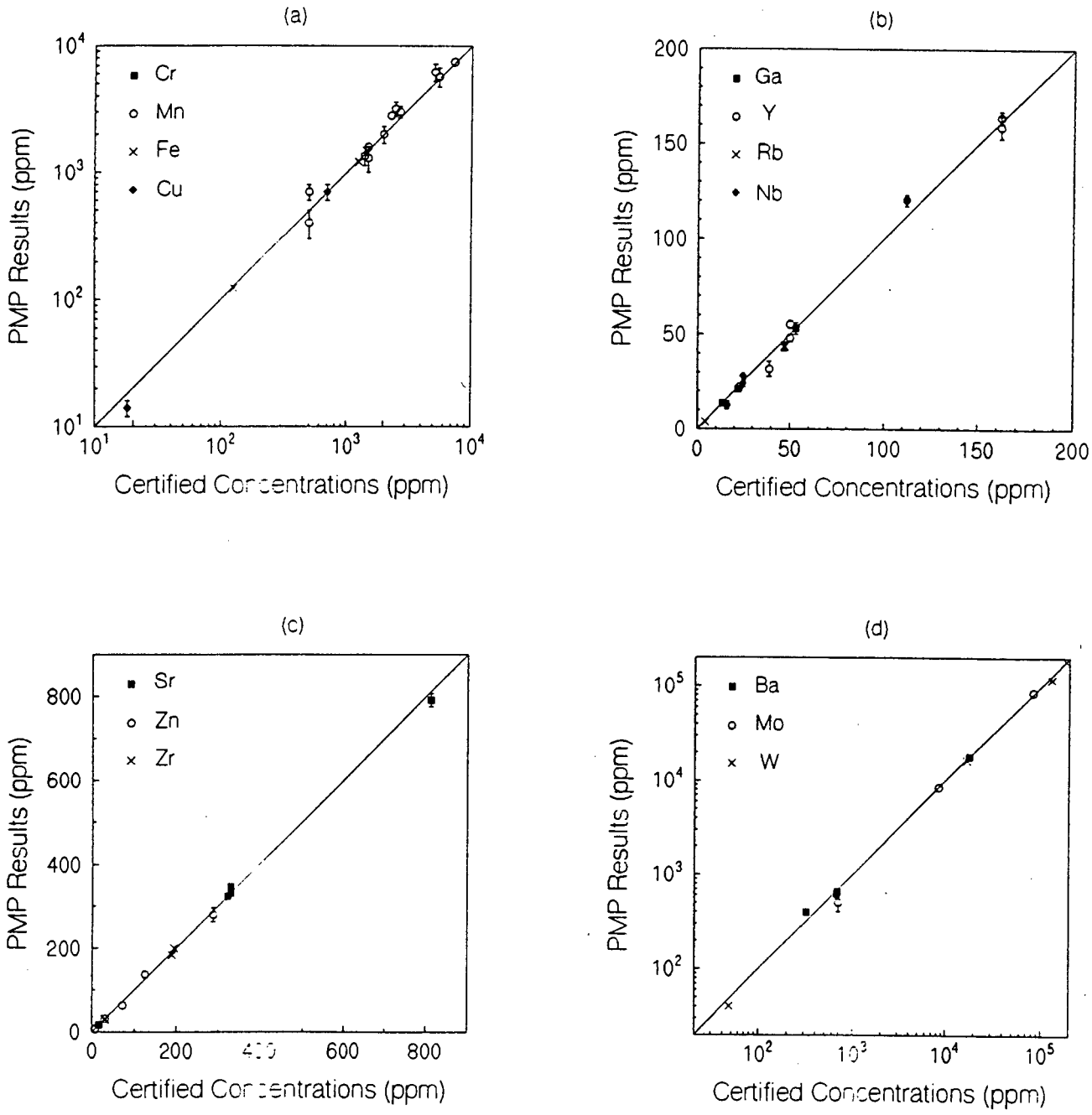

Figure 5.1: The accuracy of the proton microprobe, illustrated by plotting the known concentrations of various elements against those obtained by microPIXE analysis.

Table 5.1

Proton Microprobe Analysis of the Primary Glass Standard BCR-1 and Comparison with the Certified Values (Govindaraju, 1984) and Analysis using the CSIRO Proton Microprobe (Ryan *et al.*, 1990).

Element	Certified	CSIRO PMP	NAC PMP[a]	MDL[b]
Mn	1400	1460 ± 300	1358 ± 219	63
Fe	9.5%	9.6 ± 0.2%	9.5 %	22
Ni	13	13 ± 3	17± 5	8.5
Cu	18	15 ± 2	14 ± 2	6.3
Zn	125	124 ± 4	137 ± 8	4.6
Ga	22	23 ± 2	21 ± 1	3.9
Ge	1.5	NA[b]	ND[b]	3.3
Rb	47	43 ± 4	43 ± 2	3.9
Sr	330	343 ± 12	330 ± 8	4.4
Y	39	31 ± 4	31.6 ± 4	5.0
Zr	190	170 ± 12	183 ± 5	5.6
Nb	16	14 ± 5	13 ± 2	6.1
Ba	680	628 ± 90	652 ± 51	100
La	26	NA[b]	183 ± 51[c]	110
Ce	53	NA[b]	199 ± 50[c]	131
Pb	15	11 ± 4	16 ± 3	6.7

(a) Result of a sum spectrum from 6 spot analyses (total integrated charge Q = 6 μC), collected using a 3 MeV H^+ beam and normalized to the certified Fe concentration. All values are reported as ppm unless otherwise indicated.

(b) NA = not available, ND = not detected, MDL = minimum detection limit (99 % confidence level).

(c) The error in La and Ce concentrations is attributed to the low statistics of the peaks, explained fully in the text.

Table 5.2

Proton Microprobe Analysis of the Secondary Mineral Standard H8 (Hornblende) and Comparison with the Analysis using the CSIRO Proton Microprobe (C. G. Ryan, unpubl. data).

Element	CSIRO PMP	NAC PMP[a]	MDL[b]
Mn	0.51 %	0.62 ± 0.10 %	43
Fe	16.4 %	16.4 %	15
Zn	288 ± 21	279 ± 17	3.0
Ga	53 ± 3	53 ± 3	2.5
Ge	4.3 ± 0.6	6.3 ± 1	2.1
Sr	17 ± 1	17 ± 2	2.1
Y	162 ± 4	159 ± 6	2.3
Zr	30 ± 1	28 ± 2	2.5
Nb	25 ± 0.8	24 ± 2	2.7
W	48 ± 9	40 ± 10	8.5

(a) Results of the sum spectra of 12 point analyses to a total integrated charge of 19 μC, collected using a 3 MeV H^+ beam and normalized to the electron microprobe Fe concentrations (C. G. Ryan, unpubl. data). All values are reported as ppm unless otherwise indicated.

(b) MDL = minimum detection limit (99% confidence level).

5.2.2 Spectral Overlap

Spectral overlap is treated by the spectrum fitting program PIXE FIT (Ryan *et al.*, 1990), which varies the line area of one X-ray line of a particular element as the free

parameter p. The relative intensities r1, r2, ... rn, which are precalculated by the program LAYER (Cousens *et al.*, 1987) then relates to the peaks by p.r1, p.r2, ... p.rn. For each element this pattern of peak intensities is different, and it is this fact that enables the resolution of spectral overlaps. For example, even though the Sr K_{β} overlaps almost exactly with the Zr K_{α}, the other lines of Sr and Zr are very different, and the fit therefore converges on the correct element, Sr or Zr.

In some cases trace element X-ray lines are completely swamped by the X-ray lines resulting from the presence of major or minor elements, and spectral overlap is impossible to resolve. Analysis of the steel standards NBS D838 and D840 (Table B1, Appendix B) has shown how spectral overlap can effect quantitative results. The standards, consisting mostly of Fe, also contains Cu, Co and W. The Cu K_{α} line overlaps with the Co K_{β} line, and both the Cu K_{α} and K_{β} lines are swamped by the W L lines. The concentration of Cu in both samples is small compared to the concentrations of Co and W, and therefore, large errors in the Cu concentrations are introduced: 47% in sample D838 and 67% in sample D840. The larger error in the latter is due to the larger relative concentrations of Co and W in the sample. In contrast, sample D841, that does not contain Co, shows no error in the Cu content.

A similar problem was encountered during the analyses of two minerals in a garnet websterite sample JJG 1424 (Table B3, Appendix B). Here, erroneous results for the Ni and Co concentrations of the garnets and the Co concentrations in the orthopyroxene were obtained due to the presence of spectral overlap. Both the Ni and Co K_{α} lines are strongly obscured by the high intensity Fe K_{β} line. The Co K_{β} line

overlaps with the Ni and Cu K_{α} lines, and the Ni K_{β} lines with the Cu and Zn K_{α} lines. Hence, in this work, Co concentrations in silicates, are not reported. Similarly, at the proton microprobe laboratory of the CSIRO Division of Exploration and Mining in Sydney, Australia, trace Co results are not reported if they occur in samples containing major Fe and high trace Ni (C.G. Ryan, pers. comm.).

The problem of spectral overlap can be solved in part by the use of a Si(Li) detector of higher resolution. The Canberra detector used for these analyses is characterized by poor resolution but was the only detector available to the author at the time of these experiments. A detector of considerably better resolution has in the meantime been purchased and calibrated, a result of which is a considerable improvement in the quantitative results for trace Ni in the presence of major Fe.

5.2.3 Low Statistics Peaks[19]

Ryan *et al.* (1988) found that in the mid-energy regions, e.g. Ni through to Nb, low statistics did not pose a significant problem and that results at or just below the minimum detection limit (MDL) showed good agreement with the certified concentrations of the standards that were analyzed. However, the X-rays in the high energy regions with wide peaks and low statistics yielded erroneous results. Errors introduced due to low statistics must therefore be particularly guarded against in the high X-ray energy regions.

---

[19] Low statistics = low intensity peaks, i.e. the X-ray line in the spectrum contains a relatively small number of X-ray counts.

An example of how low statistics peaks effect quantitative results is illustrated by the analysis of a US Geological Survey standard glass, BCR-1 (Table 5.1). The K X-ray lines of the high Z elements La and Ce have low X-ray production cross sections. In other words, for a given concentration of the element in a sample, not many X-rays are produced. The La and Ce concentrations are clearly wrong, even though they are calculated to be above the minimum detection limit (MDL). This problem is solved by improved sensitivity, discussed in section 5.4.

5.2.4 Filter Attenuation

Low X-ray energy elements are attenuated in the X-ray filters that are used commonly during routine analysis. X-ray lines are then more seriously affected by the Si-escape peaks, peak tailing and high background, than when filters are not used. This is a possible source of error, particularly when these elements are present in low concentrations. For these elements (e.g. Ca, Ti, V, Cr and Mn), a 3 % filter uncertainty is added to the final results (Ryan *et al.*, 1990).

5.2.5 Improved Accuracy by Normalization to Electron Microprobe Fe concentrations

Proton microprobe analysis of mineral grains requires the prior determination of major element compositions by the electron microprobe. The analytical accuracy of the electron microprobe is widely accepted by scientists and refined accuracy in the proton microprobe results can thus be obtained by normalizing the results to one of the major elements that also appear in the PIXE spectrum (e.g. Fe). It must, however, be

emphasized that the proton microprobe technique is an absolute technique, and that because normalization is an optional procedure used only to refine the accuracy of the results, scaling factors must always be close to one[20]. Scaling factors that differ significantly from one (e.g. 1.2 or 0.8) might obscure a number of analytical errors that should be addressed before routine analysis is initiated. Normalization therefore serves as a test of analytical accuracy.

5.2.6 Analytical Accuracy using the H_2^+ Beam

A number of geostandards were analyzed using the H_2^+ beam, and the results are presented in Tables B7 to B10, Appendix B. It can be concluded from these tables that if the H_2^+ results are normalized to the electron microprobe Fe (Tables B7 to B9) and Ca (Table B10) concentrations, high accuracy is attainable. However, scaling factors are large (between 1.3 and 1.5), and an unknown number of analytical and experimental errors (for example the errors in charge integration that are introduced due to the insufficient suppression of secondary electrons - section 4.5) are accommodated by this normalization.

---

[20] There are rare exceptions (C.G. Ryan, pers. comm.). For example, if a mineral is being analyzed that has a matrix (e.g. oxides) for which small errors in the database of absorption coefficients causes errors in the PIXE results, normalization might yield a scaling factor not equal to one. However, because the error is constant, the scaling factors have to remain precise, close to the "expected" scaling factor. PIXE results that deviate markedly from this value are rejected.

5.3 Precision

In order to correctly assess the precision of the proton microprobe, a distinction has to be made between the *experimental* and the *analytical* precision of the instrument. Experimental precision (sometimes referred to as the instrumental error) results from factors in the experimental setup that affect the reproducibility of a result, such as the beam stability and the efficiency of the charge integration. The analytical precision results solely from the effects of counting statistics, and becomes apparent when the spectrum is analyzed by the data analysis software to obtain quantitative results.

5.3.1 Experimental Precision

Experimental parameters in the proton microprobe setup, for example beam stability, charge integration and detector resolution affect the *experimental precision* of the microprobe. To assess the contribution of these effects to the overall precision, a single spot on each of three geological samples was analyzed repeatedly, and the results are presented in Table 5.3. The experimental precision is given in Table 5.3 as the relative standard deviation of the mean.

From Table 5.3, the experimental precision is best assessed by looking at an element which is present in relatively high concentration in the sample, e.g. Fe, and for which the affect of counting statistics (analytical precision) becomes negligible. In Table 5.3, the precision for the Fe results remains constant at 0.1 %, regardless of its concentration in the sample. This value is assigned for the experimental precision of the NAC proton microprobe.

Table 5.3

The results of the repeated analyses of single points on three geological samples, and the assessment of the precision of the NAC proton microprobe. $\bar{x}$ = arithmetic mean concentration in ppm (unless indicated as wt%), S = standard deviation in ppm (unless indicated as wt%) and Prec. = % precision.

	Mn	Fe	Zn	Ga	Y	Zr
			ROM 242 (Garnet Megacryst), n = 10			
$\bar{x}$	2370	9.4 %	31	19	41	109
S	93	.0096%	2.2	1.5	3.2	3.6
Prec.	3.9 %	0.1 %	7.1 %	8.2 %	7.8 %	3.3 %
			EVA 09 (Garnet Megacryst), n = 10			
$\bar{x}$	2440	9.1 %	28	18	42	109
S	79	.0086%	2.5	1.1	3.1	5.8
Prec.	3.2 %	0.1 %	8.9 %	6.1 %	7.4 %	5.3 %
			ROM 218 (Olivine Megacryst), n = 10			
$\bar{x}$	1710	15 %	186	-	-	5.2
S	174	.0153%	2.1	-	-	1.1
Prec.	10 %	0.1 %	1.1 %	-	-	21 %

5.3.2 Analytical Precision

A *single* point analysis using the proton microprobe is subject to a certain degree of uncertainty (error), arising solely from the effects of *counting statistics* on the final results.

This uncertainty or error is inherent to the microPIXE technique, and is referred to in this study as the *analytical precision* of the proton microprobe. The most important factors that affect the counting statistics, and ultimately the analytical precision of the proton microprobe, are (a) the actual concentration of the element in the sample (note how the precision for the Mn and Zn results in Table 5.3 is negatively correlated with the respective concentrations of these elements in the samples), (b) the X-ray yield of the element[21] and (c) spectral overlap.

The PIXE results as fitted and reduced by the GeoPIXE software package (Ryan *et al.*, 1990), are presented with a 1σ error bar. The error estimate takes into account the factors listed above, and is reflected in the uncertainty of the least squares fit to the raw data. A 3% filter attenuation uncertainty is included if filters were used, to accommodate possible uncertainties in the database of absorption coefficients.

Proton microprobe analysis was applied in this study to a suite of Roberts Victor eclogites and kyanite eclogites. The percentage analytical precision of the trace element results obtained by the analyses of several garnets, clinopyroxenes and the kyanites are plotted as three histograms in Figure 5.2. The results exclude the 3% filter uncertainty, added to the low X-ray energy elements, in order to assess the true analytical precision across the entire X-ray energy range of interest. From the histograms, the affect of counting statistics on the analytical precision is clearly apparent.

---

[21] The X-ray yield depends on the X-ray production cross-section, which decreases with increasing X-ray energy. Accordingly, precision decreases towards higher X-ray energies.

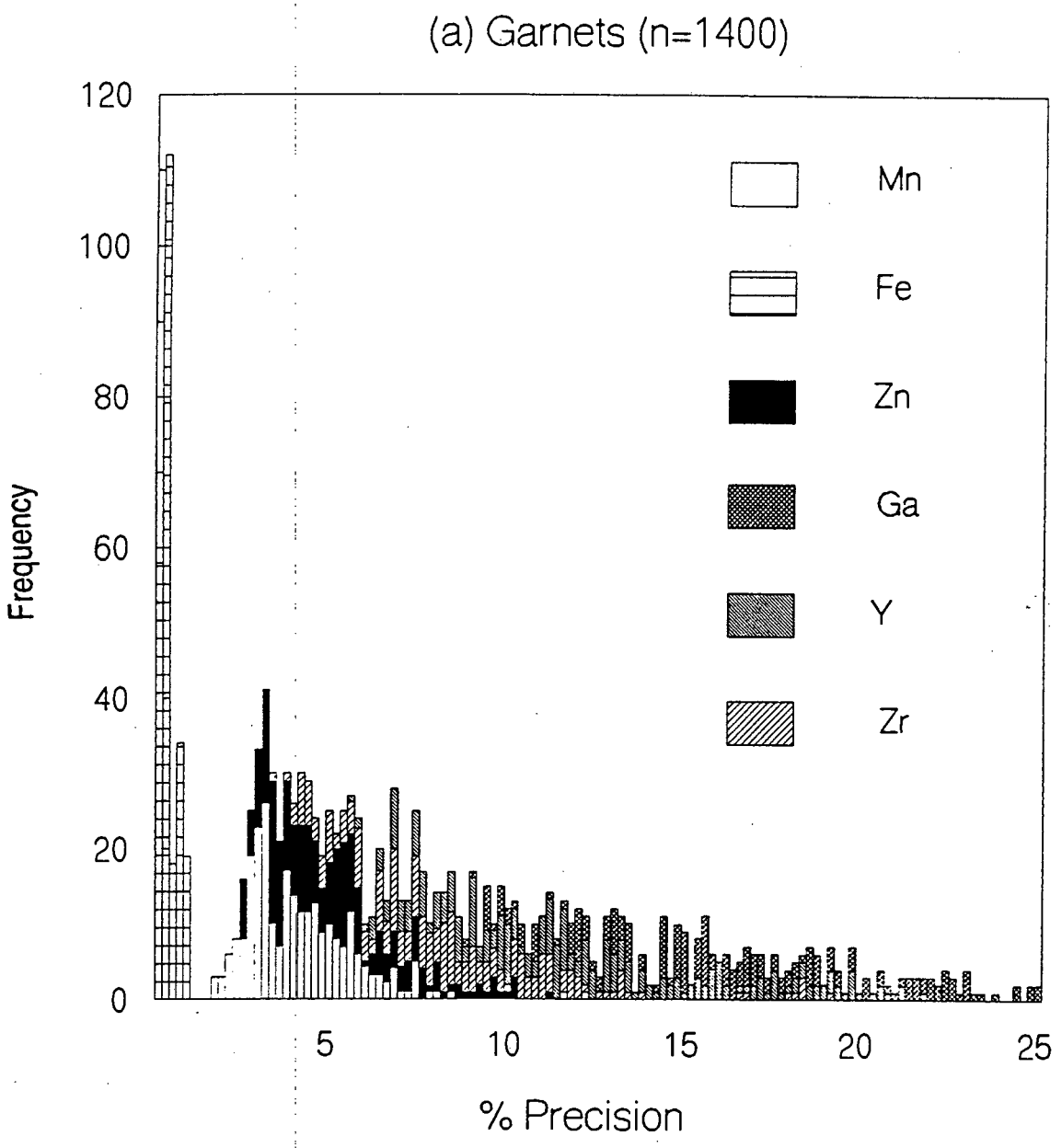

Figure 5.2: (a) Histogram of the percentage analytical precision obtained by the proton microprobe analysis of garnet grains. Note how the precision is strongly dependent on the element and its concentration in the sample. For example, the major element Fe, which has orders of magnitude more counts in the peaks, shows much better precision than the trace element Ga. Continued on the next page.

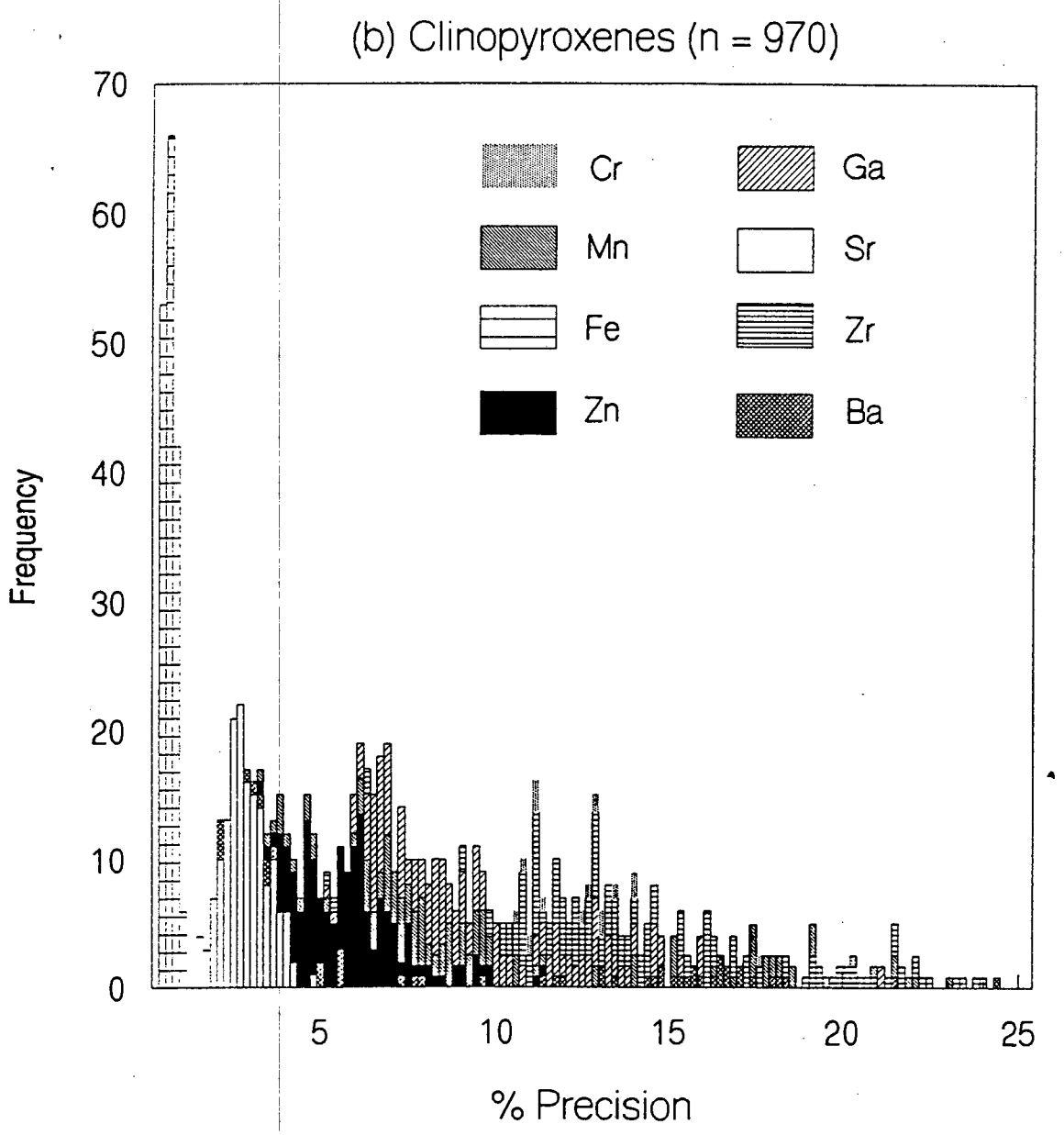

Figure 5.2 (continued): (b) Histogram of the percentage analytical precision obtained by the analysis of clinopyroxene grains. Again it is clear that the precision depends on the concentration of the element in the sample. Continued on the next page.

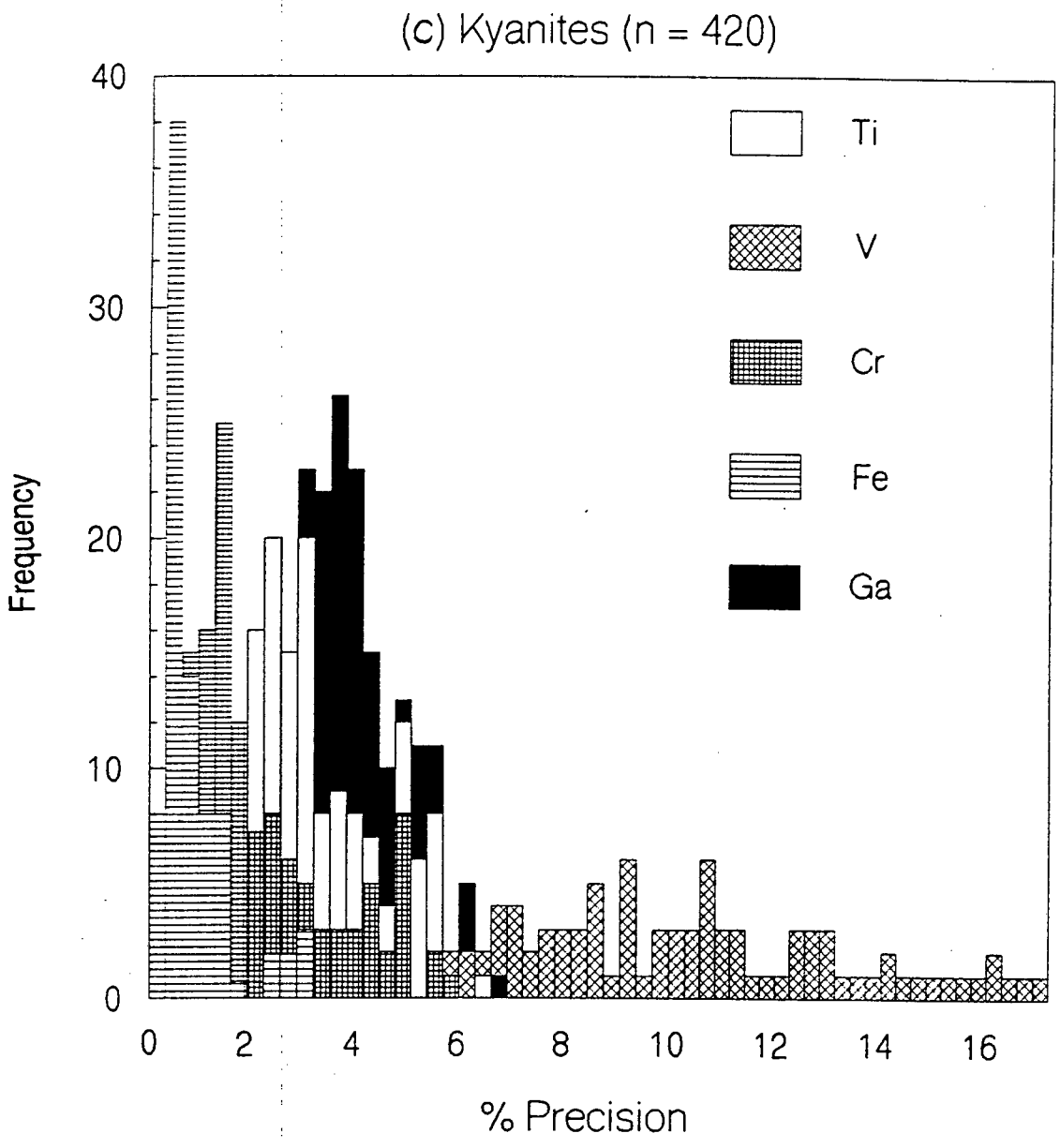

Figure 5.2 (continued): (c) Histogram of the percentage analytical precision obtained by the analysis of kyanite grains. Again it is clear that the precision depends on the concentration of the element in the sample. In this case, Fe is not a major element, but it is present in high trace concentrations (e.g. 0.1 to 0.2 wt%), as opposed to, for example, V, which is generally less than 100 ppm. As a result, Fe shows better precision.

5.4 Sensitivity

The sensitivity of the microPIXE technique is largely dependent on the peak-to-background ratio for a particular element and may be defined as the minimum detection limit (MDL) at the 99% confidence level, where (Currie, 1968):

$$MDL = 3.29 \sqrt{B}, \text{ (B = background)} \qquad (5.1)$$

Best sensitivity is obtained by long analysis times and close detection geometry.

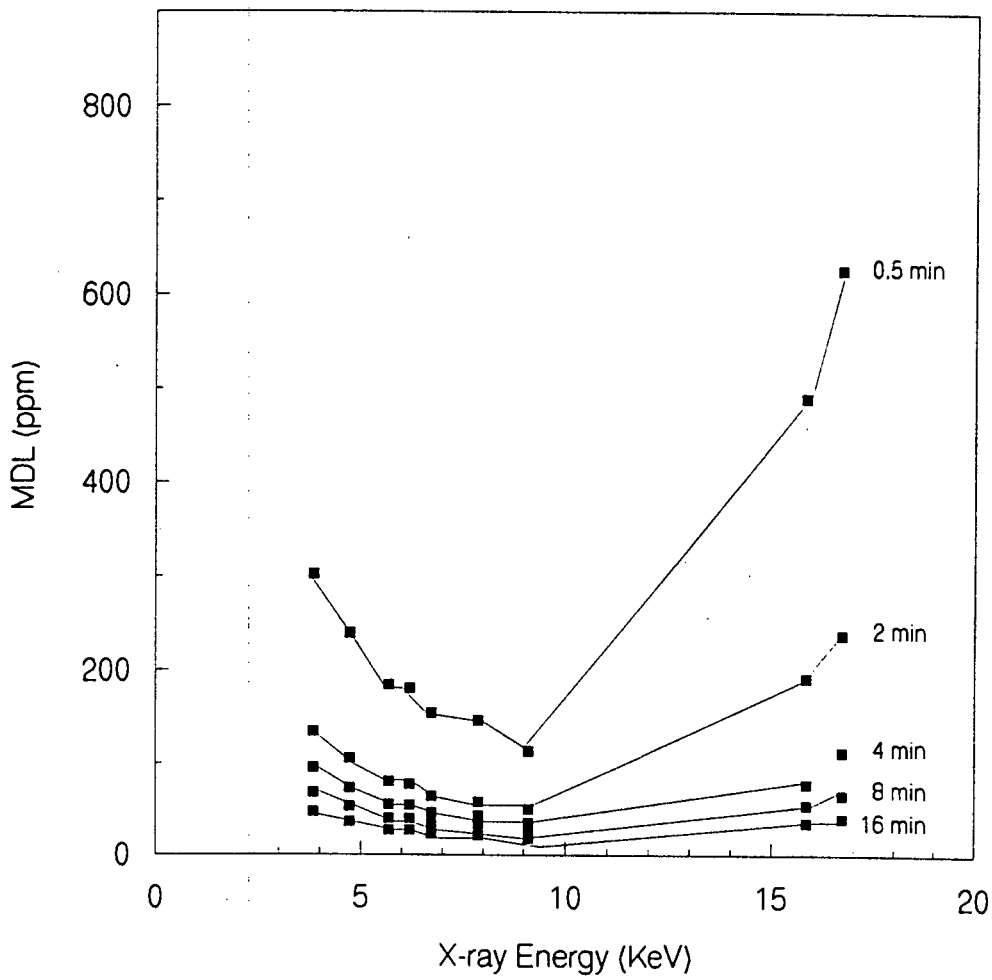

Figure 5.3: The variation in minimum detection limits at different analysis times. These curves were obtained by the analysis of a garnet megacryst, using a 3 MeV H^+ beam and a 40 μm Al filter.

Analysis times depend on the nature of each project and must be assessed by the analyst. Figure 5.3 shows how longer analysis times improve the detection limits. However, the sensitivity only increases by the square root of the increase in analysis time. Therefore, once acceptable detection limits have been reached, analysis times should be kept within reason (e.g. 5 to 8 minutes) during routine analysis. *Detection geometry* is a fixed part of the proton microprobe setup, and once the closest possible geometry is obtained, this must not be changed.

Sensitivity may be improved further by *selective filtering*. During routine analysis using the NAC proton microprobe, Al filters are commonly used to filter out the large number of counts resulting from the presence of major elements (e.g. Ca and Fe). This reduces unwanted pileup effects at higher energies in the spectrum and effectively lowers the detection limits. This is illustrated in Figure 5.4. A further example of selective filtering (Ryan *et al.*, 1990) is the simultaneous use of a 400 μm Al filter and a 25 μm Fe filter to reduce Ni and As pileup during the analysis of nickeline (NiAsS). The detection limit of trace Pd in the sample was improved considerably.

Johansson (1991) investigated the effects of *different beams and beam energies* on the sensitivity of PIXE. Better sensitivity was obtained using a 5 MeV α-particle beam compared to a 1.8 MeV H^+ beam, over a restricted X-ray energy range. The experiments were done using a large, unfocused beamspot (PIXE), and although the same results are expected for microPIXE, this could not be pursued due to the inability of the current beam focusing equipment at NAC to focus a 5 MeV α-particle beam to the small spot sizes that are required. A disadvantage of the α - particle beam is the difficulty in obtaining high beam currents, which would necessitate long analysis times.

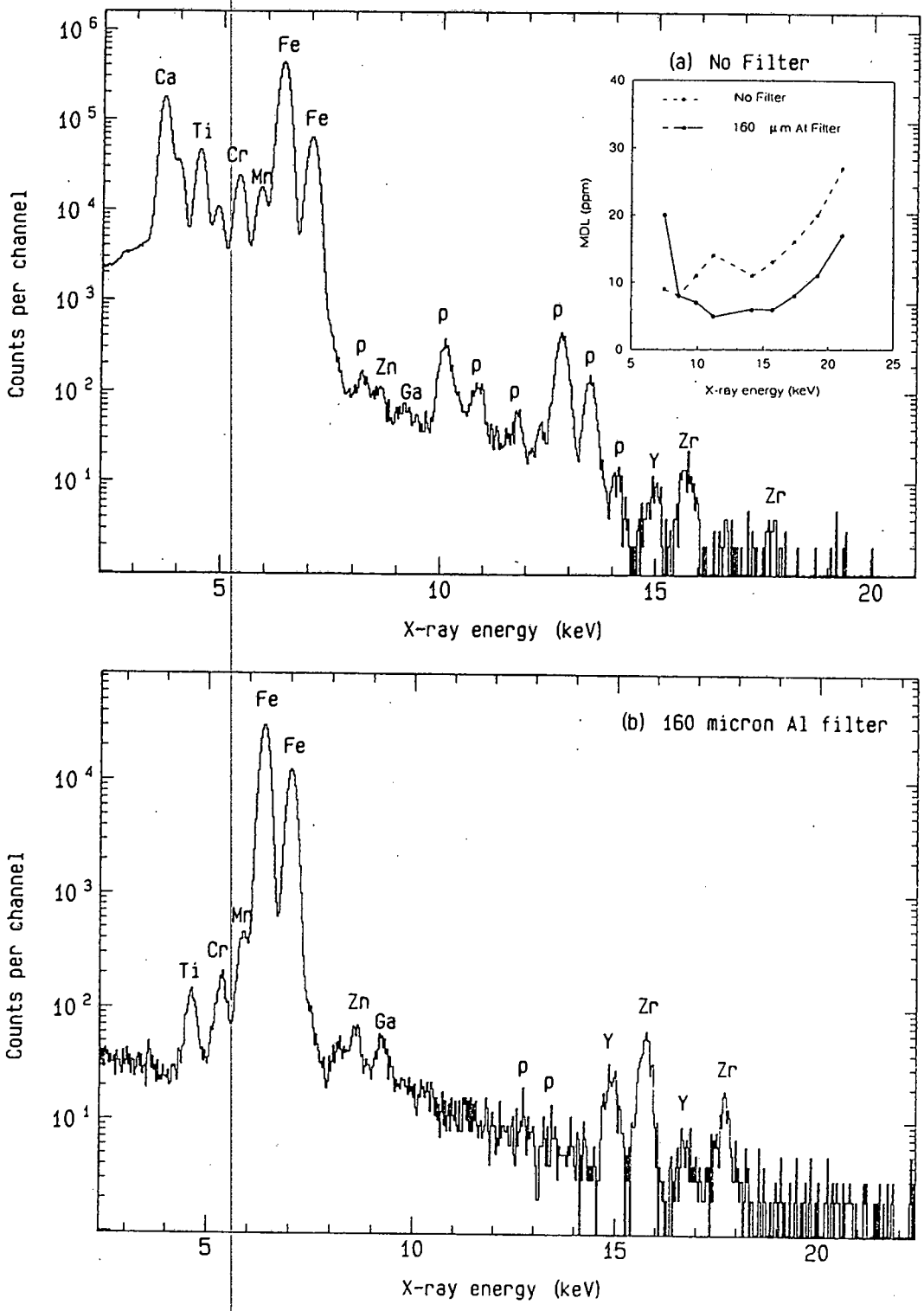

Figure 5.4: Improved sensitivity of the NAC proton microprobe is obtained by the use of various Al filters. (a) and (b) are spectra of the same sample, collected without and with an Al filter. The inset shows how this lowers the detection limits for elements with Z higher than Fe. The reduced sensitivity at the lower X-ray energies is a result of the severe attenuation of these elements by the filter.

CHAPTER 6

AN APPLICATION OF THE PROTON MICROPROBE

6.1 Introduction

The analysis of many known standards, that were described in the previous chapters of this work, showed that the National Accelerator Centre proton microprobe can be used successfully for quantitative analysis. However, the usefulness of any analytical technique only becomes apparent when it is applied to natural samples of unknown trace element composition. In cognisance of the research interests at the University of Cape Town, a suite of eclogites and kyanite eclogite xenoliths from the Roberts Victor kimberlite, Northern Cape, South Africa, were selected for analysis to illustrate the use of the proton microprobe in elucidating problems in mineralogy. These samples have been studied previously by Hatton (1978) and Kirkley *et al.* (in press) who determined major element compositions, and by Kirkley *et al.* (in press) who analyzed trace elements including rare earth elements (REE) by ion microprobe. The proton microprobe results presented here complement this database with additional trace element data.

The kyanite-bearing eclogites can be divided into two groups; (a) inhomogeneous (layered) and (b) homogeneous. The emphasis was placed on the analysis of the layered kyanite eclogites, which are characterized by layers of kyanite-bearing eclogite, bounded

by Group I bimineralic eclogite[22]. The homogeneous samples, which exhibit a more or less equal distribution of kyanite throughout the nodule and the absence of the distinct layering, were analyzed for comparison.

Gross chemical differences between the bimineralic eclogite and kyanite eclogite layers is a feature of the layered samples (Lappin and Dawson, 1975; Hatton, 1978; Kirkley *et al.*, in press). The kyanite eclogite whole rock is considerably richer in CaO, Al_2O_3 and Na_2O, and poorer in MgO, MnO and FeO (Kirkley *et al.*, in press), in comparison to the bimineralic eclogite whole rock. The change in garnet compositions at the contact is rapid, as detailed electron microprobe analyses show sharp chemical gradients across a distance of approximately 1 cm (Lappin and Dawson, 1975; Hatton, 1978; Kirkley *et al.*, in press). As an application of the technique, the proton microprobe was used in this study to obtain the representative trace element compositions of the minerals in the various layers, and to investigate whether or not the chemical differences in the minerals of the different zones, and the chemical gradients in the garnets at the contacts are imitated by the trace elements, and whether they are resolvable within the precision of the proton microprobe.

Three layered kyanite eclogite samples, HRV 17, HRV 30 and JJG 177 were selected for trace element analysis by the proton microprobe. The samples are shown in the work by Hatton (1978), and schematically in Figure 6.1. The relative positions of the thin sections that were cut and analyzed are shown in Figure 6.1.

---

[22] The classification as Group I is based on the major element data of Kirkley *et al.* (in press) and the classification scheme of McCandless and Gurney (1989): Group I eclogites contain greater than 0.09 wt% Na_2O and 0.08 wt% K_2O in the garnets and clinopyroxenes, respectively.

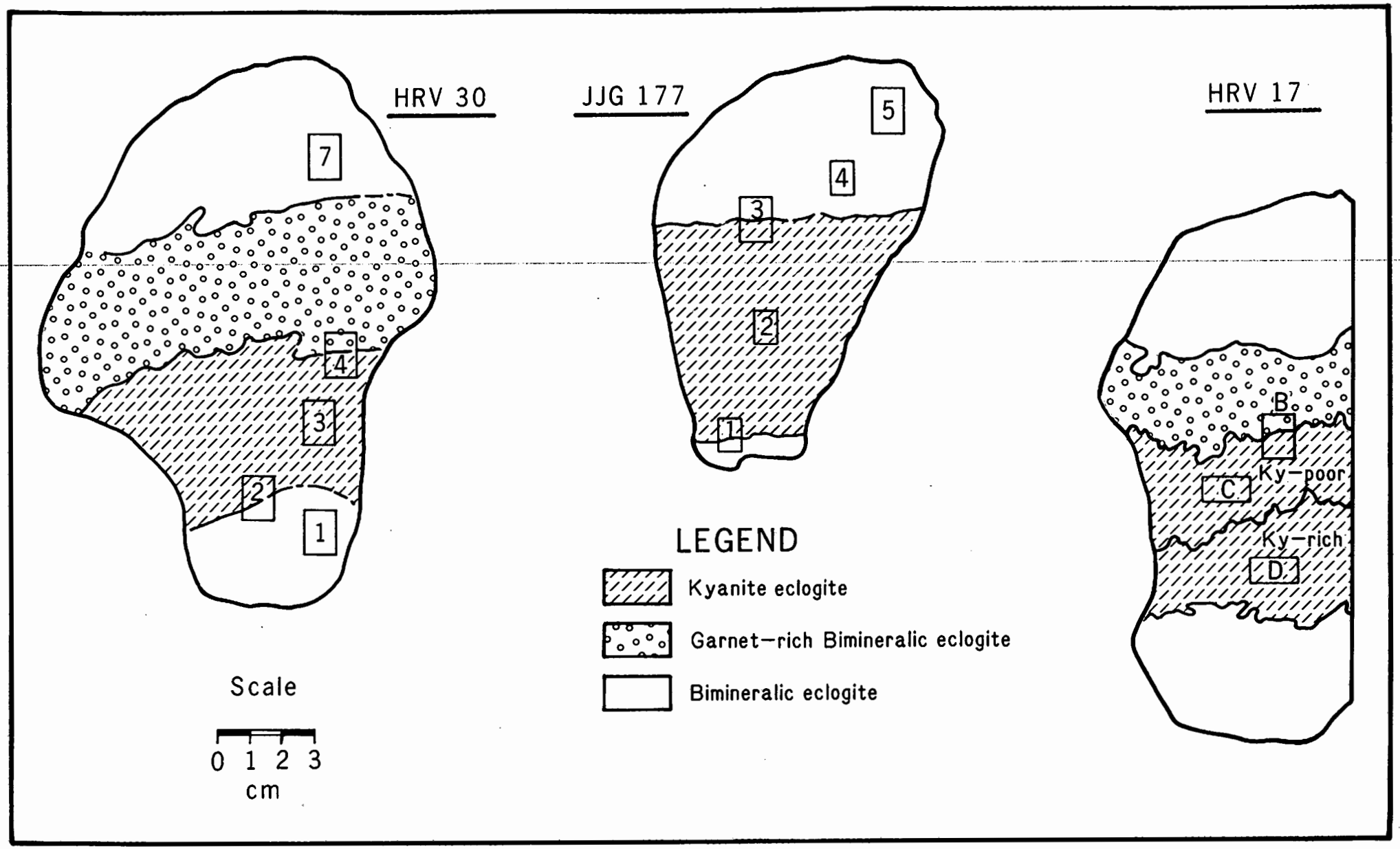

Figure 6.1: Schematic representation of the layered kyanite eclogites analyzed in this study. The relative positions of the thin sections that were selected for proton microprobe analysis are shown. The drawings for HRV 30 and JJG 177 were modified after Kirkley *et al.* (in press) and for HRV 17 after Hatton (1978).

The chemical compositions of the minerals that occur in the homogeneous kyanite eclogites are similar to those in the kyanite zones of the layered samples. The garnets are rich in Ca, always containing more than 10 wt% CaO (Hatton, 1978). The clinopyroxenes are characterized by high Al_2O_3 content which is always more than 16 wt% (Hatton, 1978). Two homogeneous kyanite-bearing eclogites (JJG 4 and PJL 17) were analyzed for comparison.

The bimineralic eclogites that bound the kyanite eclogite layers are texturally similar to other Group I eclogites, consisting of rounded orange garnets and dark clinopyroxenes in variable modal proportions. Distribution of the minerals is generally inhomogeneous and garnet- and clinopyroxene-rich patches within the bimineralic eclogite are common.

The kyanite eclogite is distinctive in having a turbid mass of altered white material (≈ 30 to 40 modal %), which has replaced clinopyroxene and consists of plagioclase, secondary clinopyroxene, nepheline and glass (Switzer and Melson, 1969; Lappin, 1978). In accordance with Kirkley *et al.* (in press), this material will be referred to as "altered clinopyroxene" in the discussions that follow. Brown or black rounded garnet grains, (≈ 50 to 60 modal %), and blue kyanite (≈ 5 to 15 modal %), constitute the remainder of the kyanite eclogite zones. The rounded to slightly elongate kyanite grains occur as free kyanite in the mass of altered clinopyroxene as well as inclusions in the garnet grains.

The xenolith surfaces are eroded toward the kyanite eclogite zones, indicating the more pronounced susceptibility to chemical and mechanical attack of these layers by the

kimberlite magma, relative to the bimineralic eclogite.

Primary minerals from a number of Group I and Group II eclogites, unrelated to the kyanite eclogite, were analyzed by proton microprobe. The results are given in Table C6, Appendix C. The samples, from the Hatton (1978) study, were chosen to represent a wide variety of different eclogite types, and the analyses were done in order to contrast mineral compositions of the Group I and Group II eclogite, and the mineral compositions in the Group I bimineralic eclogite associated with the kyanite-bearing eclogites. The study of trace element signatures of these samples was secondary to the main study of trace element patterns of the inhomogeneous kyanite eclogites.

6.2 Analytical Results

6.2.1 Running Conditions

The analyses of the geological samples were carried out using a 3 MeV proton beam. Although the analyses were spread over a time interval of several months, the beam-on-target current was always between 5 and 15 nA, with a typical spot size of approximately 10 μm or defocused up to 100 μm in diameter for the analyses of the altered clinopyroxene. The secondary electron suppressor voltage was constant at -1 kV.

X-ray detection was achieved using a Canberra Si(Li) energy-dispersive detector, with a Si(Li) crystal area of 30 mm^2, a crystal thickness of 2.5 mm and a target-to-detector distance of 36 mm.

The large number of Fe X-rays excited in the garnet and clinopyroxene grains caused high dead-time and pile-up peak contamination of the spectrum. A 160 μm thick Al filter was therefore used to attenuate Fe X-rays, which reduced the effects of these artifacts considerably.

The microPIXE spectrum of a kyanite analysis does not contain high intensity major element peaks, and the use of a thick filter is therefore not required. A 40 μm Al filter was used for these analyses. This attenuates the background in the low X-ray energy region, but still allowed the detection of lighter trace elements such as Ca, Ti and V (which would otherwise be attenuated by a thick filter).

6.2.2 Presentation of Data

With the exception of the kyanite analyses, and the analyses of the garnets at the contact zones, trace element results were normalized to the electron microprobe Fe results[23]. Analyses with scaling factors > 1.02 and < 0.97 were rejected (this procedure is discussed fully in section 5.2.5). Quantitative Ni and Co results lacked precision due to spectral overlap and these values are not reported (discussed in section 5.2.2).

If zoning profiles and subtle chemical differences within or between particular mineral grains are not observed, it is a common analytical procedure to mathematically calculate the *average* elemental concentrations from a data set of several analyses. This

[23] The contact zones are characterized by chemical gradients, including Fe. Normalization to one average Fe concentration would obscure subtle chemical gradients in the trace element concentrations and would defeat the purpose of the experiment.

ensures accurate sampling of the typical mineral composition across the polished section. During proton microprobe analysis this entails the fitting of each spectrum individually, the calculation of the elemental concentrations and the mathematical determination of the arithmetic mean concentration from these numbers. The same results can, however, be obtained by *summing* all the raw spectra of the data set together and calculating the elemental concentrations from a single high statistics spectrum. The results thus obtained are representative of the typical mineral composition and are characterized by lower detection limits and improved precision. This is illustrated in Table 6.1, where the typical kyanite trace element compositions of polished section HRV 30-3 are given as, firstly, the arithmetic mean concentration and standard deviation of 18 analyses (column a) with their average detection limits (column b) and secondly, the results obtained by fitting a single, high statistics sum-spectrum and calculating the trace element concentrations from the measured peak areas (column c) and the associated detection limits (column d). Note the improved sensitivity and precision in the latter in Table 6.1.

Representative clinopyroxene and garnet trace element compositions are given in Tables 6.2 and 6.3 respectively. In both cases, a set of results from each of the two different eclogite types are given for comparison: columns (a) represents analyses from the kyanite-bearing eclogite, and columns (b) from the kyanite-free eclogite. All results were obtained from sum-spectra. All other trace element results are presented in Tables C1 to C6, Appendix C.

The homogeneity of the distribution of the trace elements in the sample can be assessed by the ratio of the standard deviation for the data set (σ_h) to the statistical

(analytical) error (σ_s) for a single analysis. For homogeneously distributed elements, this ratio should approach one. Ryan *et al.*(1990) found that, in general, if $\sigma_h/\sigma_s \geq 2$, scatter in results can be attributed to sample heterogeneity.

Table 6.1

Representative kyanite trace element chemistry of polished section HRV 30-3. A comparison is made between the arithmetic mean concentration and standard deviation of 18 analyses, and the results obtained from a single high statistics sum-spectrum. All values are reported as ppm, and the abbreviations are as follows: Elem = element, MDL = minimum detection limit (99% confidence level).

Elem	σ_h/σ_s	(a) Arithmetic mean & standard deviation	(b) Mean MDL	(c) Sum-spectrum results and 1σ error	(d) MDL
Ca	2.4	160 ± 80	107	104 ± 11	25
Ti	2.6	586 ± 24	18	568 ± 3.1	4.3
V	1.2	70 ± 6.2	10	67 ± 3.6	2.5
Cr	3.5	579 ± 18	6.4	579 ± 2.4	1.5
Fe	24	1230 ± 142	3.3	1230 ± 4.1	0.8
Ga	1	33 ± 1	2.2	32 ± 0.4	0.5

Table 6.2

Representative clinopyroxene trace element chemistry of polished sections JJG 177-2 (kyanite-bearing eclogite) and JJG 177-4 (kyanite-free eclogite). The results were obtained from the sum-spectra of 12 and 20 analyses respectively. All values are reported as ppm unless indicated as wt %, and the abbreviations are as follows: Elem = element, MDL = minimum detection limit and ND = not detected (rejected from sum-spectrum fit).

	(a)			(b)		
Elem	σ_h/σ_s	**Kyanite Eclogite**	**MDL**	σ_h/σ_s	**Kyanite-free Eclogite**	**MDL**
Mn	2.1	224 ± 8.5	14	1.2	829 ± 32	17
Fe	-	1.7 % ± 81	5.5	-	4.0 % ± 202	6.9
Zn	3.6	56 ± 1.2	1.5	1.1	45 ± 0.63	1.3
Ga	1.7	23 ± 0.54	1.3	1.6	14 ± 0.37	1.3
Sr	15	173 ± 2.1	1.3	2.4	300 ± 5.4	1.2
Y	-	ND	1.4	1.4	1.9 ± 0.32	1.3
Zr	2.4	17 ± 1	1.6	0.90	36 ± 1.1	1.4
Ba	3.5	321 ± 24	52	-	ND	39

Table 6.3

Representative garnet trace element chemistry of polished sections HRV 30-3 (kyanite-bearing eclogite) and HRV 30-7 (kyanite-free eclogite). The results were obtained from the sum-spectra of 27 and 15 analyses respectively. All values are reported as ppm unless indicated as wt %, and the abbreviations are as follows: Elem = element, MDL = minimum detection limit and ND = not detected.

	(a)			(b)		
Elem	σ_h/σ_s	**Kyanite Eclogite**	**MDL**	σ_h/σ_s	**Kyanite-free Eclogite**	**MDL**
Cr	1.3	709 ± 55	77	0.6	211 ± 90	122
Mn	1.4	1460 ± 32	21	0.9	2530 ± 45	39
Fe	-	8.6 % ± 193	7.4	-	11 % ± 201	16
Zn	1.8	64 ± 0.58	1.4	1.3	54 ± 1.2	2.2
Ga	2.1	12 ± 0.34	1.3	1.7	4.8 ± 0.42	1.9
Sr	4.4	7.7 ± 0.36	1.0	-	ND	1.5
Y	1.6	10 ± 0.36	1.1	1.9	16 ± 0.87	1.6
Zr	3.2	40 ± 0.63	1.2	3.0	33 ± 0.87	1.7

6.2.3 Discussion

The dependence of the precision and sensitivity of the proton microprobe data on the nature of the matrix and the elemental abundances in the sample is clearly reflected in the results obtained from the analyses of the eclogites. For example, the

histogram in Figure 5 (a) show that the analytical precision[24] for Ga in garnet (approximately 12 ppm) varies from 9 to 25 %. The same element occurring in a higher concentration in kyanite (approximately 32 ppm) shows considerably better precision, at 3 to 6 % (Figure 5(c)). This illustrates that the dominant effect on the precision for low-level traces is simply counting statistics.

The effect of the nature of the matrix on the precision is apparent from the analyses of garnet and fresh clinopyroxene in a kyanite eclogite sample. The sum spectra of the data sets yielded 552 ± 17 ppm Cr in clinopyroxene (precision = 3 %) and 886 ± 138 ppm Cr in garnet (precision = 16 %). The clinopyroxene data thus shows better precision in spite of the slightly lower Cr content.

As an element of low X-ray energy, Cr results are affected by matrix and filter absorption, and the intensity of the continuum background below the peaks. Since these analyses were carried out under identical experimental conditions, with the use of the same Al filter, the large difference in the precision of the results is attributed to the difference in the matrices. The higher mean atomic number of garnet in comparison to that of clinopyroxene results in increased attenuation of the Cr X-rays as they passed from depth in the sample, through the matrix to the detector. The result is a lower Cr X-ray yield in the garnet, and degraded precision resulting from the poorer counting statistics. The heavier garnet matrix also gives rise to an increase in the continuum background, affecting not only the precision, but also the detection limits. The detection limit of Cr in garnet for this example is 117 ppm in comparison to only 37 ppm for Cr in the clinopyroxene.

---

[24] Resulting mainly from the counting statistics.

It was shown that the summing of spectra is a useful procedure when average trace element concentrations are required. However, that is only the case for a portion of the polished sections analyzed in this work. The contact zones between the two eclogite types are characterized by chemical heterogeneity, and the changing concentrations across the contact are of interest. Therefore, single point analyses are retained, and examples of the typical average detection limits for these spot analyses are summarized below in Table 6.4.

Table 6.4:

Examples of typical average minimum detection limits for the three minerals of interest. All values are reported as ppm. A 160 μm Al filter was used for the analyses of the garnets and clinopyroxenes, and a 40 μm Al filter for the kyanites.

Element	Garnet HRV 30-4 (n = 15)	Clinopyroxene JJG 4 (n = 15)	Kyanite HRV 17-D (n = 19)
Ca	-	-	63
Ti	-	-	9.1
V	-	-	5.2
Cr	268	148	3.5
Mn	74	45	-
Fe	26	18	2.1
Zn	4.8	5.1	-
Ga	4.0	4.3	1.5
Sr	3.3	3.7	-
Y	3.6	4.0	-
Zr	3.9	4.5	-
Ba	-	141	-

The precision measured for the single point analyses of all the analyzed elements, in all three minerals of interest, are summarized in the histograms of Figure 5.2.

6.3 Geological Implications of the Proton Microprobe Results

6.3.1 Trace Element Differences between Bimineralic and Kyanite Eclogite

The proton microprobe analyses of the minerals in this study have revealed clear differences in the trace element compositions of the kyanite and kyanite-free eclogite. Examples are:

* Distinct groupings on the Zn-Zr plot of garnets in the composite xenolith JJG 177 (Figure 6.2 (a)) are present. The garnets in the kyanite-bearing zone are richer in both these elements, with the increase in the Zn concentration as much as a factor of two.

* The relatively higher concentration of Mn in the garnets of the kyanite-free eclogite in comparison to the kyanite-bearing eclogites that was originally identified by the electron microprobe is clear from the proton microprobe results. The latter data can be documented more precisely due to the greatly reduced background in the PIXE spectrum.

* Clinopyroxene grains in the bimineralic eclogite are also richer in Mn, than the altered clinopyroxene in the adjacent kyanite eclogite (Figure 6.2 (b)). The results show some scatter (σ_h/σ_s = 3.2), which reveals heterogeneity in the distribution of the Mn .

* Ga and Sr in the kyanite-bearing layer of sample HRV 30 show greater abundances in the clinopyroxenes than the same mineral in the kyanite-free eclogite (Figure 6.2 (c)). Since Ga substitutes for the major element Al, the increased concentration of Ga could be related to the increase in the jadeite component of the clinopyroxene in the kyanite eclogite.

* The kyanite compositions in the kyanite eclogite zone of sample HRV 30 change from the centre to the edge of the zone. Kyanite grains at the centre are richer in Cr and poorer in Ga than those closer to the contact (Figure 6.2 (d)).

Another significant result of the proton microprobe analyses of these xenoliths is the discovery of large concentrations of Ba (up to 0.18 wt%) in the altered clinopyroxene of the kyanite eclogite. In the fresh grains of the bimineralic eclogite, Ba concentrations are always below the limits of detection of the proton microprobe. In addition, elemental images of the kyanite zones in HRV 30 (Plate 4, Appendix A) and JJG 177 (Plate 6, Appendix A) shows the extremely heterogeneous distribution of Ba, concentrating in distinct "hot spots".

From the elemental images, the concentration of Sr in the clinopyroxene in veins in the garnet is also clearly apparent (Plates 4 and 6, Appendix A).

The trace element signatures of the minerals in the homogeneous (non-layered) kyanite eclogite samples JJG 4 and PJL 17 are similar to those in the kyanite zones of the composite xenoliths. With the exception of slightly higher Sr in some of the garnets of the composite xenoliths, no significant differences were observed between the primary minerals of the

bimineralic eclogite in the layered samples, and the Group I eclogites that are unrelated to the kyanite eclogites. Trace element grouping between the Group I and Group II eclogite were not observed.

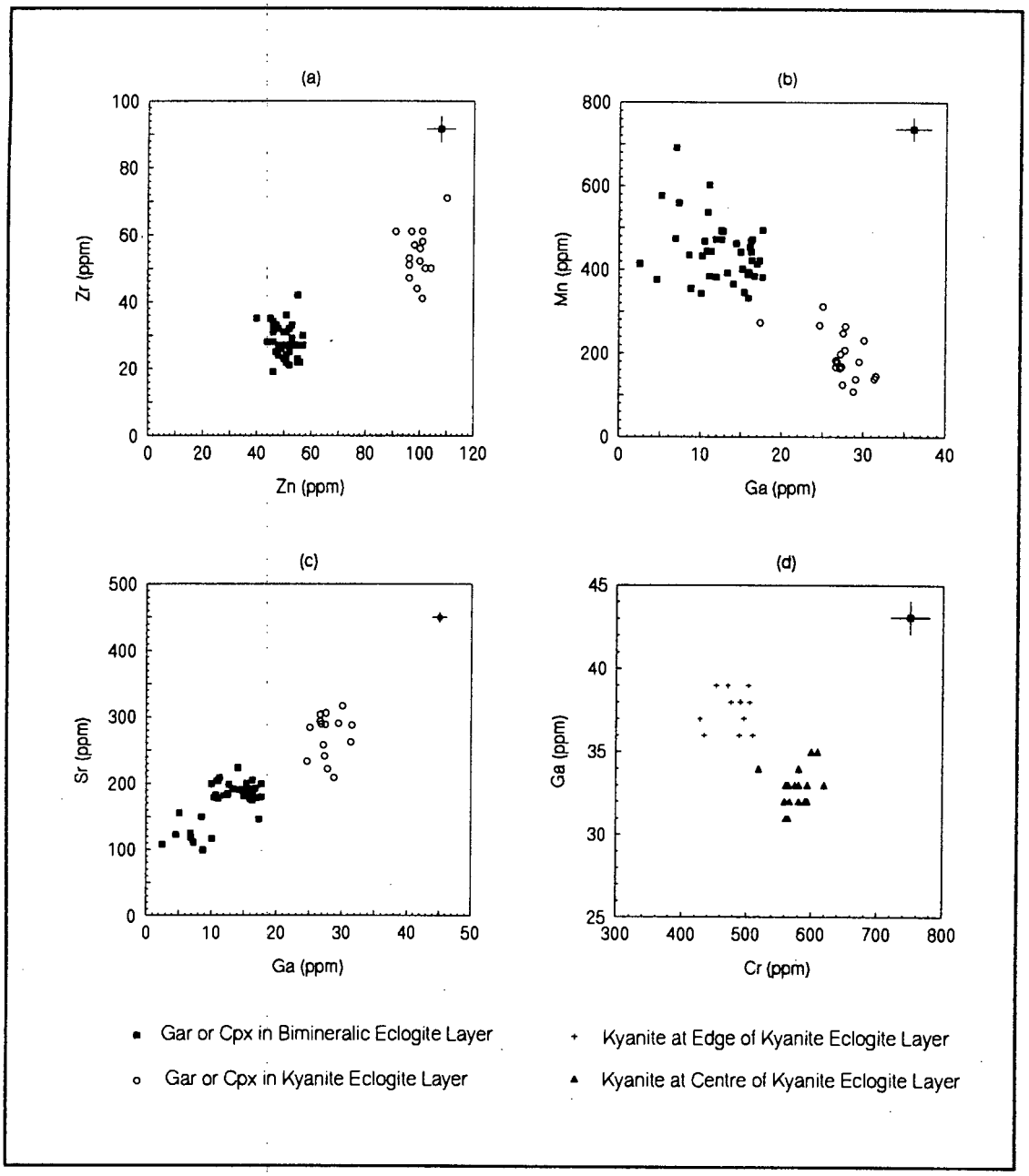

Figure 6.2: Trace element mineral chemistry of the composite eclogites, where (a) garnets; (b) and (c) clinopyroxenes, and (d) kyanites. The average error bars for each of the elements are shown in the top right-hand corner of each plot. See text for a full explanation.

6.3.2 Chemical Gradients in Garnets

Sharp chemical gradients in the major element compositions of the garnets at the contact zones of the composite eclogite samples were documented by previous workers (Lappin and Dawson, 1975; Hatton, 1978 and Kirkley *et al.* (in press)). The proton microprobe data confirm the clear decrease in Mn and Fe toward the kyanite eclogite zones, although these data show higher precision, due to the decreased background in the PIXE spectrum. The gradient in Mn can be sharp, changing rapidly over a short distance of approximately 2-3 mm (polished section HRV 30-2 - Figure 6.3 (a)), or gradational (polished section JJG 177-3 - Figure 6.3 (b)). Fe gradients are generally more gradual (polished section JJG 177-1 - Figure 6.3 (c)).

A number of clear trace element zoning profiles were identified by the proton microprobe analysis of the garnets at the contact between the two eclogite types and examples of these are shown in Figure 6.3. Most pronounced is a sharp increase in the Zn content (of the garnets) toward the kyanite zone of polished section JJG 177-1 (Figure 6.3 (d)). In the same section, Y decreases gradually toward the kyanite-bearing eclogite (Figure 6.3 (e)). Polished section HRV 30-4 (Figure 6.3 (f)) reveals a gradual increase in the Zr concentration in the garnets towards the kyanite eclogite.

6.3.3 Conclusion

From this discussion it is clear that microPIXE analysis can be used successfully in geochemistry. The precision of the technique is clearly sufficient to allow detection of

meaningful differences between and across mineral grains and would therefore be applicable to a wide variety of studies concerned with understanding trace element abundance distributions in individual mineral grains. These point analyses of small mineral grains and of chemical gradients in minerals cannot be carried out with bulk trace element analytical techniques. The clear trace element groupings and zoning profiles that were observed warrants further detailed investigation of these rare kyanite eclogite xenoliths.

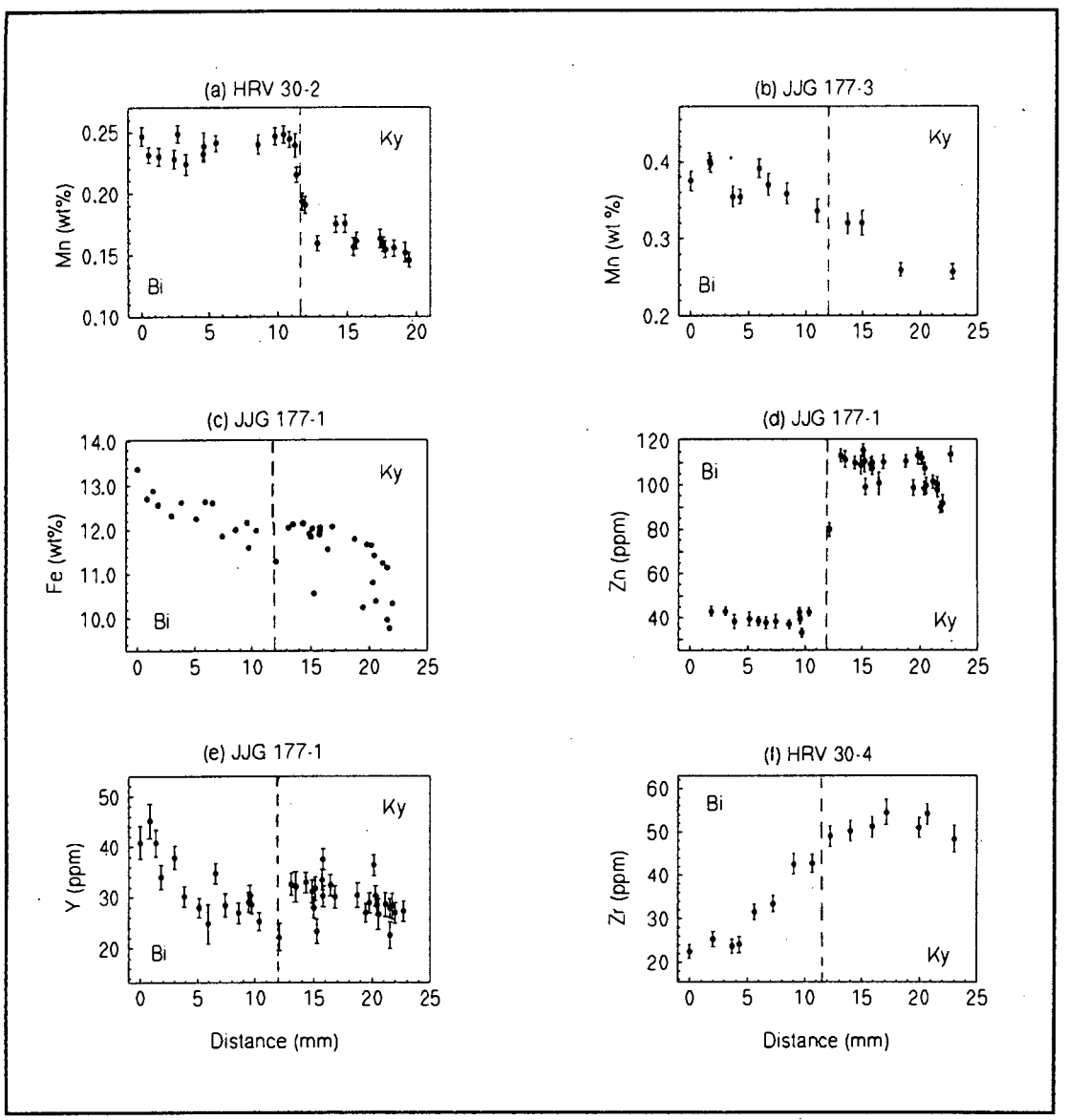

Figure 6.3: Trace element gradients in the garnets at the contact zones (contact indicated with a dashed line) of bimineralic (Bi) and kyanite (Ky) eclogite. Note the sharp changes in the Mn concentration of the garnets of polished section HRV 30-2 (a) and the Zn concentration of the garnets of section JJG 177-1 (d). All other changes are more gradational.

CHAPTER 7

DISCUSSION AND CONCLUSIONS

It was shown in the previous chapter that the proton microprobe can be used successfully in geoscience applications. Trace element compositions were obtained by the *in situ* analysis of constituent mineral grains of a suite of eclogites, using the small beam spot of the microprobe. This work revealed a number of factors that need consideration before quantitative analysis can be initiated:

* Great care is needed to set up the detection and data-acquisition systems. Accurate deadtime correction (using XSYS) and efficient electronic pileup rejection is essential.

* In the case of the National Accelerator Centre proton microprobe, where charge measurements are taken on the target ladder, a secondary electron suppressor is required. It was found that sufficient suppression of secondary electrons during the routine analysis of geological material is achieved at -1 kV, provided that the H^+ beam is used. Suppressor saturation could not be achieved using the H_2^+ beam. Hence, the H^+ beam was adopted for all quantitative work.

* Detector efficiency, specifically the detector active volume thickness and the target to detector distance, and the thicknesses of all the absorbing layers between the target and detector, including the selectable filters, needs to be accurately calibrated.

* A software program that does accurate data reduction from the PIXE spectrum, correcting for the effects of detector efficiency, secondary fluorescence and matrix and filter absorption. The GeoPIXE software package (Ryan *et al.*, 1990) was purchased for this purpose.

To make quantitative analysis possible, the following factors need consideration:

* The analysis of standards of known composition as a test of the analytical accuracy of the proton microprobe results. Such tests included the analysis of pure element standards, primary steel and geological standards, as well as secondary geological standards. Interlaboratory comparisons were made with the Heavy Ion Analytical Facility (HIAF), in Sydney, Australia. Inter-technique comparisons were made using data obtained from X-ray Fluorescence Spectroscopy. It was found that the proton microprobe is accurate to within 5%.

* An assessment of the precision achievable under routine conditions. It was found that for analyses lasting approximately 6 to 8 minutes, the analytical precision is dependent on the counting statistics, which is, in turn, affected by the element of interest, filters that were used, the nature of the matrix, the concentration of the element in the sample and the counting time. Therefore, the percentage precision, although most typically less than 8%, can be much higher (up to about 30%). Experimental precision, which is independent of the counting statistics (resulting mainly from the stability of the hardware) is as low as 0.1 %.

* An assessment of the sensitivity of the microprobe under routine conditions. Typical detection limits for elements in the X-ray energy range of 7-16 keV (Zn to Zr) is between 1 and 5 ppm, but can be higher at lower and higher X-ray energies.

* Adequate thickness of geological polished thin sections is an important prerequisite for quantitative analysis. It was found that if geological sections are not thick enough, elements in the underlying glass slide are analyzed and added to the final PIXE spectrum, leading to erroneous results. Although corrections for these are possible, it is suggested that sections are cut thick enough (> 60 μm) to avoid this possible source of error altogether.

Once these factors have been established and evaluated, the proton microprobe allows the easy, relatively fast and accurate determination of the trace element compositions of minerals, with sufficient sensitivity and precision to detect subtle variations in the trace element content of natural mineral phases. The spot sizes for routine analyses are most commonly between 10-50 μm, for a beam current ranging between 5 and 15 nA. The analyses of the eclogitic minerals in this study have illustrated its use in geology, highlighting interesting features in the samples, e.g. clear trace element differences between minerals from kyanite-bearing and kyanite-free eclogite. The small size of the proton beam and the good analytical precision allowed the identification of trace element zoning profiles across garnets at the contact of the two eclogite types and have posed interesting geological questions for further study.

LIST OF REFERENCES

Anderson, H.H. and Ziegler, J.F. (1977): *Hydrogen Stopping Powers and Ranges.* Publ. Pergamon, New York, pp 317

Bajt, S. and Traxel, K. (1991): Micro-PIXE Measurements in Meteorites as a Source of New Information. *Nucl. Instr. and Meth.* **B54**, 317-324

Bevington, P.R. (1969): *Data Reduction and Error Analysis for the Physical Sciences.* Publ. McGraw-Hill, New York.

Blank, H., El Goresy, A., Janicke, J., Nobiling, R. and Traxel, K. (1984): Trace Element Determination in Lunar Rocks - Quantitative PIXE Analysis on Thick Samples. *Nucl. Instr. and Meth.* **B3**, 681-687

Cabri, L.J. (1988): Applications of Proton and Nuclear Microprobes in Ore Deposit Mineralogy and Metallurgy. *Nucl. Instr. and Meth.* **B30**, 459-465

Churms, C.L., Pilcher, J.V., Springhorn, K.A. and Tapper, U.A.S. (1993): A VAX and PC-based Data Acquisition System for MCA, Scanning and List-mode Analysis. *Nucl. Instr. and Meth.* **B77**, 56-61

Cookson, J.A., Ferguson, A.T.G. and Pilling, F.D. (1972): Proton Microbeams, Their Production and Use. *J. Radioanal. Chem.* **12**, 39-52

Cousens, D.R., Ryan, C.G., Sie, S.H. and Griffin, W.L. (1987): Self Absorption and Secondary Fluorescence Corrections of PIXE yields from Multilayered Targets. *Proc. 5th Australian Conf. Nucl. Techn. Anal.* 58-60

Currie, L.A. (1968): Limits for Qualitative Detection and Quantitative Determination, Application to Radiochemistry. *Anal. Chem.* **40**, 586-593

Folkmann, F., Gaarde, G., Huus, T. and Kemp, K (1974a): Proton Induced X-ray Emission as a Tool for Trace Element Analysis. *Nucl. Instr. and Meth.* **116**, 487-499

Folkmann, F., Borggreen, J. and Kjeldgaard, A. (1974b): Sensitivity in Trace Element Analysis by p, α and ^{16}O Induced X-rays. *Nucl. Instr. and Meth.* **119**, 117-123

Gould, C.R., Holzsweig, L.G., King, S.E., Lau, Y.C., Poore, R.V., Roberson, N.R. and Wender, S.A. (1981): The XSYS Data Acquisition System at Triangle Universities Nuclear Laboratory. *IEEE Trans. Nucl. Sci.* **NS-28**, 3708-3714

Gould, C.R. and Roberson, N.R. (1983): Vax 11/780 Data Acquisition System at Triangle Universities Nuclear Laboratory. *IEEE Trans. Nucl. Sci.* **NS-30**, 3758 - 3763

Govindaraju, K. (1984): Compilation of Working Values for 170 International Reference Samples of Mainly Silicate Rocks and Minerals. *Geostandards Newsletter*, **8**

Griffin, W.L., Cousens, D.R., Ryan, C.G., Sie, S.H. and Suter, G.F. (1989): Ni in Chrome Pyrope Garnets: A New Geothermometer. *Contrib. Mineral. Petrol.* **103**, 199-202

Griffin, W.L., Ryan, C.G., Cousens, D.R., Sie, S.H. and Suter, G.F. (1990): An Application of the Proton Microprobe to Diamond Exploration and Genesis. *Nucl. Instr. and Meth.* **B49**, 318-322

Grime, G.W., Dawson, M., Marsh, M., McArthur, I.C. and Watt, F. (1991): The Oxford Submicron Nuclear Microscopy Facility. *Nucl. Instr. and Meth.* **B54**, 52-63

Hatton, C.J. (1978): *The Geochemistry and Origin of Xenoliths from the Roberts Victor Mine.* Unpubl. Ph.D. Thesis, Univ. Cape Town, South Africa

Ishii, K. and Morita, S. (1984): Continuum X-rays Produced by Light Ion-Atom Collisions. *Phys. Rev.* **A30**, 2278-2286

Isozumi, Y. (1985): Uncertainties in the X^2 fit for Nuclear Radiation Spectra. *Nucl. Instr. and Meth.* **A235**, 164-173

Johansson, S.A.E. and Campbell, J.L. (1988): *PIXE. A Novel Technique for Elemental Analysis.* Publ. Wiley and Sons, pp 341

Johansson, S.A.E. (1991): Optimization of the Sensitivity in PIXE Analysis. *Intern. J. of PIXE.* **2**, 33-46

Johansson, T.B., Akselsson, K.R. and Johansson, S.A.E. (1970): X-ray Analysis: Elemental Trace Analysis at the 10^{-12} g Level. *Nucl. Instr. and Meth.* **84**, 141-143

Kirkley, M.B., Harte, B. and Gurney, J.J. (in press): Crustal Plagioclase-Rich Protoliths for Roberts Victor Kyanite Eclogites. Submitted to *Contrib. Mineral. Petrol.*

Lappin, M.A. and Dawson, J.B. (1975): Two Roberts Victor Cumulate Eclogites and their Re-equilibration. *Phys. Chem. Earth.* **9**, 351-365

Lappin, M.A. (1978): The Evolution of a Grospydite from the Roberts Victor Mine, South Africa. *Contrib. Mineral. Petrol.* **66**, 229-241

McCandless, T.E. and Gurney, J.J. (1989): Sodium in Garnet and Potassium in Clinopyroxene: Criteria for Classifying Mantle Eclogites. *Geol. Soc. Australia Spec. Publ.* **2**, 827-832

O'Reilly, S.Y., Griffin, W.L. and Ryan, C.G. (1991): Residence of Trace Elements in Metasomatized Spinel Lherzolite Xenoliths: A Proton Microprobe Study. *Contrib. Mineral. Petrol.* **109**, 98-113

Pilcher, J.V. and Wikner, V.C. (1991): The National Accelerator Centre Data Handling Network. *IEEE 7th Conf. Computer Appl. Nucl. Particle Plasma Phys., Conf. Record, IEEE, New York.* 317

Ryan, C.G., Clayton, E., Griffin, W.L., Sie, S.H. and Cousens, D.R. (1988): SNIP: A Statistics Sensitive Background Treatment for the Quantitative Analysis of PIXE Spectra in Geoscience Applications. *Nucl. Instr. and Meth.* **B34**, 396-402

Ryan, C.G., Cousens, D.R., Sie, S.H., Griffin, W.L., Suter, G.F. and Clayton, E. (1990): Quantitative PIXE Microanalysis of Geological Material using the CSIRO Proton Microprobe. *Nucl. Instr. and Meth.* **B47**, 55-71

Ryan, C.G. and Cousens, D.R. (1992): GeoPIXE: PIXE Microanalysis Software System User's Guide. *CSIRO Restricted Report*, pp 275

Ryan, C.G. and Jamieson, D.N. (1993): Dynamic Analysis: On-line Quantitative PIXE Micro-Analysis and its use in Overlap-Resolved Elemental Mapping. *Nucl. Instr. and Meth.* **B77**, 203-214

Ryan, C.G., Jamieson, D.N., Churms, C.L. and Pilcher, J.V. (1993): A New Method for True Quantitative Elemental Imaging using PIXE and the Proton Microprobe. *Proc. 8th Australian Conf. Nucl. Techn. Anal.* 178-180

Switzer, G. and Melson, W.G. (1969): Partially Melted Kyanite Eclogite from the Roberts Victor Mine, South Africa. *Smithsonian Contr. Earth Sci.* **1**, 1-9

Tapper, U.A.S. and Malmqvist, K.G. (1991): Analysis, Imaging and Modification of Microscopic Specimens with Accelerator Beams. *Anal. Chem.* **63**, 715-725

Tapper, U.A.S., McMurray, W.R., Ackermann, G.F., Churms, C.L., De Villiers, G., Fourie, D., Groenewald, P.J., Kritzinger, J., Pineda, C.A., Pilcher, J.V., Schmidt, H., Springhorn, K. and Swart, T. (1993): High Brightness Proton Beams at the NAC Nuclear Microprobe by Acceleration of H_2 Ions. *Nucl. Instr. and Meth.* **B77**, 17-24

Thiesen, R. and Vollath, D. (1967): *Tables of X-ray Mass Attenuation Coefficients.* Publ. Verlag Stahliessen M.B.H., Dusseldorf

Woldseth, R. (1973): *All you ever wanted to know about X-ray Energy Spectroscopy.* Publ. Kevex Corporation, California, pp 141

APPENDIX A

PLATES AND TABLE A1

APPENDIX A

PLATES AND TABLE A1

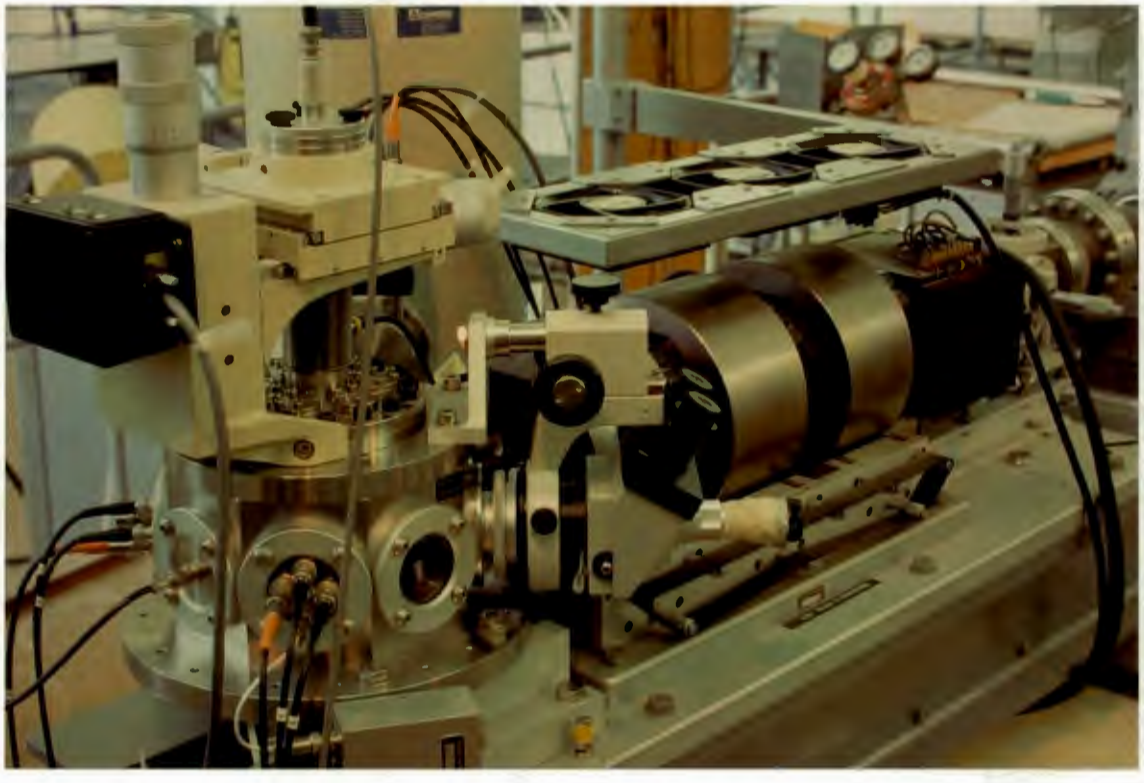

Plate 1: The National Accelerator Centre proton microprobe. To the left of the optical microscope (centre) is the sample chamber. Behind it the Si(Li) detector is visible. To the right of the microscope, two of the three circular focusing lenses can be seen. The rectangular box behind it is the scan amplifier.

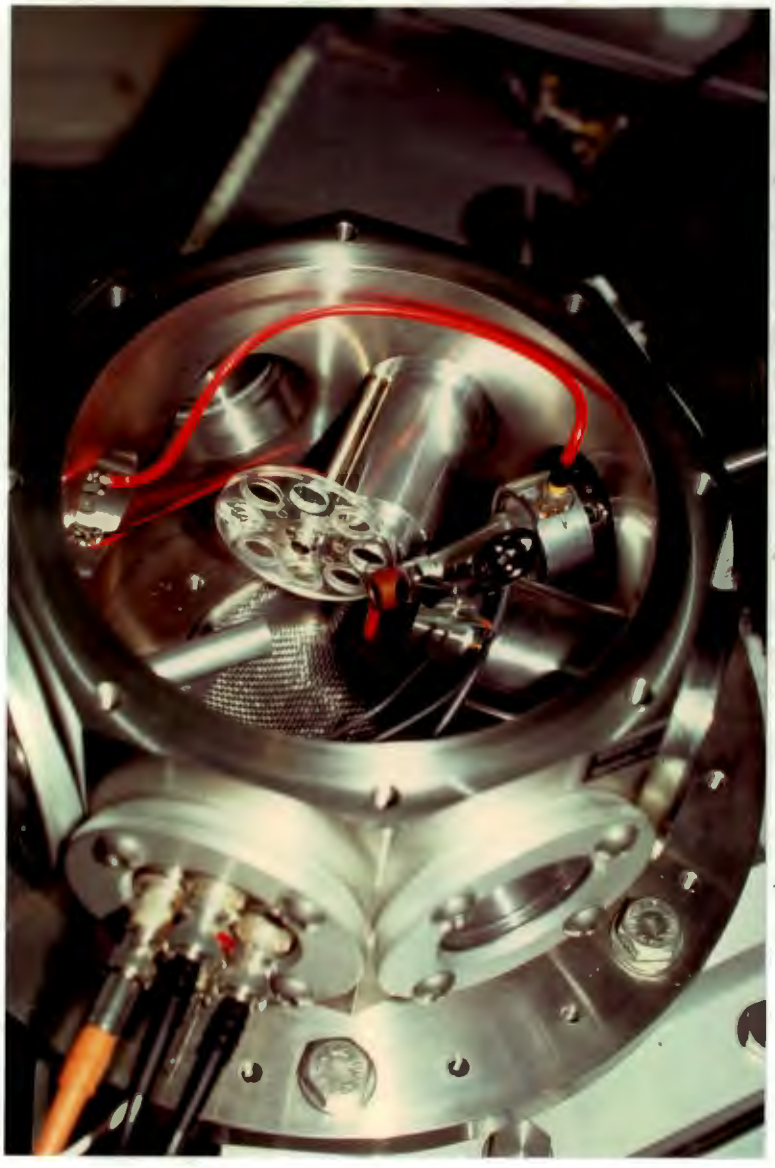

Plate 2: The proton microprobe sample chamber. The filter wheel is situated in front of the detector snout (the detector is not shown in this plate), to the left of the incoming beam position. Opposite the incoming beam, the faraday cup is visible, used for charge measurements during the analysis of thin targets.

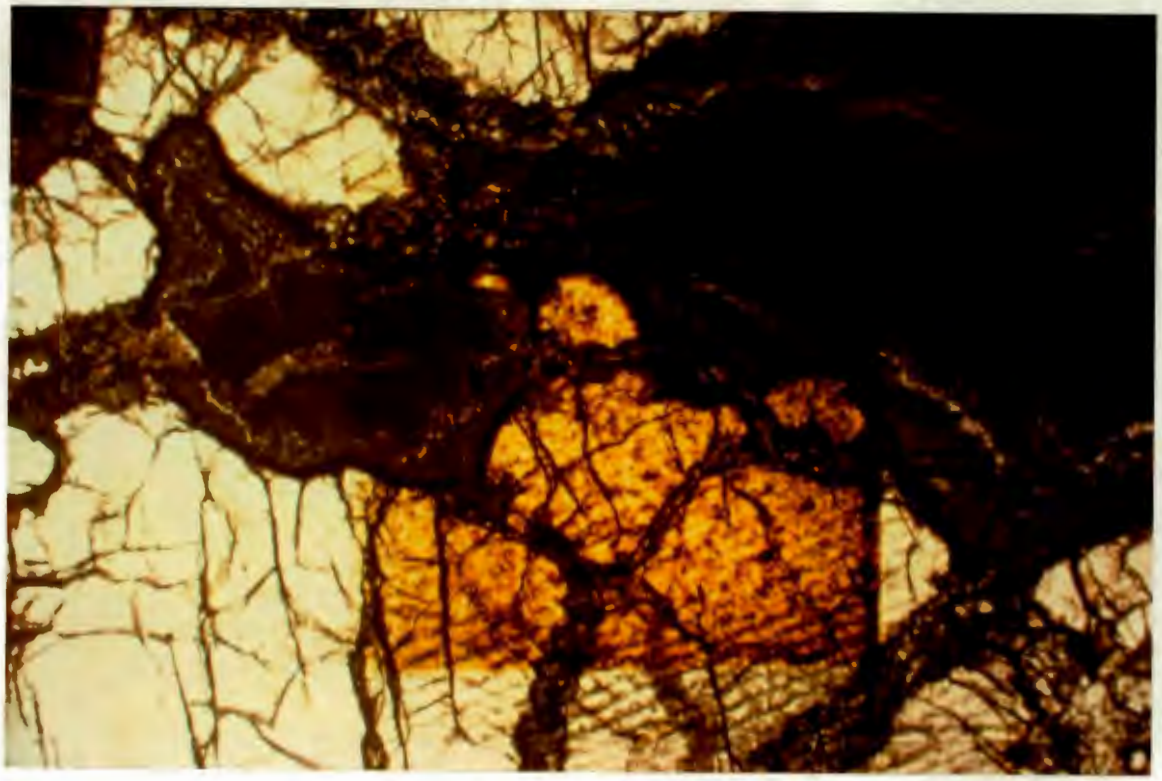

Plate 3: Elementally mapped area 1, in the kyanite zone of sample HRV 30. The map area (≈ 1.8 x 1.8 cm) is clearly visible by the discolouration of the carbon coating through interaction with the proton beam. The light mineral is the garnet and the dark mass is the altered clinopyroxene.

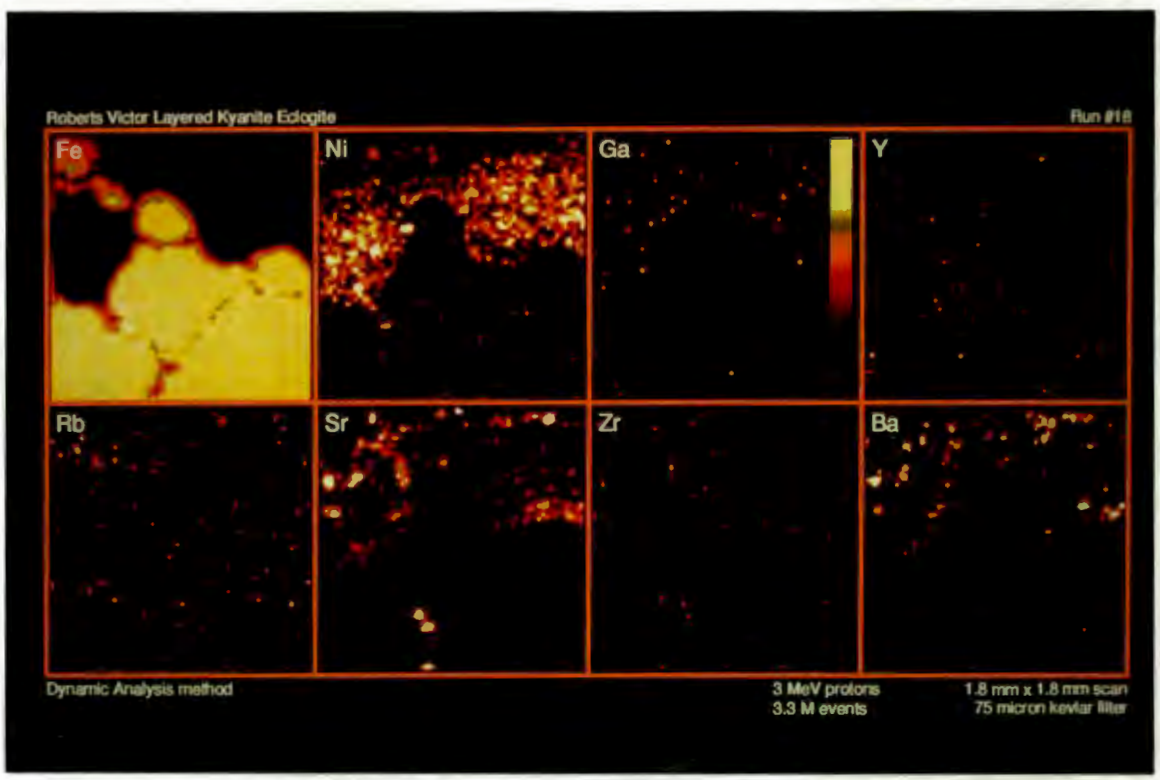

Plate 4: Elemental images of map area 1. The elements are indicated on each map, and the intensity of the colours is proportional to the concentration of the element in the sample. Note the heterogeneous distribution of Sr and Ba. The former occurs in the cracks in the garnet.

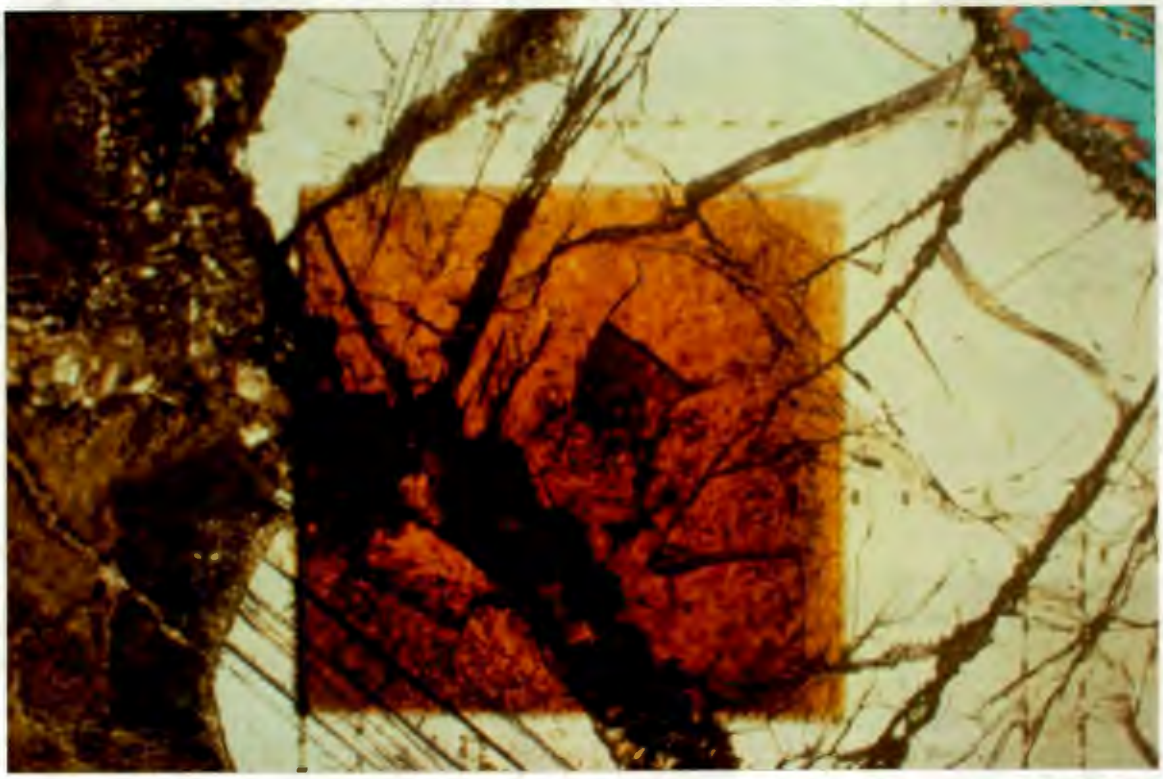

Plate 5: Elementally mapped area 2, in the kyanite zone of sample JJG 177. The map area, visible from the discolouration of the carbon coating, is ≈ 1.8 x 1.8 cm. The dark mineral is the altered clinopyroxene, occurring in a vein separating the garnet (right) from the kyanite (left).

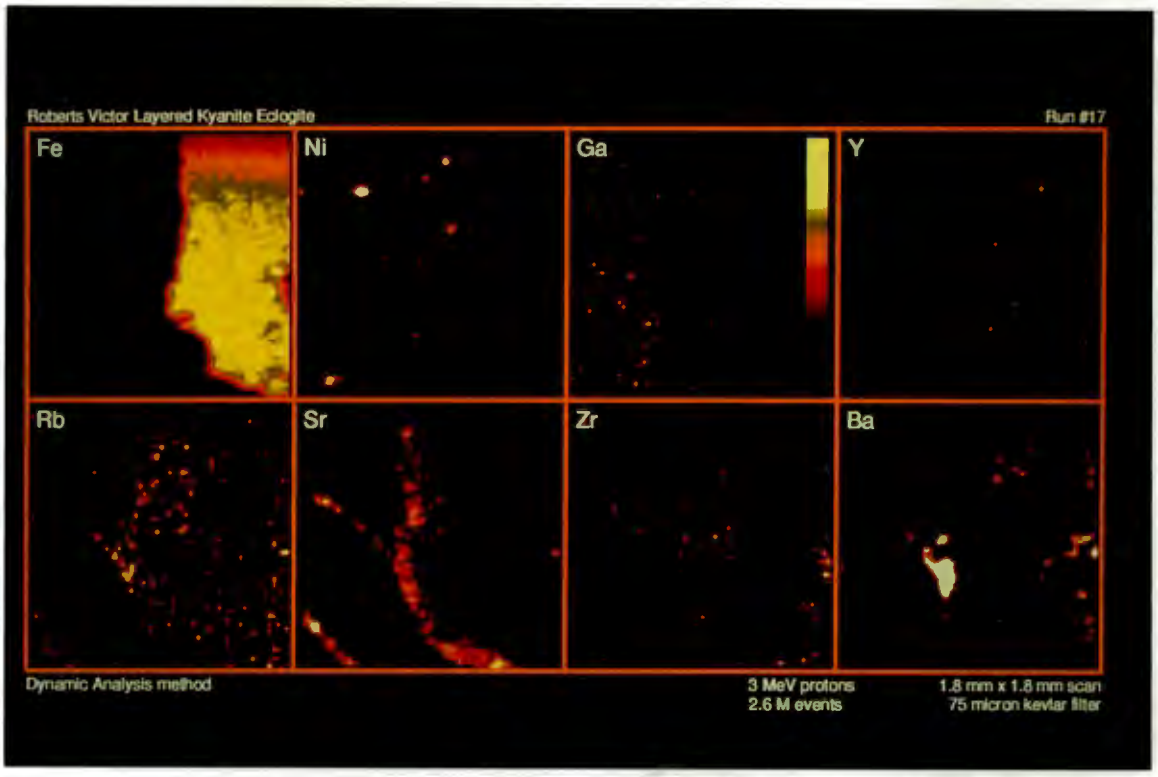

Plate 6: Elemental images of map area 2. Note the heterogeneous distribution of Sr, Rb and Ba. The former occurs along the boundaries of the altered clinopyroxene vein, and in a crack in the garnet. The "zoning" in the upper part of the Fe map is an artifact of the graphics software.

Table A1

Correspondence between the Siegbahn and IUPAC notation for X-ray lines.

Siegbahn	IUPAC	Siegbahn	IUPAC	Siegbahn	IUPAC
$K_{\alpha 1,2}$	$K\text{-}L_{2,3}$	$L_{\alpha 1}$	$L_3\text{-}M_5$	$M_{\alpha 1}$	$M_5\text{-}N_7$
$K_{\alpha 1}$	$K\text{-}L_3$	$L_{\alpha 2}$	$L_3\text{-}M_4$	$M_{\alpha 2}$	$M_5\text{-}N_6$
$K_{\alpha 2}$	$K\text{-}L_2$	$L_{\beta 1}$	$L_2\text{-}M_4$	M_{β}	$M_4\text{-}N_6$
$K_{\beta 1}$	$K\text{-}M_3$	$L_{\beta 2}$	$L_3\text{-}N_5$	M_{γ}	$M_3\text{-}N_5$
$K_{\beta 2}^{I}$	$K\text{-}N_3$	$L_{\beta 3}$	$L_1\text{-}M_3$	M_{ξ}	$M_{4,5}\text{-}N_{2,3}$
$K_{\beta 2}^{II}$	$K\text{-}N_2$	$L_{\beta 4}$	$L_1\text{-}M_2$		
$K_{\beta 3}$	$K\text{-}M_2$	$L_{\beta 5}$	$L_3\text{-}O_{4,5}$		
$K_{\beta 4}^{I}$	$K\text{-}N_5$	$L_{\beta 6}$	$L_3\text{-}N_1$		
$K_{\beta 4}^{II}$	$K\text{-}N_4$	$L_{\beta 7}$	$L_3\text{-}O_1$		
$K_{\beta 4x}$	$K\text{-}N_4$	$L_{\beta 7}'$	$L_3\text{-}N_{6,7}$		
$K_{\beta 5}^{I}$	$K\text{-}M_5$	$L_{\beta 9}$	$L_1\text{-}M_5$		
$K_{\beta 5}^{II}$	$K\text{-}M_4$	$L_{\beta 10}$	$L_1\text{-}M_4$		
		$L_{\beta 15}$	$L_3\text{-}N_4$		
		$L_{\beta 17}$	$L_2\text{-}M_3$		
		$L_{\gamma 1}$	$L_2\text{-}N_4$		
		$L_{\gamma 2}$	$L_1\text{-}N_2$		
		$L_{\gamma 3}$	$L_1\text{-}N_3$		
		$L_{\gamma 4}$	$L_1\text{-}O_3$		
		$L_{\gamma 4}'$	$L_1\text{-}O_2$		
		$L_{\gamma 5}$	$L_2\text{-}N_1$		
		$L_{\gamma 6}$	$L_2\text{-}O_4$		
		$L_{\gamma 8}$	$L_2\text{-}O_1$		
		$L_{\gamma 8}'$	$L_2\text{-}N_{6(7)}$		
		L_{η}	$L_2\text{-}M_1$		

APPENDIX B

THE ACCURACY OF THE PROTON MICROPROBE: TABLES B1-B10

APPENDIX B

THE ACCURACY THE NATIONAL ACCELERATOR CENTRE PROTON MICROPROBE

The accuracy of the PMP was tested by the analysis of targets of known composition such as steel-, and geological standards, as well as comparative analyses using the CSIRO PMP in Sydney, Australia, and using other techiques such as X-ray Fluorescence Spectroscopy (XRFS). The results of these tests are presented in Tables 1 to 10.

Standard targets of which the concentrations have been certified by a recognized authority are referred to in these tables as *primary standards*. Other standards, of which the concentrations where obtained by other techniques/PMP laboratories or are the manufacturer's given values are referred to as *secondary standards.*

All the microPIXE results are presented with 1σ uncertainty estimates.

Abbreviations

MDL	Minimum Detection Limit (99% confidence level)
ND	Not Detected
NA	Not Available

Index to Tables

Using the H^+ beam:

Using the H_2^+ beam:

Table B1

Proton Microprobe Analysis of the Primary Steel Standards D838, D840 and D841 and Comparison with the Certified Concentrations.

Element	Certified	NAC PMP[a]	MDL
(a) D838			
Cr	4.66	4.72 ± 0.05	0.006
Mn	0.20	0.20 ± 0.03	0.009
Co	4.90	5.04 ± 0.07	0.009
Cu	0.17	0.09 ± 0.01[b]	0.016
Mo	8.26	8.50 ± 0.25	0.026
W	1.70	1.63 ± 0.03	0.033
(b) D840			
Cr	2.12	2.14 ± 0.03	0.004
Mn	0.15	0.16 ± 0.01	0.005
Co	11.8	11.4 ± 0.05	0.006
Cu	0.06	0.02 ± 0.01[b]	0.010
Mo	0.07	0.05 ± 0.01	0.010
W	13.0	11.7 ± 0.2	0.022
(c) D841			
Cr	4.20	4.36 ± 0.05	0.004
Mn	0.27	0.30 ± 0.03	0.006
Cu	0.07	0.07 ± 0.01	0.008
Mo	0.84	0.84 ± 0.03	0.015
W	18.5	18.5 ± 0.2	0.022

(a) Results of the sum spectra of 6, 12 and 6 point analyses, to a total integrated charge of 0.06, 0.15 and 0.12 μC for samples D838, D840 and D841 respectively. The data were collected using a 2.5 MeV H^+ beam. The results are normalized to the given Fe concentrations(scaling factors = 1.01,1.02 and 1.00 respectively) and all values are reported as weight percent.

(b) The error in Cu results is attributed to the spectral overlap of the Cu K lines with Co K and W L lines.

Table B2

Proton Microprobe Analysis of the Primary Glass Standard BCR-1 and Comparison with the Certified Values (Govindaraju, 1984) and Analysis using the CSIRO Proton Microprobe (Ryan *et al.*, 1990).

Element	Certified	CSIRO PMP	NAC PMP[a]	MDL
Mn	1400	1460 ± 300	1358 ± 219	63
Fe	9.5%	9.6 ± 0.2%	9.5 %	22
Ni	13	13 ± 3	16.8 ± 5	8.5
Cu	18	15 ± 2	13.6 ± 2	6.3
Zn	125	124 ± 4	137 ± 8	4.6
Ga	22	23 ± 2	20.9 ± 1	3.9
Ge	1.5	NA	ND	3.3
Rb	47	43 ± 4	43 ± 2	3.9
Sr	330	343 ± 12	330 ± 8	4.4
Y	39	31 ± 4	31.6 ± 4	5.0
Zr	190	170 ± 12	183 ± 5	5.6
Nb	16	14 ± 5	12.7 ± 2	6.1
Ba	680	628 ± 90	652 ± 51	100
La	26	NA	183 ± 51[b]	110
Ce	53	NA	199 ± 50[b]	131
Pb	15	11 ± 4	16.0 ± 3	6.7

(a) Result of a sum spectrum from 6 spot analyses (total integrated charge Q = 6 μC), collected using a 3 MeV H^+ beam and normalized to the certified Fe concentration (scaling factor = 1.01). All values are reported as ppm unless otherwise indicated.

(b) The error in La and Ce concentrations is attributed to the low statistics of the peaks.

Table B3

Proton Microprobe Analysis of the Secondary Mineral Standards JJG 1424 (Garnet, Clinopyroxene and Orthopyroxene) and Comparison with Analyses by Electron Microprobe (EMP) and X-ray Fluorescence Spectroscopy (XRFS) (A. P. le Roex, unpubl. data).

Element	EMP	XRFS	NAC PMP[a]	MDL
(a) Garnet				
Cr	0.73 %	0.73 %	0.75 ± 0.02 %	81
Mn	0.23 %	0.26 %	0.28 ± 0.01 %	27
Fe	6.30 %	6.00 %	6.3 %	11
Ni		30	14.7 ± 2.3[b]	4.2
Cu		7	ND	2.5
Zn		7	8.0 ± 0.8	1.9
Y		23	22 ± 1.9	2.1
Zr		31	31 ± 1.5	2.5
(b) Clinopyroxene				
Cr	0.55 %	0.55 %	0.57 ± 0.1 %	55
Mn	0.05 %	0.04 %	0.04 ± 0.01 %	19
Fe	1.26 %	1.28 %	1.26 ± 0.2 %	8.6
Ni		281	227 ± 19[b]	4.0
Cu		8	6.5 ± 0.9	2.7
Zn		7	5.6 ± 0.6	2.0
Sr		323	322 ± 6.2	2.1
Y		5	ND	2.4
Zr		5	54 ± 3.9[c]	2.7
(c) Orthopyroxene				
Cr	0.15 %	0.13 %	0.13 ± 0.03 %	81
Mn	0.05 %	0.07 %	0.07 ± 0.01 %	28
Fe	3.92 %	3.71 %	3.92 ± 0.6 %	12
Ni		587	567 ± 48	5.0
Cu		10	ND	2.9
Zn		31	31 ± 2.1	2.2
Zr		3.5	ND	2.7

(a) Results of the sum spectra of 18 point analyses on each mineral to a total integrated charge of 38 μC in each case, collected using a 2.5 MeV H^+ beam and normalized to the electron microprobe Fe concentrations (A. P. le Roex, unpubl. data). All values are reported as ppm unless otherwise indicated.

(b) The error in the Ni results is attributed to spectral overlap with the major element Fe (explained fully in the text). Note the good agreement of the PMP Ni results with the XRFS Ni data for the orthopyroxene, resulting from a higher Ni concentration in the sample and the easier resolution of spectral overlap by the data analysis software.

(c) The large difference in comparative Zr concentrations is attributed to an error in the XRFS data, possibly a result of a bad XRF calibration for the element Zr in clinopyroxene. From the sum spectrum of the analyses, given in Figure B1 below, the presence of large amounts of Zr cannot be disputed, regardless of the accuracy of the calibration and the efficiency of the data analysis software.

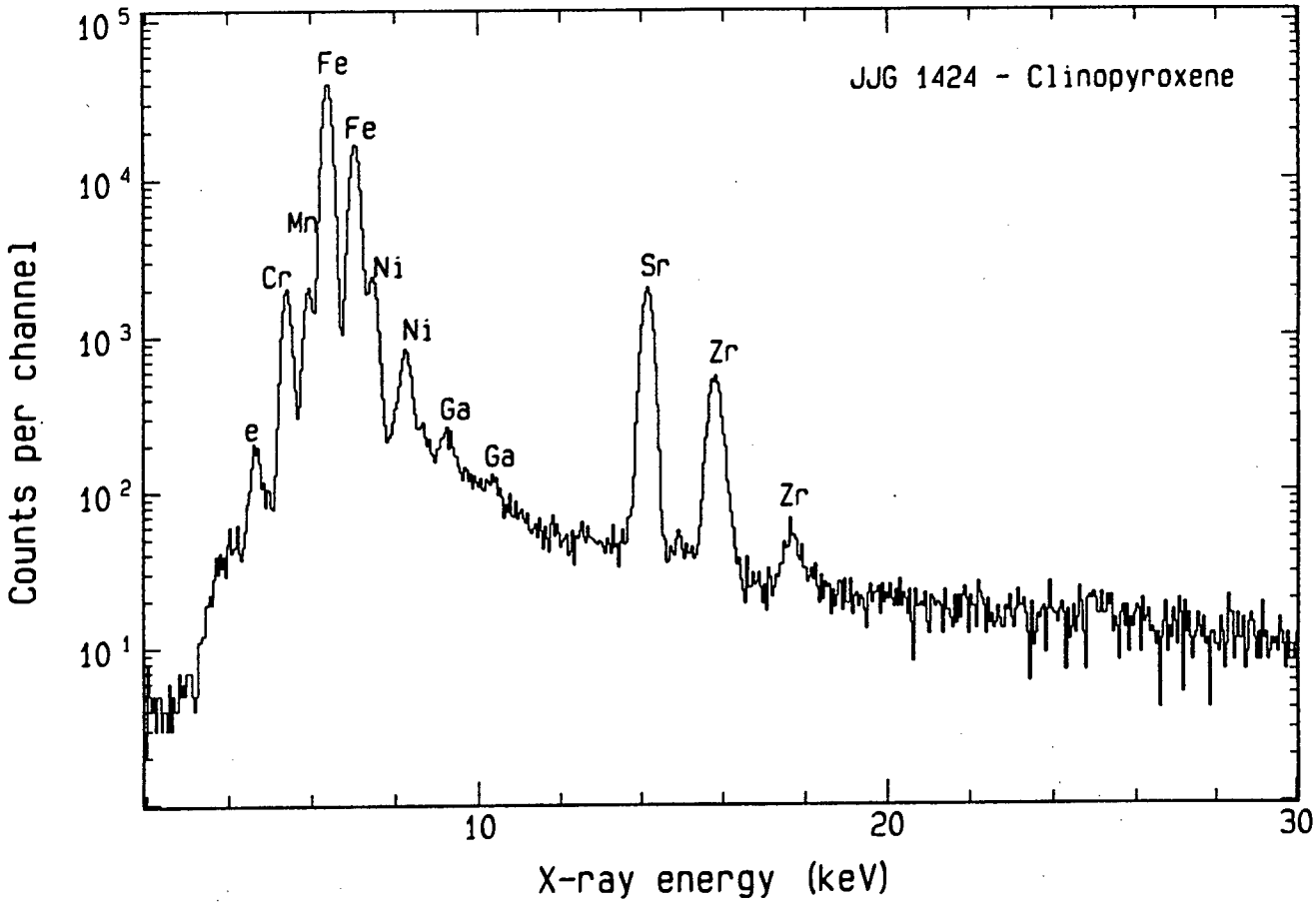

Figure B1: Sum Spectrum of 18point analyses on the clinopyroxene of JJG 1424. The presence of a relatively large concentration of Zr cannot be disputed. Please refer to section 5.2.2. (page 60), for a description of the method in which the data analyses software treats the spectral overlap of Sr K_{β} and Zr K_{α}.

Table B4

Proton Microprobe Analysis of the Secondary Mineral Standard H8 (Hornblende) and Comparison with the Analysis using the CSIRO Proton Microprobe (C. G. Ryan, unpubl. data).

Element	CSIRO PMP	NAC PMP[a]	MDL
Mn	0.51 %	0.62 ± 0.10 %	43
Fe	16.4 %	16.4 %	15
Zn	288 ± 21	279 ± 17	3.0
Ga	53 ± 3	53 ± 3	2.5
Ge	4.3 ± 0.6	6.3 ± 1	2.1
Sr	17 ± 1	17 ± 2	2.1
Y	162 ± 4	159 ± 6	2.3
Zr	30 ± 1	28 ± 2	2.5
Nb	25 ± 0.8	24 ± 2	2.7
W	48 ± 9	40 ± 10	8.5

(a) Results of the sum spectra of 12 point analyses to a total integrated charge of 19 μC, collected using a 3 MeV H^+ beam and normalized to the electron microprobe Fe concentrations (C. G. Ryan, unpubl. data). All values are reported as ppm unless otherwise indicated.

Table B5

Proton Microprobe Analysis of the Secondary Mineral Standard KSS (Kaersutite) and Comparison with the Analysis using the CSIRO Proton Microprobe (C. G. Ryan, unpubl. data).

Element	CSIRO PMP	NAC PMP[a]	MDL
Mn	0.248 %	0.317 ± 0.04%	40
Fe	13.21 %	13.21 %	14
Zn	71 ± 5	63 ± 4	2.6
Ga	13.7 ± 0.9	13.6 ± 0.9	2.2
Rb	4.3 ± 0.5	3.7 ± 1.2	2.1
Sr	812 ± 15	791 ± 15	2.3
Y	50 ± 1	55 ± 2	2.5
Zr	194 ± 3	200 ± 6	2.7
Nb	112 ± 2	121 ± 2	2.9
Ba	321 ± 22	396 ± 24	5.3

(a) Results of the sum spectra of 10 point analyses, to a total integrated charge of 20 μC, collected using a 3 MeV H^+ beam and normalized to the electron microprobe Fe concentrations (C. G. Ryan, unpubl. data). All values are reported as ppm unless otherwise indicated.

Table B6

Proton Microprobe Analysis of the Secondary Glass Standards SOV 115 and INT 152 and Comparison with the Manufacturer's given Concentrations.

Element	Given	NAC PMP[a]	MDL
(a) SOV 115			
K	4.32 %	4.31 ± 0.9 %[b]	396
Ca	6.66 %	6.66 %	62
Fe	126	123 ± 5	1.1
As	1325	1299 ± 18	0.9
Sb	2463	2880 ± 77	24
Ba	1.81 %	1.79 ± 0.05 %	82
(b) INT 152			
K	4316	4263 ± 933[b]	334
Ca	7.50 %	7.50 %	46
Ti	432	411 ± 40	6.4
Cr	27	22 ± 1	2.0
Fe	1258	1211 ± 40	1.0
Zr	133	268 ± 8	2.1
Ba	672	616 ± 64	29
Pb	742	547 ± 8	1.9

(a) Results of the sum spectra of 8 point analyses on each sample (total integrated charge for each Q = 24 μC), collected using a 3 MeV H^+ beam and normalized to the given Ca concentrations. All values are reported as ppm unless otherwise indicated.

(b) The low precision in the K results is attributed to the uncertainty that arises from X-ray attenuation in the Al filter.

Table B7

Proton Microprobe Analysis of the Primary Glass Standard BCR-1 and Comparison with the Certified Values (Govindaraju, 1984) and Analysis using the CSIRO Proton Microprobe (Ryan *et al.*, 1990).

Element	Certified	CSIRO PMP	NAC PMP[a]	MDL
Mn	1400	1460 ± 300	1520 ± 243	33
Fe	9.5%	9.6 ± 0.2%	9.5 %	14
Ni	13	13 ± 3	ND	5.8
Cu	18	15 ± 2	11 ± 1	3.8
Zn	125	124 ± 4	145 ± 8	3.0
Ga	22	23 ± 2	21.3 ± 1	2.5
Ge	1.5	NA	ND	2.2
Rb	47	43 ± 4	44 ± 2	2.9
Sr	330	343 ± 12	345 ± 6	3.4
Y	39	31 ± 4	28 ± 2	4.0
Zr	190	170 ± 12	198 ± 4	4.9
Nb	16	14 ± 5	12.3 ± 2	5.8
Ba	680	628 ± 90	720 ± 50	110
Pb	15	11 ± 4	12.3 ± 2	4.3

(a) Result of a sum spectrum from 17 spot analyses (total integrated charge Q = 34 μC), collected using a 2 MeV H_2^+ beam and normalized to the certified Fe concentration (scaling factor = 1.35). All values are reported as ppm unless otherwise indicated.

Table B8

Proton Microprobe Analysis of the Secondary Mineral Standard H8 (Hornblende) and Comparison with the Analysis using the CSIRO Proton Microprobe (C. G. Ryan, unpubl. data).

Element	CSIRO PMP	NAC PMP[a]	MDL
Mn	0.51 %	0.40 ± 0.06 %	22
Fe	16.4 %	16.4 %	10
Zn	288 ± 21	274 ± 15	1.3
Ga	53 ± 3	47 ± 3	1.2
Ge	4.3 ± 0.6	2.7 ± 1	1.0
Sr	17 ± 1	14.3 ± 2	1.2
Y	162 ± 4	164 ± 3	1.2
Zr	30 ± 1	30 ± 1	1.4
Nb	25 ± 0.8	28 ± 1	1.6
W	48 ± 9	50 ± 4	3.5

(a) Results of the sum spectra of 28 point analyses to a total integrated charge of 260 μC, collected using a 2 MeV H_2^+ beam and normalized to the electron microprobe Fe concentrations (C. G. Ryan, unpubl. data). All values are reported as ppm unless otherwise indicated.

Table B9

Proton Microprobe Analysis of the Secondary Mineral Standard KSS (Kaersutite) and Comparison with the Analysis using the CSIRO Proton Microprobe (C. G. Ryan, unpubl. data).

Element	CSIRO PMP	NAC PMP[a]	MDL
Mn	0.248 %	0.219 ± 0.04%	32
Fe	13.21 %	13.21 %	13
Zn	71 ± 5	67 ± 4	2.6
Ga	13.7 ± 0.9	14.0 ± 0.9	2.3
Rb	4.3 ± 0.5	ND	2.6
Sr	812 ± 15	804 ± 15	3.0
Y	50 ± 1	48 ± 2	3.5
Zr	194 ± 3	200 ± 4	3.9
Nb	112 ± 2	120 ± 3	4.2
Ba	321 ± 22	378 ± 34	93

(a) Results of the sum spectra of 21 point analyses, to a total integrated charge of 42 μC, collected using a 2 MeV H_2^+ beam and normalized to the electron microprobe Fe concentrations (C. G. Ryan, unpubl. data). All values are reported as ppm unless otherwise indicated.

Table B10

Proton Microprobe Analysis of the Secondary Glass Standards SOV 115 and INT 152 and Comparison with the Manufacturer's given Concentrations.

Element	Given	NAC PMP[a]	MDL
(a) SOV 115			
K	4.32 %	4.34 ± 0.9 %	765
Ca	6.66 %	6.66 %	135
Fe	126	127 ± 5	3.3
As	1325	1358 ± 24	2.9
Sb	2463	2873 ± 136	134
Ba	1.81 %	1.85 ± 0.08 %	532
(b) INT 152			
K	4316	4599 ± 1000[b]	581
Ca	7.50 %	7.50 %	87
Ti	432	393 ± 38	13
Cr	27	15 ± 5	4.7
Fe	1258	1251 ± 42	2.6
Zr	133	300 ± 12	10
Ba	672	852 ± 160	256
Pb	742	577 ± 12	5.3

(a) Results of the sum spectra of 10 point analyses on each sample (total integrated charge for each Q = 5 μC), collected using a 2 MeV H_2^+ beam and normalized to the given Ca concentrations. All values are reported as ppm unless otherwise indicated.

(b) The low precision in the K results is attributed to the uncertainty that arises from X-ray attenuation in the Al filter.

APPENDIX C

APPLICATION OF THE PROTON MICROPROBE - ANALYTICAL RESULTS (TABLES C1-C6)

APPENDIX C

APPLICATION OF THE PROTON MICROPROBE - ANALYTICAL RESULTS

The trace element compositions of the Roberts Victor eclogites and kyanite eclogites that were analyzed in this study are listed. The results are presented with a 1σ error bar, and unless indicated as wt%, all data are given as ppm. All spectra were collected using a proton beam of 3.0 MeV and a secondary electron suppression voltage of - 1 kV. In the case of the garnets and clinopyroxenes, a 160 μm Al filter was used to attenuate the Fe X-rays. A 40 μm Al filter was used during the analyses of the kyanite grains. The beam currents varied between 5 and 15 nA, and the beam spot size between 10 to 100 μm.

Results donated with an asterisk (*) at the Fe numbers, were normalized to the electron microprobe Fe numbers, as was discussed in Chapter 5. Scaling factors remained very close to one (generally between 0.97 and 1.02).

Mineral Abbreviations

ACpx	Altered Clinopyroxene
Cpx	Clinopyroxene
Gar	Garnet
Ky	Kyanite

Other Abbreviations

An. #	GeoPIXE datafile number
n	Number of analyses
NA	Not analyzed (i.e. not included in fit to raw spectrum)
ND	Not detected

Index to Tables

Table C1

Sample HRV 17

Sample	HRV 17-B	HRV 17-B	HRV 17-B	HRV 17-B	HRV 17-B
Mineral	Gar	Gar	Gar	Gar	Gar
An. #	36	35	38	39	40
Cr	680 ± 123	434 ± 121	581 ± 122	606 ± 123	482 ± 156
Mn	2960 ± 63	3030 ± 69	3100 ± 86	2950 ± 63	3060 ± 63
Fe	11 ± .03%	11 ± .03%	11 ± .02%	11 ± .03%	11 ± .02%
Zn	70 ± 2.0	71 ± 3.0	67 ± 2.6	70 ± 2.2	70 ± 2.0
Ga	5.9 ± 1.1	9.2 ± 1.3	6.3 ± 1.1	8.0 ± 1.3	5.0 ± 1.1
Sr	4.5 ± 1.3	< 3.7	< 3.8	< 3.7	< 3.8
Y	17 ± 1.4	19 ± 1.9	18 ± 1.4	19 ± 2.2	20 ± 1.5
Zr	27 ± 1.8	26 ± 2.9	27 ± 2.2	20 ± 1.7	36 ± 2.0

Sample	HRV 17-B	HRV 17-B	HRV 17-B	HRV 17-B	HRV 17-B
Mineral	Gar	Gar	Gar	Gar	Gar
An. #	41	42	43	46	47
Cr	865 ± 147	500 ± 121	594 ± 151	< 303	436 ± 171
Mn	2830 ± 62	2920 ± 67	2980 ± 63	3080 ± 94	3360 ± 65
Fe	11 ± .03%	11 ± .04%	11 ± .03%	11 ± .04%	11 ± .03%
Zn	73 ± 2.7	69 ± 3.4	72 ± 2.5	71 ± 2.1	68 ± 2.0
Ga	5.7 ± 1.1	5.5 ± 1.1	8.0 ± 1.3	6.4 ± 1.2	6.4 ± 1.1
Sr	< 3.6	< 3.7	4.5 ± 1.3	< 3.6	< 3.7
Y	23 ± 2.6	19 ± 2.5	21 ± 1.9	20 ± 2.2	17 ± 1.7
Zr	30 ± 1.9	23 ± 1.7	25 ± 2.1	32 ± 2.0	29 ± 2.1

Table C1 (continued)

Sample	HRV 17-B	HRV 17-B	HRV 17-B	HRV 17-B	HRV 17-B
Mineral	Gar	Gar	Gar	Gar	Gar
An. #	49	50	58	59	60
Cr	524 ± 140	847 ± 127	537 ± 125	381 ± 123	347 ± 119
Mn	3410 ± 66	3340 ± 96	3270 ± 92	3140 ± 98	2650 ± 61
Fe	11 ± .03%	11 ± .04%	11 ± .03%	11 ± .04%	10 ± .02%
Zn	67 ± 2.4	69 ± 2.0	70 ± 2.3	70 ± 2.2	74 ± 2.2
Ga	9.5 ± 1.2	6.8 ± 1.1	8.6 ± 1.1	7.0 ± 2.2	7.5 ± 1.5
Sr	< 3.6	< 3.8	< 3.8	< 3.7	< 3.7
Y	22 ± 1.5	19 ± 1.9	21 ± 1.5	18 ± 1.4	20 ± 1.5
Zr	28 ± 1.8	22 ± 1.8	27 ± 1.8	28 ± 1.9	33 ± 2.0

Sample	HRV 17-B	HRV 17-B	HRV 17-B	HRV 17-B	HRV 17-B
Mineral	Gar	Gar	Gar	Gar	Gar
An. #	61	68	69	70	71
Cr	536 ± 135	389 ± 119	< 347	< 288	< 272
Mn	2150 ± 62	1690 ± 57	1400 ± 80	1440 ± 67	444 ± 146
Fe	8.9 ± .03%	9.1 ± .02%	8.7 ± .04%	8.5 ± .04%	8.2 ± .01%
Zn	61 ± 2.1	71 ± 2.0	66 ± 2.8	72 ± 3.1	67 ± 2.4
Ga	14 ± 1.5	6.4 ± 1.1	11 ± 1.6	13 ± 1.2	13 ± 1.2
Sr	15 ± 1.5	5.0 ± 1.2	< 3.6	7.6 ± 1.5	8.8 ± 1.3
Y	16 ± 1.4	17 ± 1.5	14 ± 2.0	13 ± 2.0	15 ± 1.3
Zr	29 ± 2.4	35 ± 2.0	41 ± 2.1	31 ± 2.0	37 ± 2.0

Table C1 (continued)

Sample	HRV 17-B	HRV 17-B	HRV 17-B	HRV 17-B	HRV 17-B
Mineral	Gar	Gar	Gar	Gar	Gar
An. #	72	73	74	76	77
Cr	292 ± 118	< 287	536 ± 124	389 ± 122	406 ± 141
Mn	1320 ± 67	1420 ± 56	3060 ± 81	1640 ± 55	1660 ± 62
Fe	8.6 ± .05%	8.4 ± .03%	11 ± .01%	8.7 ± .02%	8.5 ± .01%
Zn	65 ± 2.0	60 ± 2.7	70 ± 2.0	71 ± 2.0	68 ± 2.3
Ga	11 ± 1.2	11 ± 1.2	8.9 ± 1.1	13 ± 1.2	12 ± 1.2
Sr	5.9 ± 1.2	7.1 ± 1.3	< 3.8	4.3 ± 1.3	5.7 ± 1.9
Y	12 ± 1.5	11 ± 1.4	17 ± 1.4	9.8 ± 2.5	11 ± 1.4
Zr	29 ± 2.2	33 ± 2.5	26 ± 1.8	28 ± 2.5	33 ± 3.0

Sample	HRV 17-B	HRV 17-B	HRV 17-B	HRV 17-B	HRV 17-B
Mineral	Gar	Gar	Gar	Gar	Gar
An. #	78	79	80	81	82
Cr	772 ± 175	1040 ± 100	755 ± 122	< 304	565 ± 146
Mn	1590 ± 78	2950 ± 92	1670 ± 62	1570 ± 68	1500 ± 54
Fe	8.5 ± .01%	11 ± .03%	8.7 ± .03%	8.5 ± .02%	8.5 ± .02%
Zn	64 ± 2.0	72 ± 2.1	65 ± 3.0	70 ± 2.0	72 ± 2.2
Ga	12 ± 1.2	5.7 ± 1.0	7.4 ± 1.2	9.4 ± 1.3	13 ± 1.2
Sr	4.8 ± 1.3	< 3.7	5.4 ± 1.7	7.5 ± 1.3	5.3 ± 1.9
Y	13 ± 1.3	16 ± 1.5	10 ± 2.0	13 ± 1.4	11 ± 1.8
Zr	34 ± 2.7	31 ± 2.5	38 ± 2.8	37 ± 2.4	34 ± 1.9

Table C1 (continued)

Sample	HRV 17-B	HRV 17-B	HRV 17-B	HRV 17-B	HRV 17-B
Mineral	Gar	Gar	Cpx	Cpx	Cpx
An. #	83	84	48	51	52
Cr	489 ± 146	592 ± 119	524 ± 102	474 ± 95	571 ± 77
Mn	1610 ± 73	1480 ± 54	441 ± 53	517 ± 33	502 ± 33
Fe	8.7 ± .02%	8.2 ± .02%	3.0 ± .01%	2.8 ± .01%	2.7 ± .01%
Zn	68 ± 2.7	67 ± 2.8	48 ± 2.2	47 ± 2.8	43 ± 1.7
Ga	11 ± 1.3	12 ± 1.2	17 ± 1.5	19 ± 1.2	21 ± 1.3
Sr	5.7 ± 1.3	5.9 ± 1.3	216 ± 3.8	192 ± 4.3	203 ± 3.9
Y	14 ± 1.3	11 ± 1.3	NA	NA	NA
Zr	32 ± 1.9	32 ± 1.9	24 ± 2.7	25 ± 2.6	32 ± 2.7
Ba	NA	NA	192 ± 45	< 141	< 136

Sample	HRV 17-B	HRV 17-B	HRV 17-B	HRV 17-B	HRV 17-B
Mineral	ACpx	ACpx	ACpx	ACpx	ACpx
An. #	89	90	92	93	94
Cr	216 ± 137	251 ± 66	177 ± 83	262 ± 148	< 222
Mn	268 ± 56	306 ± 43	287 ± 31	522 ± 68	886 ± 58
Fe	1.6 ± .01%	1.5 ± .01%	1.6 ± .01%	1.9 ± .01%	3.9 ± .02%
Zn	48 ± 2.0	45 ± 2.2	53 ± 1.7	39 ± 1.6	35 ± 1.5
Ga	24 ± 1.5	25 ± 1.3	26 ± 1.3	19 ± 1.2	18 ± 1.2
Sr	326 ± 4.6	268 ± 4.2	238 ± 5.0	543 ± 7.5	542 ± 5.8
Zr	19 ± 2.8	15 ± 2.5	16 ± 3.2	31 ± 4.6	86 ± 5.8
Ba	1.7 ± .05%	1.4 ± .03%	.96 ± .02%	2.5 ± .05%	.26 ± .01%

Table C1 (continued)

Sample	HRV 17-B	HRV 17-B	HRV 17-B	HRV 17-B	HRV 17-B
Mineral	ACpx	ACpx	ACpx	ACpx	Cpx
An. #	95	96	97	98	99
Cr	749 ± 184	368 ± 73	506 ± 91	467 ± 92	576 ± 77
Mn	1620 ± 100	450 ± 29	717 ± 33	505 ± 40	425 ± 30
Fe	7.9 ± .02%	2.5 ± .01%	2.7 ± .01%	2.5 ± .01%	2.6 ± .01%
Zn	72 ± 2.0	54 ± 2.1	49 ± 1.9	47 ± 1.7	40 ± 1.8
Ga	8.3 ± 1.3	15 ± 1.4	17 ± 1.2	18 ± 1.5	17 ± 1.1
Sr	199 ± 3.8	218 ± 3.8	291 ± 6.7	263 ± 4.2	174 ± 3.4
Zr	55 ± 3.1	22 ± 3.8	29 ± 2.8	31 ± 2.8	22 ± 2.6
Ba	409 ± 48	366 ± 55	.24 ± .01%	1.2 ± .02%	< 123

Sample	HRV 17-B	HRV 17-B	HRV 17-B	HRV 17-B	HRV 17-B
Mineral	ACpx	ACpx	Cpx	Cpx	ACpx
An. #	100	101	102	103	104
Cr	359 ± 94	282 ± 76	384 ± 83	524 ± 77	509 ± 82
Mn	566 ± 40	594 ± 32	421 ± 29	400 ± 30	500 ± 44
Fe	2.7 ± .01%	2.6 ± .01%	2.6 ± .01%	2.7 ± .01%	3.0 ± .01%
Zn	57 ± 1.8	46 ± 1.7	42 ± 2.5	45 ± 2.7	46 ± 1.8
Ga	11 ± 1.1	18 ± 1.2	19 ± 1.2	19 ± 1.3	17 ± 1.2
Sr	340 ± 4.6	244 ± 4.0	180 ± 3.5	203 ± 4.3	299 ± 6.4
Zr	39 ± 4.3	27 ± 2.7	26 ± 3.5	23 ± 2.5	26 ± 2.8
Ba	.93 ± .03%	.89 ± .03%	< 127	< 123	.63 ± .02%

Table C1 (continued)

Sample	HRV 17-B	HRV 17-B	HRV 17-B	HRV 17-B	HRV 17-B
Mineral	Ky	Ky	Ky	Ky	Ky
An. #	62	64	65	66	75
Ti	576 ± 18	607 ± 21	591 ± 21	533 ± 16	604 ± 20
Cr	320 ± 4.5	332 ± 4.7	337 ± 5.4	311 ± 6.8	314 ± 2.9
Fe	1750 ± 5.0	1850 ± 5.7	1940 ± 6.4	1610 ± 21	2060 ± 5.5
Ga	36 ± 0.9	38 ± 0.9	36 ± 1.0	36 ± 1.3	36 ± 1.3

Sample	HRV 17-B	HRV 17-C	HRV 17-C	HRV 17-C	HRV 17-C
Mineral	Ky	Gar	Gar	Gar	Gar
An. #	88	3	4	7	9
Ti	601 ± 25	NA	NA	NA	NA
Cr	334 ± 3.4	< 297	677 ± 133	776 ± 137	464 ± 135
Mn	-	1120 ± 56	1360 ± 63	1550 ± 66	1480 ± 85
Fe	1760 ± 8.6	6.3 ± .04%	7.7 ± .02%	8.0 ± .03%	8.3 ± .04%
Zn	-	44 ± 2.7	56 ± 2.2	57 ± 2.2	62 ± 2.6
Ga	37 ± 1.0	8.8 ± 1.2	14 ± 1.4	12 ± 1.3	15 ± 1.6
Sr	-	59 ± 2.6	31 ± 2.4	25 ± 2.0	11 ± 1.7
Y	-	8.4 ± 1.5	9.5 ± 2.0	14 ± 1.8	9.6 ± 1.9
Zr	-	34 ± 2.6	27 ± 2.3	29 ± 3.3	22 ± 2.8

Table C1 (continued)

Sample	HRV 17-C	HRV 17-C	HRV 17-C	HRV 17-C	HRV 17-C
Mineral	Gar	Gar	Gar	Gar	Gar
An. #	15	18	19	20	21
Cr	1250 ± 210	514 ± 165	487 ± 169	571 ± 143	735 ± 151
Mn	1860 ± 111	1450 ± 80	1220 ± 79	1570 ± 122	1580 ± 75
Fe	9.5 ± .02%	8.3 ± .02%	6.9 ± .04%	8.66 ±.04%	9.1 ± .03%
Zn	77 ± 2.5	62 ± 2.2	57 ± 2.6	68 ± 2.3	70 ± 2.6
Ga	13 ± 1.7	13 ± 1.4	10 ± 1.3	15 ± 1.4	16 ± 1.6
Sr	< 4.4	17 ± 1.8	48 ± 2.4	22 ± 2.0	4.9 ± 1.6
Y	12 ± 1.6	8.9 ± 2.0	11 ± 1.5	7.8 ± 2.2	15 ± 1.5
Zr	44 ± 2.9	21 ± 2.1	40 ± 2.8	35 ± 2.8	34 ± 2.7

Sample	HRV 17-C	HRV 17-C	HRV 17-C	HRV 17-C	HRV 17-C
Mineral	Gar	Gar	Gar	Gar	Gar
An. #	22	23	24	25	27
Cr	1150 ± 155	2100 ± 290	952 ± 187	1200 ± 161	1100 ± 181
Mn	1540 ± 72	4160 ± 152	3350 ± 119	3590 ± 123	3470 ± 88
Fe	9.2 ± .03%	13 ± .07%	12 ± .05%	12 ± .05%	12 ± .05%
Zn	71 ± 2.5	74 ± 2.4	67 ± 2.3	66 ± 3.1	65 ± 2.4
Ga	15 ± 1.8	8.7 ± 1.3	6.9 ± 1.8	8.0 ± 2.5	9.4 ± 1.3
Sr	5.3 ± 1.5	< 4.1	11 ± 2.6	13 ± 1.7	13 ± 1.7
Y	15 ± 1.5	24 ± 2.0	19 ± 1.6	22 ± 2.2	23 ± 1.7
Zr	41 ± 2.4	29 ± 2.2	31 ± 2.6	34 ± 2.3	29 ± 2.4

Table C1 (continued)

Sample	HRV 17-C	HRV 17-C	HRV 17-C	HRV 17-C	HRV 17-D
Mineral	Gar	Gar	Gar	Ky	Ky
An. #	28	29	30	26	1
Ca	NA	NA	NA	137 ± 44	< 67
Ti	NA	NA	NA	542 ± 7.6	697 ± 25
V	NA	NA	NA	73 ± 3.6	166 ± 17
Cr	409 ± 204	< 290	400 ± 196	311 ± 2.9	343 ± 12
Mn	3330 ± 104	1370 ± 82	1490 ± 59	NA	NA
Fe	11 ± .07%	7.5 ± .03%	7.9 ± .03%	1060 ± 5.3	1130 ± 22
Zn	66 ± 2.3	55 ± 2.1	56 ± 2.4	NA	NA
Ga	8.0 ± 1.2	7.3 ± 1.2	8.7 ± 1.5	35 ± 0.8	38 ± 1.0
Sr	17 ± 2.9	43 ± 3.9	39 ± 2.2	NA	NA
Y	17 ± 2.2	11 ± 1.6	13 ± 1.5	NA	NA
Zr	31 ± 3.1	47 ± 3.3	41 ± 3.2	NA	NA

Sample	HRV 17-D	HRV 17-D	HRV 17-D	HRV 17-D	HRV 17-D
Mineral	Ky	Ky	Ky	Ky	Ky
An. #	2	3	4	5	6
Ca	< 60	< 66	450 ± 116	< 69	669 ± 147
Ti	676 ± 25	721 ± 23	755 ± 32	693 ± 23	766 ± 28
V	150 ± 14	165 ± 17	152 ± 16	165 ± 18	154 ± 16
Cr	322 ± 11	356 ± 12	327 ± 7.6	351 ± 14	367 ± 11
Fe	1430 ± 13	1130 ± 22	1370 ± 12	1120 ± 21	1110 ± 22
Ga	38 ± 0.9	37 ± 1.3	37 ± 0.9	37 ± 0.8	38 ± 1.3

Table C1 (continued)

Sample	HRV 17-D	HRV 17-D	HRV 17-D	HRV 17-D	HRV 17-D
Mineral	Ky	Ky	Ky	Ky	Ky
An. #	7	8	9	10	11
Ca	< 58	444 ± 138	< 59	< 63	< 69
Ti	668 ± 23	667 ± 29	650 ± 24	650 ± 21	733 ± 25
V	143 ± 11	130 ± 10	147 ± 13	141 ± 11	163 ± 20
Cr	329 ± 13	329 ± 7.7	331 ± 11	334 ± 9.0	369 ± 10
Fe	1520 ± 13	1150 ± 12	1350 ± 11	1340 ± 11	1180 ± 19
Ga	36 ± 0.8	40 ± 0.8	36 ± 0.8	35 ± 0.8	38 ± 1.1

Sample	HRV 17-D	HRV 17-D	HRV 17-D	HRV 17-D	HRV 17-D
Mineral	Ky	Ky	Ky	Ky	Ky
An. #	12	13	14	15	16
Ca	< 62	< 60	< 62	< 64	< 58
Ti	653 ± 20	654 ± 23	690 ± 24	687 ± 26	678 ± 26
V	143 ± 9.9	147 ± 12	142 ± 13	137 ± 12	143 ± 12
Cr	342 ± 11	340 ± 11	336 ± 11	335 ± 9.3	334 ± 8.7
Fe	1410 ± 13	1170 ± 11	1570 ± 13	1650 ± 9.7	1370 ± 13
Ga	36 ± 0.8	39 ± 0.8	36 ± 0.8	38 ± 0.8	36 ± 0.8

Table C1 (continued)

Sample	HRV 17-D	HRV 17-D	HRV 17-D	HRV 17-D
Mineral	Gar	Gar	Gar	Gar
An. #	26	27	29	30
Cr	650 ± 175	961 ± 245	575 ± 141	< 322
Mn	2390 ± 70	2620 ± 73	1520 ± 81	1620 ± 61
Fe	11 ± .03%	11 ± .04%	8.7 ± .04%	8.7 ± .03%
Zn	80 ± 2.7	86 ± 4.4	72 ± 2.3	69 ± 2.3
Ga	10 ± 1.8	9.6 ± 1.4	9.8 ± 1.3	8.3 ± 1.4
Sr	42 ± 2.3	5.8 ± 1.7	6.9 ± 1.4	14 ± 1.6
Y	21 ± 1.8	26 ± 2.2	22 ± 1.8	17 ± 1.6
Zr	42 ± 2.9	40 ± 2.4	37 ± 3.7	37 ± 2.4

Table C2

Sample HRV 30

Sample	HRV 30-1	HRV 30-1	HRV 30-1	HRV 30-1	HRV 30-1
Mineral	Gar	Gar	Gar	Gar	Gar
An. #	1	2	3	4	5
Cr	814 ± 219	1130 ± 271	< 493	638 ± 207	< 499
Mn	2630 ± 124	2690 ± 123	2710 ± 121	2790 ± 205	2480 ± 120
Fe	10.9*	10.9*	10.9*	10.9*	10.9*
Zn	61 ± 4.5	59 ± 6.0	58 ± 4.0	66 ± 4.3	55 ± 4.0
Ga	11 ± 2.3	11 ± 2.3	9.3 ± 2.7	< 9.1	9.1 ± 2.3
Sr	< 7.6	8.1 ± 2.6	< 6.1	25 ± 5.6	20 ± 4.4
Y	16 ± 3.0	16 ± 3.0	27 ± 5.3	20 ± 3.5	14 ± 3.6
Zr	42 ± 4.7	40 ± 4.7	39 ± 4.3	35 ± 5.8	30 ± 7.4

Sample	HRV 30-1	HRV 30-1	HRV 30-1	HRV 30-1	HRV 30-1
Mineral	Gar	Gar	Gar	Gar	Gar
An. #	6	7	8	9	10
Cr	< 491	< 470	509 ± 210	< 506	< 501
Mn	2510 ± 184	2480 ± 118	2550 ± 121	2420 ± 142	2880 ± 190
Fe	10.9*	10.9*	10.9*	10.9*	10.9*
Zn	68 ± 6.2	63 ± 2.8	60 ± 5.8	64 ± 4.3	58 ± 6.5
Ga	11 ± 2.3	< 9.1	10 ± 2.4	< 9.7	< 9.7
Sr	< 6.5	12 ± 3.4	< 7.3	13 ± 3.1	18 ± 3.2
Y	15 ± 2.8	19 ± 3.0	< 7.8	12 ± 3.6	27 ± 3.5
Zr	28 ± 5.1	33 ± 4.3	29 ± 5.6	37 ± 7.0	40 ± 4.7

Table C2 (continued)

Sample	HRV 30-1	HRV 30-1	HRV 30-1	HRV 30-1
Mineral	Gar	Gar	Gar	Gar
An. #	11	12	13	14
Cr	< 485	< 489	< 479	< 496
Mn	2730 ± 152	2690 ± 142	2600 ± 119	2700 ± 166
Fe	10.9*	10.9*	10.9*	10.9*
Zn	55 ± 4.1	49 ± 3.9	59 ± 5.0	60 ± 4.1
Ga	9.7 ± 2.4	11 ± 2.3	< 9.1	9.2 ± 2.3
Sr	< 6.7	11 ± 3.2	7.4 ± 2.4	9.4 ± 2.6
Y	15 ± 2.8	13 ± 2.7	22 ± 4.3	17 ± 4.4
Zr	24 ± 3.7	45 ± 4.8	22 ± 4.4	34 ± 6.0

Sample	HRV 30-1	HRV 30-1	HRV 30-1	HRV 30-1	HRV 30-1
Mineral	Cpx	Cpx	Cpx	Cpx	Cpx
An. #	1	2	3	4	5
Mn	432 ± 21	414 ± 15	354 ± 21	375 16	443 ± 16
Fe	2.45*	2.45*	2.45*	2.45*	2.45*
Zn	143 ± 5.8	30 ± 3.4	26 ± 3.8	34 3.4	28 ± 2.6
Ga	10 ± 2.5	< 8.2	8.8 ± 2.0	< 8.3	11 ± 2.5
Sr	116 ± 12	107 ± 11	99 ± 10	123 12	209 ± 14
Zr	54 ± 11	32 ± 8.8	53 ± 15	39 11	35 ± 11
Ba	< 1240	< 1100	< 1180	< 1360	< 437

Table C2 (continued)

Sample	HRV 30-1	HRV 30-1	HRV 30-1	HRV 30-1	HRV 30-1
Mineral	Cpx	Cpx	Cpx	Cpx	Cpx
An. #	6	7	8	9	10
Mn	441 ± 19	577 ± 18	474 ± 16	382 ± 14	421 ± 17
Fe	2.45*	2.45*	2.45*	2.45*	2.45*
Zn	32 ± 3.0	26 ± 4.3	26 ± 3.6	41 ± 3.1	31 ± 4.7
Ga	16 ± 2.5	< 7.4	< 7.8	12 ± 2.3	17 ± 2.4
Sr	205 ± 13	156 ± 10	125 ± 12	182 ± 15	147 ± 12
Zr	43 ± 10	30 ± 7.8	26 ± 7.9	40 ± 11	20 ± 14

Sample	HRV 30-2	HRV 30-2	HRV 30-2	HRV 30-2	HRV 30-2
Mineral	Gar	Gar	Gar	Gar	Gar
An. #	1	2	3	4	5
Cr	< 288	650 ± 122	439 ± 117	390 ± 119	454 ± 121
Mn	1460 ± 61	1520 ± 77	1550 ± 65	1540 ± 67	1580 ± 62
Fe	8.6 ± .03%	8.6 ± .03%	8.5 ± .02%	8.7 ± .02%	8.7 ± .03%
Zn	58 ± 2.0	59 ± 2.7	57 ± 1.9	59 ± 2.4	61 ± 1.9
Ga	9.8 ± 1.2	8.5 ± 1.4	9.5 ± 1.1	9.1 ± 1.1	11 ± 1.4
Sr	< 3.2	6.6 ± 1.4	< 3.1	< 3.1	13 ± 1.3
Y	12 ± 1.3	13 ± 1.5	13 ± 1.2	11 ± 1.3	14 ± 1.3
Zr	36 ± 2.1	37 ± 2.0	37 ± 2.0	34 ± 2.3	37 ± 3.1

Table C2 (continued)

Sample	HRV 30-2	HRV 30-2	HRV 30-2	HRV 30-2	HRV 30-2
Mineral	Gar	Gar	Gar	Gar	Gar
An. #	6	7	8	9	10
Cr	295 ± 121	657 ± 125	643 ± 128	473 ± 187	645 ± 127
Mn	1570 ± 70	1760 ± 75	1750 ± 65	1590 ± 63	1910 ± 68
Fe	9.1 ± .02%	9.2 ± .03%	9.3 ± .03%	8.8 ± .03%	9.5 ± .03%
Zn	60 ± 1.9	55 ± 1.8	59 ± 1.9	58 ± 1.9	59 ± 2.1
Ga	8.3 ± 1.2	8.7 ± 1.2	10 ± 1.1	9.3 ± 1.2	8.3 ± 1.4
Sr	3.4 ± 1.4	8.5 ± 1.4	4.2 ± 1.2	15 ± 1.5	4.9 ± 1.1
Y	14 ± 2.1	17 ± 1.5	13 ± 1.3	13 ± 1.3	16 ± 1.3
Zr	45 ± 2.2	41 ± 2.1	29 ± 1.9	47 ± 2.8	41 ± 2.1

Sample	HRV 30-2	HRV 30-2	HRV 30-2	HRV 30-2	HRV 30-2
Mineral	Gar	Gar	Gar	Gar	Gar
An. #	11	12	13	14	15
Cr	448 ± 129	484 ± 127	209 ± 124	547 ± 155	555 ± 122
Mn	1930 ± 68	2150 ± 63	2440 ± 66	2390 ± 93	2480 ± 67
Fe	9.1 ± .03%	9.3 ± .03%	9.8 ± .03%	9.9 ± .04%	9.9 ± .04%
Zn	58 ± 1.8	53 ± 1.8	57 ± 1.9	57 ± 1.9	54 ± 2.4
Ga	8.4 ± 1.3	6.7 ± 1.0	8.3 ± 1.3	< 3.9	6.8 ± 1.0
Sr	< 3.1	4.8 ± 1.5	5.1 ± 1.1	< 2.9	< 3.1
Y	15 ± 1.4	20 ± 2.0	19 ± 2.2	16 ± 1.3	16 ± 1.4
Zr	27 ± 1.8	30 ± 2.4	27 ± 1.8	25 ± 1.8	31 ± 2.2

Table C2 (continued)

Sample	HRV 30-3	HRV 30-3	HRV 30-3	HRV 30-3	HRV 30-3
Mineral	Gar	Gar	Gar	Gar	Gar
An. #	1	2	3	4	5
Cr	473 ± 177	< 392	600 ± 202	528 ± 169	598 ± 176
Mn	1420 ± 78	1340 ± 76	1370 ± 159	1440 ± 132	1490 ± 79
Fe	8.59%*	8.59%*	8.59%*	8.59%*	8.59%*
Zn	61 ± 3.0	59 ± 3.4	63 ± 3.3	58 ± 3.0	68 ± 3.1
Ga	15 ± 1.9	7.7 ± 1.7	14 ± 1.9	12 ± 1.8	14 ± 1.8
Sr	9.8 ± 1.9	9.2 ± 1.8	7.9 ± 1.9	10 ± 1.9	< 5.1
Y	14 ± 1.9	11 ± 2.1	9.7 ± 1.9	12 ± 2.1	11 ± 2.8
Zr	51 ± 3.5	39 ± 3.2	45 ± 3.4	54 ± 3.6	42 ± 3.2

Sample	HRV 30-3	HRV 30-3	HRV 30-3	HRV 30-3	HRV 30-3
Mineral	Gar	Gar	Gar	Gar	Gar
An. #	6	7	8	9	10
Cr	1000 ± 169	< 396	629 ± 207	960 ± 169	< 394
Mn	1380 ± 78	1370 ± 77	1400 ± 78	1330 ± 86	1460 ± 123
Fe	8.59%*	8.59%*	8.59%*	8.59%*	8.59%*
Zn	65 ± 3.1	70 ± 3.2	61 ± 3.0	72 ± 3.2	60 ± 4.4
Ga	13 ± 1.8	14 ± 1.8	13 ± 1.8	14 ± 2.1	11 ± 2.0
Sr	5.7 ± 1.7	5.7 ± 2.2	< 4.8	7.3 ± 1.8	18 ± 2.2
Y	12 ± 2.2	12 ± 1.9	13 ± 1.9	11 ± 2.0	16 ± 1.0
Zr	41 ± 3.8	44 ± 3.3	45 ± 3.4	50 ± 4.4	41 ± 4.9

Table C2 (continued)

Sample	HRV 30-3	HRV 30-3	HRV 30-3	HRV 30-3	HRV 30-3
Mineral	Gar	Gar	Gar	ACpx	ACpx
An. #	28	29	30	1	2
Cr	802 ± 188	887 ± 224	760 ± 209	NA	NA
Mn	1490 ± 86	1450 ± 85	1450 ± 175	124 ± 52	267 ± 52
Fe	8.59%*	8.59%*	8.59%*	1.75%*	1.75%*
Zn	65 ± 3.5	66 ± 3.1	63 ± 4.2	39 ± 2.8	44 ± 5.1
Ga	9.3 ± 2.5	15 ± 1.9	13 ± 1.9	27 ± 2.9	25 ± 2.3
Sr	7.7 ± 2.4	5.7 ± 1.8	16 ± 3.0	289 ± 7.8	233 ± 7.9
Y	18 ± 3.3	15 ± 2.6	12 ± 2.5	< 7.6	< 6.7
Zr	53 ± 3.6	53 ± 5.0	40 ± 3.3	28 ± 6.3	29 ± 4.7
Ba	NA	NA	NA	534 ± 101	2790 ± 190

Sample	HRV 30-3	HRV 30-3	HRV 30-3	HRV 30-3	HRV 30-3
Mineral	ACpx	ACpx	ACpx	ACpx	ACpx
An. #	3	4	5	7	8
Mn	263 ± 49	145 ± 39	164 ± 40	311 ± 41	166 ± 42
Fe	1.75%*	1.75%*	1.75%*	1.75%*	1.75%*
Zn	39 ± 2.8	41 ± 2.8	40 ± 2.8	49 ± 2.8	43 ± 4.3
Ga	28 ± 2.8	32 ± 2.4	27 ± 2.7	25 ± 2.1	27 ± 4.3
Sr	223 ± 8.1	288 ± 8.1	258 ± 7.2	285 ± 9.0	27 ± 2.2
Y	< 6.8	< 6.5	< 6.8	< 6.1	< 7.8
Zr	25 ± 4.5	32 ± 10	24 ± 5.7	24 ± 4.6	33 ± 6.6
Ba	3020 ± 234	655 ± 108	548 ± 102	889 ± 123	1520 ± 149

Table C2 (continued)

Sample	HRV 30-3	HRV 30-3	HRV 30-3	HRV 30-3	HRV 30-3
Mineral	ACpx	ACpx	ACpx	ACpx	ACpx
An. #	9	10	11	12	16
Mn	247 ± 73	167 ± 37	230 ± 53	138 ± 47	183 ± 39
Fe	1.75%*	1.75%*	1.75%*	1.75%*	1.75%*
Zn	35 ± 3.2	46 ± 2.8	45 ± 3.1	50 ± 4.2	38 ± 2.7
Ga	28 ± 2.3	27 ± 2.2	30 ± 2.8	31 ± 2.5	27 ± 2.2
Sr	306 ± 7.9	241 ± 9.1	316 ± 7.9	262 ± 7.2	304 ± 12
Y	< 7.0	6.3 ± 2.1	< 7.3	< 7.6	< 6.8
Zr	33 ± 5.5	25 ± 5.3	29 ± 6.5	20 ± 4.8	22 ± 4.7
Ba	1220 ± 186	1220 ± 194	2050 ± 164	2820 ± 205	695 ± 131

Sample	HRV 30-3	HRV 30-3	HRV 30-3	HRV 30-3	HRV 30-3
Mineral	Ky	Ky	Ky	Ky	Ky
An. #	16	19	21	25	26
Ca	210 ± 37	274 ± 88	173 ± 45	308 ± 68	136 ± 50
Ti	594 ± 11	626 ± 16	605 ± 12	594 ± 11	586 ± 12
V	70 ± 5	61 ± 7.1	76 ± 5.1	82 ± 6.5	69 ± 5.1
Cr	581 ± 5.9	609 ± 12	575 ± 5.1	581 ± 5.1	565 ± 5.0
Fe	1480 ± 6.0	1370 ± 9.0	1140 ± 5.7	1140 ± 5.4	1150 ± 5.0
Ga	33 ± 1.4	35 ± 1.6	33 ± 1.3	32 ± 1.4	31 ± 1.0

Table C2 (continued)

Sample	HRV 30-3	HRV 30-3	HRV 30-3	HRV 30-3	HRV 30-3
Mineral	Ky	Ky	Ky	Ky	Ky
An. #	27	34	35	36	37
Ca	234 ± 51	195 ± 38	< 111	139 ± 35	< 108
Ti	572 ± 12	569 ± 14	567 ± 14	575 ± 12	584 ± 11
V	61 ± 5.0	64 ± 9.5	68 ± 5.1	73 ± 5.0	70 ± 5.2
Cr	561 ± 5.0	581 ± 5.1	594 ± 5.1	590 ± 8.8	594 ± 5.2
Fe	1270 ± 6.2	1500 ± 9.5	1500 ± 1.9	1150 ± 5.0	1120 ± 6.3
Ga	31 ± 1.1	34 ± 1.0	32 ± 1.0	32 ± 1.1	33 ± 1.3

Sample	HRV 30-3	HRV 30-3	HRV 30-4	HRV 30-4	HRV 30-4
Mineral	Ky	Ky	Gar	Gar	Gar
An. #	39	40	1	2	3
Ca	< 103	203 ± 37	NA	NA	NA
Ti	567 ± 20	541 ± 11	NA	NA	NA
V	76 ± 7.3	74 ± 5.0	NA	NA	NA
Cr	559 ± 9.1	561 ± 5.0	< 260	526 ± 139	281 ± 111
Mn	NA	NA	1620 ± 74	1700 ± 94	1560 ± 60
Fe	1030 ± 6.3	1140 ± 6.5	9.1 ± .02%	9.2 ± .03%	9.1 ± .03%
Zn	NA	NA	68 ± 2.0	64 ± 1.9	65 ± 2.0
Ga	32 ± 1.2	33 ± 1.2	7.6 ± 1.4	7.6 ± 1.2	7.4 ± 1.1
Sr	NA	NA	3.6 ± 1	< 3.1	< 3.4
Y	NA	NA	19 ± 1.4	20 ± 1.6	19 ± 1.5
Zr	NA	NA	48 ± 3.1	54 ± 2.3	51 ± 2.3

Table C2 (continued)

Sample	HRV 30-4	HRV 30-4	HRV 30-4	HRV 30-4	HRV 30-4
Mineral	Gar	Gar	Gar	Gar	Gar
An. #	4	5	6	7	8
Cr	< 263	< 264	< 261	280 ± 116	< 274
Mn	1480 ± 100	1650 ± 61	1260 ± 126	1610 ± 102	2000 ± 62
Fe	9.1 ± .05%	9.1 ± .04%	9.1 ± .07%	9.3 ± .05%	9.8 ± .04%
Zn	62 ± 1.9	64 ± 1.9	65 ± 2.9	63 ± 1.9	64 ± 2.7
Ga	6.3 ± 1.4	8.2 ± 1.3	7.6 ± 1.1	6.7 ± 1.5	6.5 ± 1.6
Sr	< 3.4	< 3.6	< 3.6	< 3.5	< 2.9
Y	19 ± 1.7	19 ± 1.6	18 ± 1.4	21 ± 2.0	21 ± 1.4
Zr	55 ± 2.9	51 ± 2.2	50 ± 2.3	49 ± 2.4	43 ± 2.1

Sample	HRV 30-4	HRV 30-4	HRV 30-4	HRV 30-4	HRV 30-4
Mineral	Gar	Gar	Gar	Gar	Gar
An. #	9	10	11	12	13
Cr	< 268	< 271	< 278	< 284	341 ± 140
Mn	1700 ± 85	1730 ± 94	2160 ± 106	2120 ± 116	2300 ± 90
Fe	9.4 ± .05%	9.6 ± .07%	10 ± .04%	10 ± .08%	10 ± .06%
Zn	60 ± 1.9	58 ± 1.9	60 ± 1.9	52 ± 2.0	59 ± 1.9
Ga	7.0 ± 1.1	5.3 ± 1.3	7.1 ± 1.0	7.4 ± 1.1	6.1 ± 1.1
Sr	< 3.4	< 3.4	< 3.5	< 3.5	< 3.8
Y	23 ± 2.2	20 ± 1.4	19 ± 1.4	14 ± 1.3	13 ± 1.3
Zr	43 ± 2.4	33 ± 1.9	32 ± 1.8	24 ± 1.9	24 ± 1.7

Table C2 (continued)

Sample	HRV 30-4	HRV 30-4	HRV 30-4	HRV 30-4	HRV 30-4
Mineral	Gar	Gar	Ky	Ky	Ky
An. #	14	15	1	2	3
Ca	NA	NA	286 ± 58	169 ± 71	161 ± 49
Ti	NA	NA	665 ± 20	657 ± 11	659 ± 19
V	NA	NA	95 ± 4.8	90 ± 6.0	94 ± 4.8
Cr	557 ± 145	309 ± 117	491 ± 4.0	503 ± 6.0	471 ± 3.9
Mn	2350 ± 74	2250 ± 66	NA	NA	NA
Fe	10 ± .04%	9.9 ± .03%	1340 ± 4.4	1320 ± 5.5	1530 ± 6.2
Zn	57 ± 2.4	56 ± 1.8	NA	NA	NA
Ga	8.9 ± 1.0	5.6 ± 1.0	38 ± 1.3	39 ± 1.0	39 ± 0.9
Sr	< 3.0	< 3.0	NA	NA	NA
Y	17 ± 1.4	16 ± 1.4	NA	NA	NA
Zr	25 ± 1.7	23 ± 1.6	NA	NA	NA

Sample	HRV 30-4	HRV 30-4	HRV 30-4	HRV 30-4	HRV 30-4
Mineral	Ky	Ky	Ky	Ky	Ky
An. #	4	5	6	7	8
Ca	226 ± 33	113 ± 54	193 ± 41	178 ± 37	153 ± 45
Ti	695 ± 16	652 ± 16	689 ± 9.6	660 ± 13	656 ± 16
V	92 ± 4.4	85 ± 4.4	69 ± 5.8	78 ± 4.3	75 ± 4.3
Cr	489 ± 5.7	496 ± 4.0	490 ± 5.2	453 ± 3.8	476 ± 3.9
Fe	1540 ± 4.7	1320 ± 4.4	1430 ± 4.6	1370 ± 4.5	1270 ± 6.3
Ga	36 ± 0.9	37 ± 0.9	38 ± 0.9	39 ± 0.9	38 ± 0.9

Table C2 (continued)

Sample	HRV 30-4	HRV 30-4	HRV 30-4	HRV 30-4
Mineral	Ky	Ky	Ky	Ky
An. #	9	10	11	12
Ca	254 ± 68	2450 ± 55	254 ± 39	233 ± 40
Ti	663 ± 14	648 ± 9.9	648 ± 15	628 ± 12
V	89 ± 4.7	82 ± 4.4	93 ± 6.5	91 ± 4.4
Cr	510 ± 4.0	505 ± 4.9	435 ± 4.6	428 ± 4.8
Fe	1310 ± 5.2	1340 ± 5.5	1370 ± 7.3	1400 ± 4.5
Ga	36 ± 0.9	38 ± 0.9	36 ± 0.9	37 ± 0.9

Sample	HRV 30-7	HRV 30-7	HRV 30-7	HRV 30-7	HRV 30-7
Mineral	Gar	Gar	Gar	Gar	Gar
An. #	1	2	3	4	5
Cr	< 447	< 437	< 499	< 523	< 497
Mn	2530 ± 135	2690 ± 110	2550 ± 170	2620 ± 118	2630 ± 128
Fe	11%*	11%*	11%*	11%*	11%*
Zn	49 ± 4.7	52 ± 5.1	56 4.9	51 ± 2.9	54 ± 4.3
Ga	< 7.3	< 7.5	< 7.5	< 7.6	< 7.3
Sr	< 5.6	< 5.7	< 6.1	< 5.7	< 5.3
Y	14 ± 2.1	16 ± 4.4	16 ± 3.5	14 ± 2.3	26 ± 2.5
Zr	38 ± 3.2	28 ± 2.8	26 ± 6.7	28 ± 3.7	48 ± 3.5

Table C2 (continued)

Sample	HRV 30-7	HRV 30-7	HRV 30-7	HRV 30-7	HRV 30-7
Mineral	Gar	Gar	Gar	Gar	Gar
An. #	6	7	8	9	10
Cr	< 508	< 504	< 514	< 495	< 494
Mn	2730 ± 122	2730 ± 119	2620 ± 185	2720 ± 177	2760 ± 128
Fe	11%*	11%*	11%*	11%*	11%*
Zn	50 ± 2.9	54 ± 3.8	55 ± 4.2	57 ± 3.7	57 ± 3.0
Ga	< 7.4	< 7.2	< 7.2	< 6.9	7.5 ± 1.7
Sr	< 4.8	< 6.0	< 4.9	< 4.7	< 6.0
Y	18 ± 2.2	17 ± 2.2	16 ± 2.3	23 ± 2.6	16 ± 3.7
Zr	36 ± 4.3	35 ± 3.1	35 ± 3.1	37 ± 5.2	39 ± 3.2

Sample	HRV 30-7	HRV 30-7	HRV 30-7	HRV 30-7	HRV 30-7
Mineral	Gar	Gar	Gar	Gar	Gar
An. #	11	12	13	14	15
Cr	< 440	< 441	< 447	< 446	< 439
Mn	2520 ± 131	2720 ± 103	2520 ± 131	2510 ± 102	2480 ± 100
Fe	11%*	11%*	11%*	11%*	11%*
Zn	64 ± 3.6	51 ± 3.6	58 ± 3.6	53 ± 2.9	50 ± 5.0
Ga	6.7 ± 1.5	< 7.2	< 7.0	< 7.3	< 7.3
Sr	< 5.4	5.5	< 4.7	< 5.0	< 5.4
Y	15 ± 2.1	16 ± 2.1	20 ± 2.2	26 ± 3.0	19 ± 2.4
Zr	30 ± 3.2	31 ± 2.9	26 ± 2.7	39 ± 3.2	52 ± 3.5

Table C2 (continued)

Sample	HRV 30-7	HRV 30-7	HRV 30-7	HRV 30-7	HRV 30-7
Mineral	Cpx	Cpx	Cpx	Cpx	Cpx
An. #	11	12	13	14	15
Mn	343 ± 49	467 ± 45	691 ± 32	453 ± 45	365 ± 64
Fe	2.43%*	2.43%*	2.43%*	2.43%*	2.43%*
Zn	32 ± 2.0	32 ± 3.2	17 ± 2.2	40 ± 2.6	32 ± 2.3
Ga	10 ± 1.4	16 ± 1.7	6.9 ± 0.8	16 ± 1.6	14 ± 1.6
Sr	199 ± 5.3	489 ± 8.5	118 ± 3.7	182 ± 5.4	224 ± 6.0
Y	< 4.5	< 4.9	6.2 ± 1.2	< 5.1	< 5.1
Zr	37 ± 3.9	33 ± 4.8	35 ± 2.6	27 ± 4.2	32 ± 5.3
Ba	371 ± 66	1660 ± 128	387 ± 48	< 158	685 ± 135

Sample	HRV 30-7	HRV 30-7	HRV 30-7	HRV 30-7	HRV 30-7
Mineral	Cpx	Cpx	Cpx	Cpx	Cpx
An. #	16	17	18	19	20
Mn	392 ± 39	494 ± 49	602 ± 41	332 ± 43	413 ± 40
Fe	2.43%*	2.43%*	2.43%*	2.43%*	2.43%*
Zn	36 ± 2.4	38 ± 2.3	29 ± 1.8	37 ± 2.7	43 ± 2.8
Ga	16 ± 1.7	18 ± 2.1	11 ± 1.6	16 ± 1.7	17 ± 1.7
Sr	178 ± 7.1	199 ± 6.8	178 ± 4.7	177 ± 6.2	178 ± 6.8
Y	< 5.3	< 5.1	< 4.0	< 4.7	< 5.1
Zr	20 ± 4.1	21 ± 4.6	38 ± 3.5	26 ± 3.7	25 ± 3.8
Ba	< 165	< 168	628 ± 78	< 172	< 161

Table C2 (continued)

Sample	HRV 30-7	HRV 30-7	HRV 30-7	HRV 30-7	HRV 30-7
Mineral	Cpx	Cpx	Cpx	Cpx	Cpx
An. #	25	26	27	28	29
Mn	468 ± 35	441 ± 38	381 ± 37	472 ± 42	493 ± 46
Fe	2.43%*	2.43%*	2.43%*	2.43%*	2.43%*
Zn	26 ± 2.0	38 ± 2.0	35 ± 1.9	38 ± 2.0	35 ± 2.7
Ga	10 ± 1.3	15 ± 1.7	18 ± 1.8	13 ± 2.8	13 ± 1.5
Sr	179 ± 4.8	182 ± 4.5	180 ± 5.6	185 ± 4.6	182 ± 4.4
Y	< 3.9	< 4.5	< 4.3	< 4.5	< 3.9
Zr	22 ± 2.8	22 ± 4.0	22 ± 3.1	30 ± 3.3	24 ± 3.0
Ba	690 ± 69	< 150	< 162	244 ± 54	< 133

Sample	HRV 30-7	HRV 30-7	HRV 30-7	HRV 30-7
Mineral	Cpx	Cpx	Cpx	Cpx
An. #	30	31	32	33
Mn	384 ± 60	384 ± 34	461 ± 35	471 ± 36
Fe	2.43%*	2.43%*	2.43%*	2.43%*
Zn	38 ± 2.7	32 ± 2.6	39 ± 1.9	36 ± 1.9
Ga	17 ± 1.9	11 ± 2.1	14 ± 1.9	16 ± 1.4
Sr	192 ± 5.1	205 ± 4.5	191 ± 4.5	187 ± 4.5
Y	< 3.9	< 4.1	< 4.5	< 4.1
Zr	25 ± 3.1	26 ± 4.5	21 ± 3.1	24 ± 3.2
Ba	< 135	370 ± 57	184 ± 50	233 ± 52

Table C3

Sample JJG-4

Sample	JJG 4	JJG 4	JJG 4	JJG 4	JJG 4
Mineral	Gar	Gar	Gar	Gar	Gar
An. #	1	2	5	6	7
Cr	972 ± 195	1000 ± 200	1190 ± 263	1530 ± 220	1410 ± 218
Mn	2210 ± 108	2240 ± 112	2500 ± 171	2630 ± 152	2520 ± 198
Fe	9.64%*	9.64%*	9.64%*	9.64%*	9.64%*
Zn	86 ± 3.4	90 ± 2.8	88 ± 3.7	88 ± 5.6	88 ± 2.8
Ga	8.3 ± 1.8	< 5.7	8.7 ± 1.3	< 5.9	6.3 ± 1.4
Sr	< 4.6	5.4 ± 1.8	< 4.5	5.8 ± 2.0	< 4.5
Y	17 ± 1.8	17 ± 2.7	13 ± 2.8	17 ± 1.8	20 ± 2.0
Zr	27 ± 2.8	34 ± 3.0	26 ± 2.1	29 ± 3.4	27 ± 3.6

Sample	JJG 4	JJG 4	JJG 4	JJG 4	JJG 4
Mineral	Gar	Gar	Gar	Gar	Gar
An. #	8	9	10	11	12
Cr	< 580	< 589	511 ± 154	< 385	< 379
Mn	2440 ± 62	2600 ± 178	1990 ± 74	1940 ± 87	1880 ± 111
Fe	9.64%*	9.64%*	9.64%*	9.64%*	9.64%*
Zn	98 ± 3.2	79 ± 3.0	93 ± 2.7	91 ± 3.0	90 ± 3.2
Ga	6.3 ± 2.6	6.6 ± 1.5	< 5.5	6.7 ± 1.3	6.6 ± 1.3
Sr	< 4.6	< 4.4	< 4.2	< 4.3	5.4 ± 1.5
Y	14 ± 2.2	12 ± 2.4	16 ± 1.8	17 ± 2.1	16 ± 2.0
Zr	32 ± 3.1	27 ± 3.9	30 ± 2.3	32 ± 2.4	31 ± 3.4

Table C3 (continued)

Sample	JJG 4	JJG 4	JJG 4	JJG 4	JJG 4
Mineral	Gar	Gar	Gar	Gar	Gar
An. #	13	14	23	24	25
Cr	859 ± 175	< 374	< 395	679 ± 156	668 ± 163
Mn	1830 ± 74	1890 ± 72	2110 ± 116	1960 ± 100	2050 ± 76
Fe	9.64%*	9.64%*	9.64%*	9.64%*	9.64%*
Zn	91 ± 3.3	87 ± 2.8	87 ± 2.7	90 ± 3.9	89 ± 3.2
Ga	8.3 ± 1.6	8.4 ± 1.6	8.6 ± 1.6	9.8 ± 1.5	8.4 ± 1.9
Sr	< 4.7	< 4.6	< 4.4	4.7 ± 1.9	< 4.4
Y	9.9 ± 1.8	11 ± 1.6	11 ± 2.7	7.4 ± 1.4	11 ± 1.5
Zr	28 ± 2.4	27 ± 2.6	26 ± 2.2	28 ± 2.3	29 ± 2.3

Sample	JJG 4	JJG 4	JJG 4	JJG 4	JJG 4
Mineral	Cpx	Cpx	Cpx	Cpx	Cpx
An. #	15	16	17	18	19
Cr	595 ± 80	701 ± 79	520 ± 77	617 ± 110	494 ± 102
Mn	181 ± 33	211 ± 30	152 ± 35	226 ± 30	185 ± 29
Fe	1.46%*	1.46%*	1.46%*	1.46%*	1.46%*
Zn	41 ± 1.9	43 ± 2.4	38 ± 1.8	39 ± 1.8	43 ± 2.6
Ga	21 ± 1.4	20 ± 1.3	19 ± 1.3	18 ± 1.3	17 ± 1.5
Sr	103 ± 4.9	97 ± 3.1	99 ± 3.9	107 ± 3.7	106 ± 3.2
Y	< 3.8	< 3.7	< 3.9	< 4.3	< 4.0
Zr	21 ± 2.5	18 ± 2.6	20 ± 2.9	13 ± 2.4	11 ± 2.5
Ba	166 ± 58	< 136	223 ± 82	< 156	< 152

Table C3 (continued)

Sample	JJG 4	JJG 4	JJG 4	JJG 4	JJG 4
Mineral	Cpx	Cpx	Cpx	Cpx	Cpx
An. #	20	21	22	30	33
Cr	579 ± 75	581 ± 79	625 ± 80	529 ± 101	591 ± 78
Mn	197 ± 35	188 ± 46	186 ± 30	180 ± 47	200 ± 40
Fe	1.46%*	1.46%*	1.46%*	1.46%*	1.46%*
Zn	45 ± 3.1	40 ± 1.8	36 ± 1.7	42 ± 1.9	43 ± 2.4
Ga	20 ± 1.5	18 ± 1.3	19 ± 1.5	19 ± 1.3	23 ± 1.4
Sr	113 ± 4.2	99 ± 5.3	155 ± 4.3	115 ± 3.4	109 ± 3.9
Y	< 4.0	< 4.2	< 4.2	< 4.2	< 4.3
Zr	13 ± 2.3	16 ± 2.5	18 ± 3.7	9.3 ± 2.9	11 ± 2.6
Ba	< 134	185 ± 62	640 ± 75	< 159	< 151

Sample	JJG 4	JJG 4	JJG 4	JJG 4	JJG 4
Mineral	Cpx	Cpx	Cpx	Cpx	Cpx
An. #	34	35	36	38	39
Cr	629 ± 90	687 ± 75	682 ± 98	724 ± 81	705 ± 80
Mn	220 ± 30	142 ± 28	188 ± 29	199 ± 31	245 ± 33
Fe	1.46%*	1.46%*	1.46%*	1.46%*	1.46%*
Zn	40 ± 1.8	37 ± 3.4	38 ± 1.8	40 ± 1.9	42 ± 1.8
Ga	21 ± 2.0	15 ± 1.5	17 ± 1.5	21 ± 1.7	23 ± 1.7
Sr	114 ± 4.1	106 ± 3.3	103 ± 4.2	102 ± 3.2	118 ± 4.0
Y	< 4.1	< 3.7	< 4.1	< 4.1	< 4.0
Zr	13 ± 2.7	16 ± 2.2	14 ± 3.5	16 ± 3.3	9.8 ± 2.6
Ba	176 ± 50	< 131	< 132	174 ± 47	< 153

Table C3 (continued)

Sample	JJG 4	JJG 4	JJG 4	JJG 4	JJG 4
Mineral	ACpx	ACpx	ACpx	ACpx	ACpx
An. #	28	29	32	37	40
Cr	567 ± 79	747 ± 81	721 ± 99	359 ± 66	690 ± 80
Mn	186 ± 35	206 ± 30	184 ± 41	157 ± 26	147 ± 33
Fe	1.46%*	1.46%*	1.46%*	1.46%*	1.46%*
Zn	44 ± 1.8	39 ± 2.0	37 ± 1.9	68 ± 2.9	38 ± 1.7
Ga	20 ± 1.3	19 ± 1.3	19 ± 1.3	9.8 ± 1.1	19 ± 1.3
Sr	158 ± 3.8	152 ± 3.8	156 ± 5.4	197 ± 3.8	144 ± 3.7
Y	< 3.9	< 3.6	< 3.9	< 3.4	< 4.2
Zr	14 ± 2.5	22 ± 2.7	15 ± 3.4	23 ± 2.6	13 ± 4.6
Ba	482 ± 65	676 ± 81	419 ± 62	216 ± 59	479 ± 84

Sample	JJG 4	JJG 4	JJG 4
Mineral	Ky	Ky	Ky
An. #	3	4	27
Ca	136 ± 60	201 ± 61	176 ± 38
Ti	779 ± 14	752 ± 10	781 ± 10
V	75 ± 6.9	68 ± 4.7	83 ± 6.6
Cr	1020 ± 8.8	963 ± 5.3	1090 ± 8.8
Fe	1360 ± 9.8	1310 ± 13	1650 ± 9.4
Ga	33 ± 0.8	32 ± 0.8	31 ± 0.8

Table C4

Sample JJG 177

Sample	JJG 177-1	JJG 177-1	JJG 177-1	JJG 177-1	JJG 177-1
Mineral	Gar	Gar	Gar	Gar	Gar
An. #	1	2	3	4	7
Cr	566 ± 266	< 408	858 ± 203	784 ± 180	513 ± 216
Mn	3050 ± 86	2770 ± 103	2820 ± 81	2950 ± 92	3250 ± 112
Fe	12 ± .02%	10 ± .02%	10 ± .02%	11 ± .03%	12 ± .03%
Zn	114 ± 3.5	98 ± 3.0	100 ± 3.7	101 ± 3.1	112 ± 2.8
Ga	12 ± 1.6	14 ± 1.4	12 ± 1.4	13 ± 1.9	9.2 ± 1.4
Sr	13 ± 1.8	8.3 ± 1.6	< 4.1	7.6 ± 1.6	4.5 ± 1.6
Y	27 ± 1.9	23 ± 2.6	27 ± 3.0	29 ± 2.3	36 ± 2.0
Zr	71 ± 4.0	64 ± 4.0	69 ± 3.7	67 ± 3.5	66 ± 3.6

Sample	JJG 177-1	JJG 177-1	JJG 177-1	JJG 177-1	JJG 177-1
Mineral	Gar	Gar	Gar	Gar	Gar
An. #	8	9	10	11	12
Cr	< 420	536 ± 191	< 415	773 ± 159	938 ± 187
Mn	3030 ± 94	2850 ± 135	3020 ± 81	2530 ± 82	3020 ± 99
Fe	11 ± .02%	11 ± .03%	11 ± .02%	9.8 ± .03%	10 ± .01%
Zn	107 ± 2.7	98 ± 3.0	100 ± 3.7	90 ± 2.5	99 ± 3.5
Ga	12 ± 1.4	7.7 ± 1.3	12 ± 2.0	12 ± 1.3	15 ± 1.4
Sr	6.4 ± 1.6	9.7 ± 1.7	5.6 ± 2.0	< 4.0	5.5 ± 1.6
Y	29 ± 1.9	30 ± 1.9	28 ± 1.9	28 ± 2.5	27 ± 1.9
Zr	67 ± 2.9	71 ± 3.6	69 ± 3.1	65 ± 3.3	54 ± 2.8

Table C4 (continued)

Sample	JJG 177-1	JJG 177-1	JJG 177-1	JJG 177-1	JJG 177-1
Mineral	Gar	Gar	Gar	Gar	Gar
An. #	16	17	23	29	34
Cr	938 ± 187	746 ± 189	797 ± 222	1600 ± 212	2400 ± 336
Mn	3020 ± 99	3470 ± 150	3470 ± 134	5300 ± 150	6230 ± 168
Fe	10 ± .03%	12 ± .03%	12 ± .03%	12 ± .04%	13 ± .05%
Zn	99 ± 3.5	111 ± 2.8	101 ± 5.1	33 ± 1.9	38 ± 2.7
Ga	15 ± 1.4	15 ± 1.5	11 ± 1.5	9.0 ± 1.3	10 ± 2.0
Sr	5.5 ± 1.6	6.8 ± 1.7	9.2 ± 1.7	< 3.8	< 4.3
Y	27 ± 1.9	30 ± 2.4	32 ± 2.1	29 ± 1.9	35 ± 2.0
Zr	54 ± 2.8	66 ± 2.9	72 ± 3.0	80 ± 3.4	92 ± 5.3

Sample	JJG 177-1	JJG 177-1	JJG 177-1	JJG 177-1	JJG 177-1
Mineral	Gar	Gar	Gar	Gar	Gar
An. #	35	37	38	45	46
Cr	1620 ± 217	2690 ± 265	1380 ± 195	1470 ± 196	988 ± 351
Mn	5580 ± 129	6390 ± 129	5770 ± 143	5980 ± 135	5770 ± 224
Fe	12 ± .03%	12 ± .05%	12 ± .04%	13 ± .02%	13 ± .03%
Zn	38 ± 2.8	43 ± 2.0	39 ± 3.0	110 ± 3.2	105 ± 3.1
Ga	12 ± 1.3	16 ± 1.4	11 ± 1.3	13 ± 1.6	15 ± 1.5
Sr	< 4.0	< 4.1	< 4.2	< 4.6	6.6 ± 2.1
Y	29 ± 2.3	38 ± 2.4	28 ± 1.9	41 ± 2.7	45 ± 3.4
Zr	71 ± 3.4	88 ± 6.1	74 ± 3.1	76 ± 3.2	64 ± 4.8

Table C4 (continued)

Sample	JJG 177-1	JJG 177-1	JJG 177-1	JJG 177-1	JJG 177-1
Mineral	Ky	Ky	Ky	Ky	Ky
An. #	5	6	13	14	18
Ca	162 ± 30	186 ± 33	230 ± 30	207 ± 37	197 ± 39
Ti	544 ± 7.9	524 ± 13	544 ± 7.7	520 ± 7.6	599 ± 10
V	63 ± 5.0	62 ± 3.6	63 ± 4.2	71 ± 3.6	79 ± 4.9
Cr	306 ± 5.4	300 ± 3.9	305 ± 3.7	272 ± 3.4	275 ± 2.9
Fe	2050 ± 4.7	2010 ± 5.5	1840 ± 4.5	1810 ± 5.3	1930 ± 4.6
Ga	35 ± 0.9	35 ± 1.0	32 ± 0.7	34 ± 0.7	37 ± 1.1

Sample	JJG 177-1	JJG 177-1	JJG 177-1	JJG 177-1	JJG 177-1
Mineral	Ky	Ky	Ky	Ky	Ky
An. #	19	20	21	27	55
Ca	127 ± 50	246 ± 40	200 ± 30	103 ± 34	145 ± 35
Ti	565 ± 9.0	591 ± 10	616 ± 13	604 ± 9.3	602 ± 10
V	75 ± 4.6	78 ± 3.7	82 ± 3.8	97 ± 6.7	95 ± 3.8
Cr	269 ± 4.7	292 ± 3.6	288 ± 3.7	267 ± 2.8	257 ± 3.4
Fe	1780 ± 4.8	1770 ± 4.4	1830 ± 5.0	1860 ± 4.5	1870 ± 4.5
Ga	35 ± 0.9	34 ± 0.7	36 ± 1.0	39 ± 0.8	38 ± 0.9

Table C4 (continued)

Sample	JJG 177-2	JJG 177-2	JJG 177-2	JJG 177-2	JJG 177-2
Mineral	Gar	Gar	Gar	Gar	Gar
An. #	2	3	4	6	7
Cr	< 522	< 516	< 536	< 536	1200 ± 366
Mn	3840 ± 636	3710 ± 639	3430 ± 612	3400 ± 607	3430 ± 581
Fe	10.6%*	10.6%*	10.6%*	10.6%*	10.6%*
Zn	96 ± 7.6	96 ± 6.9	104 ± 6.8	101 ± 7.2	100 ± 7.5
Ga	9.9 ± 2.0	11 ± 2.5	8.7 ± 2.0	9.2 ± 1.8	13 ± 2.0
Sr	14 ± 2.7	10 ± 2.6	13 ± 2.4	15 ± 2.5	15 ± 2.4
Y	17 ± 2.2	17 ± 2.2	23 ± 2.5	18 ± 4.6	22 ± 2.4
Zr	53 ± 7.0	47 ± 4.1	50 ± 5.9	58 ± 4.8	52 ± 7.2

Sample	JJG 177-2	JJG 177-2	JJG 177-2	JJG 177-2	JJG 177-2
Mineral	Gar	Gar	Gar	Gar	Gar
An. #	10	14	19	20	24
Cr	905 ± 285	< 546	< 532	1080 ± 383	537
Mn	3590 ± 597	3160 ± 566	3220 ± 534	3020 ± 537	3160 ± 540
Fe	10.6%*	10.6%*	10.6%*	10.6%*	10.6%*
Zn	96 ± 6.4	102 ± 6.7	101 ± 7.4	97 ± 6.8	110 ± 7.2
Ga	9.2 ± 1.8	12 ± 2.4	11 ± 1.9	15 ± 2.0	8.9 ± 2.0
Sr	10 ± 2.8	13 ± 3.2	7.4 ± 3.3	11 ± 2.8	6.4 ± 2.1
Y	20 ± 3.6	24 ± 4.5	15 ± 2.3	25 ± 2.4	23 ± 3.1
Zr	51 ± 5.0	50 ± 3.7	41 ± 3.8	61 ± 3.9	71 ± 6.2

Table C4 (continued)

Sample	JJG 177-2	JJG 177-2	JJG 177-2	JJG 177-2
Mineral	Gar	Gar	Gar	Gar
An. #	25	26	28	29
Cr	< 525	< 535	881 ± 284	< 545
Mn	3310 ± 565	3270 ± 540	3370 ± 575	3460 ± 604
Fe	10.6%*	10.6%*	10.6%*	10.6%*
Zn	100 ± 6.6	91 ± 6.1	99 ± 7.1	98 ± 7.4
Ga	12 ± 2.3	9.4 ± 2.5	13 ± 2.2	9.1 ± 2.5
Sr	11 ± 3.5	7.2 ± 2.7	16 ± 3.8	6.5 ± 3.3
Y	17 ± 2.6	18 ± 2.2	18 ± 3.6	21 ± 2.3
Zr	56 ± 3.8	61 ± 5.4	44 ± 3.6	57 ± 4.8

Sample	JJG 177-2	JJG 177-2	JJG 177-2	JJG 177-2	JJG 177-2
Mineral	ACpx	ACpx	ACpx	ACpx	ACpx
An. #	1	3	4	5	7
Mn	193 ± 35	214 ± 35	180 ± 29	264 ± 30	183 ± 28
Fe	1.60 ±	1.79 ±	1.65 ±	1.82 ±	1.63 ±
Zn	.01%	.01%	.01%	.01%	.01%
Ga	49 ± 2.2	64 ± 2.2	52 ± 2.1	71 ± 2.6	59 ± 2.2
Sr	21 ± 1.5	25 ± 1.5	21 ± 1.4	23 ± 2.1	25 ± 1.5
Zr	152 ± 5.5	263 ± 7.5	219 ± 4.9	282 ± 6.3	204 ± 6.1
Ba	10 ± 3.0	28 ± 3.6	17 ± 3.1	16 ± 3.4	16 ± 3.1
	387 ± 67	663 ± 81	623 ± 105	665 ± 91	418 ± 75

Table C4 (continued)

Sample	JJG 177-2	JJG 177-2	JJG 177-2	JJG 177-2	JJG 177-2
Mineral	ACpx	ACpx	Cpx	ACpx	ACpx
An. #	8	9	10	11	12
Mn	231 ± 35	185 ± 32	278 ± 30	229 ± 30	280 ± 50
Fe	1.70 ±	1.64 ±	1.79 ±	1.67 ±	1.70 ±
Zn	.01%	.01%	.01%	.01%	.01%
Ga	57 ± 3.2	48 ± 2.5	60 ± 3.2	50 ± 2.1	56 ± 3.8
Sr	22 ± 1.5	26 ± 2.0	27 ± 2.0	19 ± 1.4	23 ± 1.5
Zr	210 ± 6.6	109 ± 3.6	94 ± 3.4	114 ± 3.6	118 ± 3.7
Ba	28 ± 3.4	18 ± 4.8	12 ± 3.9	13 ± 2.6	22 ± 2.9
	655 ± 99	282 ± 60	< 139	229 ± 57	198 ± 57

Sample					
Mineral	JJG 177-2	JJG 177-2	JJG 177-2	JJG 177-2	JJG 177-2
An. #	Ky	Ky	Ky	Ky	Ky
	1	5	8	9	11
Ca					
Ti	127 ± 40	121 ± 37	188 ± 62	208 ± 43	< 111
V	569 ± 11	516 ± 10	453 ± 11	501 ± 15	576 ± 22
Cr	55 ± 6.6	43 ± 5.7	52 ± 4.7	45 ± 5.5	60 ± 7.3
Fe	254 ± 3.8	263 ± 3.8	255 ± 3.8	258 ± 6.9	269 ± 6.1
Ga	1700 ± 6.1	1640 ± 5.9	1850 ± 6.3	1750 ± 9.4	1640 ± 6.3
	26 ± 1.1	26 ± 0.9	25 ± 1.2	25 ± 0.9	26 ± 1.2

Table C4 (continued)

Sample	JJG 177-2	JJG 177-2	JJG 177-2	JJG 177-2	JJG 177-2
Mineral	Ky	Ky	Ky	Ky	Ky
An. #	12	13	17	18	21
Ca	< 109	< 108	< 109	< 107	126 ± 39
Ti	538 ± 11	536 ± 13	497 ± 16	557 ± 12	508 ± 14
V	62 ± 8.2	54 ± 6.0	45 ± 7.8	54 ± 8.7	49 ± 4.8
Cr	308 ± 4.5	327 ± 4.6	341 ± 4.7	365 ± 4.3	361 ± 5.5
Fe	1610 ± 5.9	1720 ± 6.3	1660 ± 6.0	1600 ± 5.9	1580 ± 5.9
Ga	27 ± 1.0	25 ± 1.0	29 ± 1.0	26 ± 0.9	26 ± 1.0

Sample	JJG 177-2	JJG 177-2	JJG 177-2	JJG 177-2	JJG 177-2
Mineral	Ky	Ky	Ky	Ky	Ky
An. #	27	30	2	6	15
Ca	125 ± 50	< 110	138 ± 30	127 ± 38	< 87
Ti	501 ± 12	549 ± 23	544 ± 10	536 ± 13	553 ± 8.7
V	38 ± 6.8	45 ± 5.7	49 ± 4.3	63 ± 3.9	59 ± 3.9
Cr	257 ± 4.9	255 ± 3.8	337 ± 3.4	270 ± 3.5	248 ± 3.8
Fe	1760 ± 7.2	1860 ± 6.3	1580 ± 4.8	1590 ± 5.9	1680 ± 4.9
Ga	26 ± 1.0	28 ± 1.0	28 ± 0.8	26 ± 0.9	27 ± 0.8

Table C4 (continued)

Sample	JJG 177-3	JJG 177-3	JJG 177-3	JJG 177-3	JJG 177-3
Mineral	Gar	Gar	Gar	Gar	Gar
An. #	2	3	4	5	6
Mn	3750 ± 126	3970 ± 104	4010 ± 105	3550 ± 98	3000 ± 83
Fe	12 ± .04%	12 ± .02%	12 ± .04%	11 ± .02%	11 ± .03%
Zn	54 ± 4.4	54 ± 2.5	63 ± 2.6	77 ± 3.1	74 ± 2.6
Ga	< 5.5	6.9 ± 1.4	7.8 ± 2.0	8.1 ± 1.3	5.8 ± 1.3
Sr	< 4.2	< 4.3	< 3.9	5.1 ± 2.6	< 4.0
Y	16 ± 2.2	19 ± 1.9	26 ± 3.6	23 ± 2.0	25 ± 1.9
Zr	31 ± 2.3	29 ± 2.2	28 ± 2.4	50 ± 30	43 ± 3.0

Sample	JJG 177-3	JJG 177-3	JJG 177-3	JJG 177-3	JJG 177-3
Mineral	Gar	Gar	Gar	Gar	Gar
An. #	7	8	10	13	14
Mn	3920 ± 120	3710 ± 140	3360 ± 151	2590 ± 88	2570 ± 101
Fe	12 ± .03%	12 ± .03%	11 ± .04%	10 ± .03%	10 ± .03%
Zn	80 ± 3.2	84 ± 4.3	92 ± 2.7	85 ± 3.2	88 ± 2.6
Ga	8.2 ± 1.9	7.1 ± 2.2	< 5.4	10 ± 1.4	< 5.5
Sr	< 4.4	6.7 ± 2.1	11 ± 1.9	6.0 ± 1.7	6.5 ± 2.3
Y	20 ± 1.8	22 ± 1.8	13 ± 1.7	20 ± 1.7	17 ± 1.8
Zr	49 ± 2.7	52 ± 2.7	61 ± 4.5	58 ± 2.8	50 ± 4.4

Table C4 (continued)

Sample	JJG 177-3	JJG 177-3	JJG 177-3	JJG 177-3	JJG 177-3
Mineral	Ky	Ky	Ky	Ky	Ky
An. #	6	7	8	9	10
Ca	189 ± 34	212 ± 36	119 ± 57	189 ± 52	188 ± 50
Ti	677 ± 15	654 ± 10	658 ± 9.6	654 ± 9.5	641 ± 13
V	83 ± 6.3	80 ± 4.4	83 ± 4.4	89 ± 4.4	84 ± 5.2
Cr	266 ± 3.2	266 ± 5.7	292 ± 4.1	265 ± 3.5	256 ± 4.0
Fe	2140 ± 5.5	2310 ± 5.8	2280 ± 5.7	2210 ± 5.6	2450 ± 7.2
Ga	38 ± 0.9	36 ± 0.9	39 ± 1.4	38 ± 0.9	36 ± 0.9

Sample	JJG 177-4	JJG 177-4	JJG 177-4	JJG 177-4	JJG 177-4
Mineral	Gar	Gar	Gar	Gar	Gar
An. #	1	2	3	4	5
Cr	1690 ± 273	1300 ± 197	1290 ± 193	1510 ± 225	1700 ± 199
Mn	4530 ± 126	4390 ± 171	4430 ± 172	4340 ± 199	4320 ± 268
Fe	12.2%*	12.2%*	12.2%*	12.2%*	12.2%*
Zn	49 ± 3.7	45 ± 3.1	46 ± 2.8	48 ± 3.1	40 ± 4.1
Ga	7.2 ± 2.3	8.4 ± 2.0	9.6 ± 2.4	12 ± 1.7	9.1 ± 1.7
Sr	< 5.7	14 ± 2.2	6.0 ± 2.0	< 6.0	15 ± 3.0
Y	20 ± 3.2	21 ± 2.3	21 ± 2.8	21 ± 2.3	22 ± 2.3
Zr	26 ± 2.7	35 ± 3.3	34 ± 3.1	26 ± 2.7	35 ± 4.0

Table C4 (continued)

Sample	JJG 177-5	JJG 177-5	JJG 177-5	JJG 177-5	JJG 177-5
Mineral	Gar	Gar	Gar	Gar	Gar
An. #	5	6	7	8	9
Cr	1300 ± 237	1350 ± 290	1620 ± 196	878 ± 324	1020 ± 225
Mn	4460 ± 233	4580 ± 104	4480 ± 169	4520 ± 169	4570 ± 190
Fe	12.2%*	12.2%*	12.2%*	12.2%*	12.2%*
Zn	48 ± 3.3	55 ± 2.9	55 ± 2.9	52 ± 2.8	51 ± 3.1
Ga	7.8 ± 1.7	14 ± 2.1	9.1 ± 1.6	10 ± 1.7	< 6.9
Sr	6.9 ± 2.4	< 5.6	< 6.1	< 5.2	< 4.7
Y	22 ± 2.4	22 ± 2.6	18 ± 2.3	23 ± 3.5	23 ± 2.3
Zr	32 ± 3.1	27 ± 2.8	23 ± 2.7	32 ± 3.8	22 ± 3.3

Sample	JJG 177-5	JJG 177-5	JJG 177-5	JJG 177-5	JJG 177-5
Mineral	Cpx	Cpx	Cpx	Cpx	Cpx
An. #	1	2	3	4	5
Mn	1020 ± 81	945 ± 61	958 ± 70	861 ± 54	878 ± 84
Fe	3.90%*	3.90%*	3.90%*	3.90%*	3.90%*
Zn	43 ± 2.6	43 ± 4.0	40 ± 3.1	41 ± 2.6	43 ± 2.5
Ga	14 ± 1.7	13 ± 1.8	13 ± 2.7	16 ± 1.7	14 ± 1.7
Sr	282 ± 6.9	290 ± 11	289 ± 7.3	287 ± 12	292 ± 6.8
Y	< 5.1	< 5.4	< 5.3	< 5.5	5.9 ± 1.8
Zr	37 ± 5.2	38 ± 4.0	30 ± 5.4	48 ± 5.1	40 ± 6.8
Ba	< 155	< 146	< 162	< 149	< 145

Table C5

Sample PJL 17

Sample	PJL 17	PJL 17	PJL 17	PJL 17	PJL 17
Mineral	Gar	Gar	Gar	Gar	Gar
An. #	1	2	3	4	5
Cr	< 449	< 394	< 378	< 429	< 476
Mn	2210 ± 121	1680 ± 73	1620 ± 71	1880 ± 80	2040 ± 102
Fe	10.1%*	10.1%*	10.1%*	10.1%*	10.1%*
Zn	88 ± 3.0	83 ± 3.9	82 ± 3.5	80 ± 3.3	79 ± 3.7
Ga	11 ± 1.7	14 ± 1.5	10 ± 1.9	9.3 ± 1.5	8.2 ± 1.5
Sr	12 ± 2.1	15 ± 1.8	17 ± 1.9	26 ± 2.3	14 ± 2.3
Y	16 ± 1.8	19 ± 2.1	19 ± 1.9	16 ± 2.8	11 ± 1.6
Zr	58 ± 2.8	63 ± 3.1	69 ± 3.5	64 ± 3.3	58 ± 4.1

Sample	PJL 17	PJL 17	PJL 17	PJL 17	PJL 17
Mineral	Gar	Gar	Gar	Gar	Gar
An. #	6	7	8	9	10
Cr	< 462	< 460	< 453	< 412	< 432
Mn	1990 ± 83	2020 ± 89	1850 ± 127	1660 ± 130	1810 ± 102
Fe	10.1%*	10.1%*	10.1%*	10.1%*	10.1%*
Zn	86 ± 3.4	87 ± 4.7	83 ± 3.5	82 ± 3.1	84 ± 2.7
Ga	8.2 ± 1.9	12 ± 1.5	13 ± 1.7	10 ± 2.1	13 ± 1.6
Sr	13 ± 1.9	7.4 ± 1.8	9.6 ± 1.8	7.7 ± 1.7	8.0 ± 1.7
Y	16 ± 1.7	16 ± 1.8	15 ± 1.7	14 ± 1.7	14 ± 2.3
Zr	67 ± 3.2	60 ± 4.6	64 ± 3.2	64 ± 4.9	68 ± 3.2

Table C5 (continued)

Sample	PJL 17	PJL 17	PJL 17	PJL 17	PJL 17
Mineral	Ky	Ky	Ky	Ky	Ky
An. #	20	21	22	23	24
Ca	323 ± 37	133 ± 35	127 ± 37	121 ± 44	168 ± 46
Ti	668 ± 13	697 ± 9.8	677 ± 9.8	687 ± 20	667 ± 19
V	59 ± 6.5	65 ± 7.0	48 ± 4.3	38 ± 4.6	45 ± 4.3
Cr	154 ± 3.5	157 ± 3.1	154 ± 3.8	150 ± 4.2	156 ± 5.7
Fe	1790 ± 5.0	1760 ± 4.9	1750 ± 4.9	1770 ± 5.0	1800 ± 5.0
Ga	37 ± 1.0	35 ± 0.9	35 ± 0.9	35 ± 1.0	35 ± 1.3

Sample	PJL 17	PJL 17	PJL 17	PJL 17	PJL 17
Mineral	Ky	Ky	Ky	Ky	Ky
An. #	25	26	27	28	29
Ca	182 ± 52	147 ± 34	180 ± 60	234 ± 37	268 ± 38
Ti	677 ± 16	653 ± 13	645 ± 9.8	673 ± 13	675 ± 11
V	40 ± 6.7	44 ± 5.2	42 ± 4.3	45 ± 4.3	52 ± 4.3
Cr	170 ± 3.1	162 ± 5.2	177 ± 2.9	181 ± 3.9	186 ± 2.9
Fe	1750 ± 6.4	1720 ± 4.9	1760 ± 5.0	1840 ± 9.6	1830 ± 6.7
Ga	34 ± 0.9	34 ± 0.9	35 ± 0.9	37 ± 0.9	35 ± 1.0

Table C6

Roberts Victor Group I and II Eclogites

Sample	JJG 31	HRV 98	HRV 145	HRV 110	KRV 6
Mineral	Gar	Gar	Gar	Gar	Gar
An. #	21	26	42	47	52
Group	I	I	I	I	I
n	3	3	5	5	5
Cr	536 ± 92	2460 ± 65	1910 ± 153	2120 ± 168	791 ± 178
Mn	1660 ± 78	1940 ± 65	2700 ± 131	2070 ± 97	4030 ± 156
Fe	7.65%*	7.43%*	9.72%*	10.5%*	14.5%*
Zn	70 ± 2.5	34 ± 1.0	52 ± 1.9	56 ± 2.0	64 ± 1.8
Ga	7.3 ± 0.5	10 ± 0.7	13 ± 0.7	9.6 ± 0.5	14 ± 0.5
Y	3.1 ± 0.5	2.6 ± 0.6	6.3 ± 0.5	7.3 ± 0.5	78 ± 4.0
Zr	20 ± 1.8	7.6 ± 1.1	4.8 ± 0.6	15 ± 1.1	13 ± 1.2

Sample	KRV 4	HRV 247	JJG 14	HRV 173	HRV 243
Mineral	Gar	Gar	Gar	Gar	Gar
An. #	57	62	01	02	06
Group	I	I	I	II	II
n	3	5	4	4	5
Cr	1350 ± 184	669 ± 86	590 ± 77	8890 ± 155	1430 ± 143
Mn	6190 ± 189	2440 ± 73	2100 ± 49	3050 ± 140	2680 ± 114
Fe	14.7%*	8.78%*	9.25%*	6.81%*	7.85%*
Zn	52 ± 2.3	35 ± 1.1	70 ± 2.7	12 ± 0.6	23 ± 1.0
Ga	9.3 ± 0.7	15 ± 0.5	6.5 ± 0.8	9.7 ± 0.5	13 ± 0.5
Y	20 ± 1.3	13 ± 1.0	12 ± 1.2	29 ± 1.7	15 ± 1.1
Zr	13 ± 1.2	38 ± 2.9	24 ± 1.9	26 ± 2.1	22 ± 1.4

Table C6 (continued)

Sample	HRV 244	HRV 67	HRV 175	JJG 6	JJG 312
Mineral	Gar	Gar	Gar	Gar	Gar
An. #	11	16	31	36	05
Group	II	II	II	II	II
n	5	5	3	3	4
Cr	2490 ± 164	2130 ± 200	921 ± 153	1190 ± 198	3310 ± 84
Mn	2740 ± 127	3330 ± 171	4210 ± 149	3990 ± 145	3400 ± 69
Fe	8.47%*	9.95%*	15.3%*	15.3%*	5.95%*
Zn	30 ± 1.1	43 ± 1.4	68 ± 2.7	69 ± 1.8	12 ± 0.6
Ga	7.6 ± 0.419	8.2 ± 0.5	12 ± 0.7	9.9 ± 1.1	7.8 ± 0.5
Y	14 ± 0.87	11 ± 0.9	85 ± 5.6	35 ± 3.0	28 ± 1.4
Zr	3.2 ± 0.5	< 1.7	2.7 ± 0.6	< 2.5	42 ± 2.4

Sample	HRV 15	HRV 98	JJG 31	HRV 247	KRV 4
Mineral	Gar	Cpx	Cpx	Cpx	Cpx
An. #	09	26	31	41	46
Group	II	I	I	I	I
n	4	3	5	5	5
Cr	1010 ± 60	1030 ± 48	553 ± 26	335 ± 46	1120 ± 45
Mn	1490 ± 49	423 ± 29	161 ± 13	185 ± 20	1320 ± 21
Fe	6.02%*	2.53%*	1.45%*	2.03%*	5.84%*
Zn	24 ± 1.6	34 ± 0.8	45 ± 1.3	29 ± 0.7	51 ± 1.2
Ga	9.1 ± 0.5	7.0 ± 0.5	17 ± 0.5	18 ± 0.5	12 ± 0.8
Sr	NA	486 ± 6.4	208 ± 3.0	328 ± 2.6	179 ± 1.5
Y	< 1.8	< 2.1	< 1.6	< 1.6	3.6 ± 0.5
Zr	12 ± 1.6	11 ± 3.2	13 ± 1.2	31 ± 1.9	20 ± 1.3

Table C6 (continued)

Sample	HRV 110	JJG 14	HRV 67	HRV 244	HRV 243
Mineral	Cpx	Cpx	Cpx	Cpx	Cpx
An. #	56	61	01	06	11
Group	I	I	II	II	II
n	4	5	5	5	5
Cr	1490 ± 53	1440 ± 38	1270 ± 34	1080 ± 44	592 ± 30
Mn	862 ± 21	373 ± 16	250 ± 22	337 ± 25	403 ± 17
Fe	4.37%*	2.54%*	1.77%*	2.46%*	2.33%*
Zn	51 ± 0.8	51 ± 1.0	32 ± 0.8	26 ± 0.6	22 ± 1.0
Ga	13 ± 0.5	18 ± 1.0	12 ± 0.5	7.2 ± 0.5	16 ± 0.5
Sr	316 ± 2.1	1030 ± 6.0	8.7 ± 0.5	7.3 ± 0.5	350 ± 4.3
Y	3.0 ± 0.7	5.0 ± 0.5	< 1.5	< 1.5	2.2 ± 1.6
Zr	29 ± 1.3	23 ± 2.5	< 1.7	< 1.6	30 ± 1.7

Sample	HRV 173	HRV 175	JJG 6	JJG 312	HRV 15
Mineral	Cpx	Cpx	Cpx	Cpx	Cpx
An. #	16	21	36	05	09
Group	II	II	II	II	II
n	5	5	5	4	4
Cr	4890 ± 96	544 ± 74	767 ± 104	2130 ± 74	1210 ± 35
Mn	700 ± 63	428 ± 28	481 ± 40	637 ± 25	93 ± 22
Fe	2.17%*	4.66%*	4.68%*	1.65%*	0.93%*
Zn	15 ± 0.5	71 ± 1.7	60 ± 1.4	10 ± 0.6	14 ± 0.7
Ga	7.4 ± 0.4	20 ± 0.9	18 ± 0.6	9.2 ± 0.5	17 ± 0.6
Sr	178 ± 2.7	20 ± 1.2	23 ± 0.9	341 ± 4.5	110 ± 1.4
Y	4.4 ± 0.5	2.7 ± 0.4	< 1.7	5.7 ± 0.5	< 1.7
Zr	14 ± 1.2	4.2 ± 0.6	< 1.9	54 ± 1.6	2.5 ± 0.9